Thermistor-based airflow sensing on a flapping wing micro air vehicle

Faculty of Aerospace Engineering
Sunyi Wang

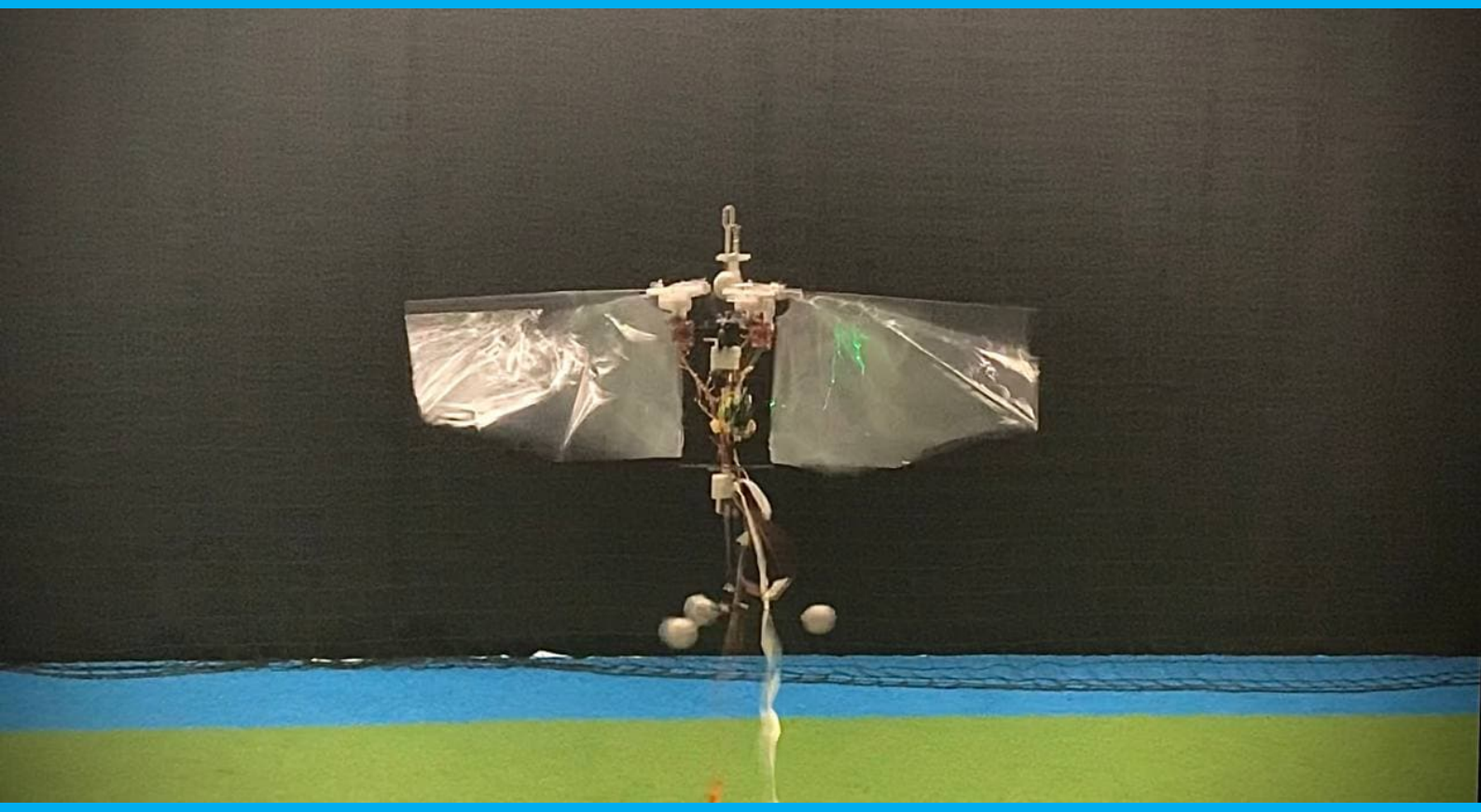

TU Delft

Thermistor-based airflow sensing on a flapping wing micro air vehicle

by

to obtain the degree of Master of Science
at the Delft University of Technology,
to be defended publicly on Tuesday September 28th, 2021 at 11:00 AM.

Student number:	4832019	
Project duration:	October 26th, 2020 – September 28th, 2021	
Thesis committee:	Dr. ir. B. W. (Bas) van Oudheusden,	TU Delft, supervisor and chair
	Prof. dr. G. C. H. E. (Guido) de Croon,	TU Delft, supervisor and examiner
	D. A. (Diana) Olejnik, MSc	TU Delft, daily supervisor
	Ir. C. (Christophe) de Wagter,	TU Delft, examiner

TU Delft

Preface

My interest in flapping wings and animal flight started back then in 2016 during my undergraduate research time when I first got exposed to some relevant projects from Jun, Leif and Stephen. I was always fascinated by birds' flight performance since a kid but not until then did I realize there is a whole big world of it out there. That brought me to TU Delft, to Delfly. Through further learning during the first year, I soon realized how multi-disciplinary the world of flapping wings is. The more I learn, the more I realise I do not know.

As an experiment-heavy thesis project, the experimental parts were carried out entirely during the COVID-19 pandemic, including the heaviest amount of work in the wind tunnels which was done during the strictest lockdown period throughout the first half of 2021. It was fortunate to be able to even use the university facility under strict measures given the devastating situation globally. Otherwise all this work would not have been possible. I still remember the very first day of my wind tunnel testing weeks. It had snowed so heavily the night before, so I had to walk to the faculty with three big bags of equipment needed for testing. It felt a bit strange with the empty campus, especially when you approach the nuclear reactor near the Aerospace faculty under the ominous snow weather. Overall, without the meaningful daily social contact, it was more difficult to make progress, criticize results, discuss questions and learn from peers.

This thesis would not be possible without the help from numerous people. Thank you Diana for giving me the student assistant position that allowed me to learn about all aspects of Delfly Nimble before I started the thesis. The knowledge exchange and the experiment collaboration we had is like no other. Your encouragement and hands-on practice spirit made me have more confidence in myself to learn and do things I have never done before.

Thank you to Bas and Guido for giving me full freedom to design and carry out tests independently and provide critical feedback during the process. This full autonomy is difficult at first when I had no clue where to start from but it pushed me to learn faster and learn to look for help effectively.

Thank you to Edo and Marios for handling the unexpected broken hot-wire bridge situation and connecting me with the start-up company Dimple Technology where Olaf and Michiel lent me their equipment under a short notice and rescued my tests by avoiding months of delay.

Thanks to all the lab technicians Dennis, Peter, Frits, Henk-Jan, Nico, Erik and the MAVLab squad. Without your help, I would not be able to assemble the test set-ups that I needed and arrange all the logistics. Thank you Stefan for coming to the low-speed lab again and again setting up the data acquisition with me and debugging numerous small problems.

Thank you to my family and friends scattered around the world for your remote support during this process. I have been on the move for the past 10 years across different cities and different continents. It would not have been possible without you guys. Thank you Nilay, Alina, Likhit and Ran for the once-in-a-while crazy laughter and listening to my rambling.

Last but not least, thank you Philip. I could not survive in Delft without the joy and peace from you. You remind me everyday to never stop thinking or questioning about things, to cherish life and to be proud of myself. Thank you Lin, Ton and Jelle for your never stopping support and love, en het lekkerste eten van heel Nederland.

Cheers to the future.

Delft, September 2021

Contents

Abstract

Flow sensing exists widely in nature to help animals perform certain tasks. It has also been widely adopted in engineering applications with different types of sensing instrumentation. In particular, in the field of aerospace engineering, airflow sensing is crucial to vehicle state evaluation and flight control. This project surveys the key mechanisms from biological features in nature that enable flow sensing and expands towards the application motivation to identify a suitable airflow sensor that can be equipped to a flapping wing micro air vehicle (FWMAV) for onboard airflow sensing.

The selection of sensors is first narrowed down to three major types of airflow sensors from the state of art that have the most potential to be integrated onboard a flapping wing MAV, considering the sensor performance need, size, weight and power (SWaP) restrictions. Two thermal-based commercially available low-cost airflow sensors RevP and RevC from Modern Device have been selected after the trade-off analysis.

A full workflow of calibrating and evaluating the two airflow sensors' directional sensitivity has been carried out through two wind tunnel campaigns. Their performance under grid-generated turbulence is compared with a constant temperature hot-wire anemometer. This series of tests leads to the conclusion that the RevP airflow sensor has better performance and is therefore chosen to be placed onboard a flapping wing MAV Delfly Nimble.

Both mounted tests and tethered hovering tests with the Delfly Nimble are performed to further examine the airflow sensor RevP's measurement performance under different influence factors such as MAV throttle levels, MAV body pitch angles and freestream speeds. In the end, it is concluded that as a proof of concept, the RevP sensor is capable of performing effective measurements for low flow speeds less than 4 m/s, within the pitching angle range of ± 30 degrees. Although this is the first achieved tethered hover flight with onboard airflow sensing for a flapping wing MAV, its limited payload and onboard power supply demands an even smaller and less power consuming design of airflow sensors to enable further applications such as autonomous reactive control under wind disturbances.

Nomenclature

Latin letters

A	[-]	Wheatstone bridge bridge ratio
c	[J·kg^{-1}·K^{-1}]	Hot-wire sensor material specific heat
C_P	[-]	Pressure coefficient
d	[m]	Hot-wire sensor sensing wire diameter
E_w	[V]	Anemometer output voltage
f	[-]	Sensitivity factor
g	[m/s^2]	Amplitude in power spectral density analysis
h	[W/(m^{2}K)]	Coefficient of convective heat transfer
I	[A]	Heating current through the hot-wire sensor
k_s	[W·m^{-1}·K^{-1}]	Coefficient of thermal conductivity for the hot-wire sensor material
P_α	[pa]	5-hole probe pressure differential between top and bottom hole
P_β	[pa]	5-hole probe pressure differential between right and left hole
P_R	[pa]	5-hole probe pressure differential between center and top hole
P_∞	[pa]	Freestream pressure
q	[pa]	Dynamic pressure
t	[s]	Time
T_a	[K]	Ambient fluid temperature
T_f	[K]	Temperature of the fluid
T_s	[K]	Temperature of the hot-wire sensor
T_{sur}	[K]	Temperature of the surrounding
T_w	[K]	Hot-wire temperature
U	[m/s]	Air velocity
U_∞	[m/s]	Freestream velocity
x	[m]	Distance measured along the hot-wire sensor

Greek letters

α	[rad]	Angle of attack
β	[rad]	Side slip angle
ϵ	[-]	Emissivity of the hot-wire sensor
ϕ	[rad]	Roll angle
θ	[rad]	Pitch angle
ρ	[kg/m^3]	Flow density; density of the hot-wire sensor material
ρ_r	[Ω·m]	Resistivity of hot-wire sensor material
σ	[W·m^{-2}·K^{-4}]	Stefan-Boltzmann constant
ψ	[rad]	Yaw angle

Acronyms

AOA	Angle of attack
COTS	Commercially available off-the-shelf
CCA	Constant current anemometer
CTA	Constant temperature anemometer
DAQ	Data acquisition
DOF	Degree of freedom
IMU	Inertial measurement unit
FWMAV	Flapping wing micro air vehicle
HWA	Hot wire anemometry
MAV	Micro air vehicle
MEMS	Microelectromechanical systems
PCB	Printed circuit board
PIV	Particle image velocimetry
PLA	Polylactic acid
PTC	Positive temperature coefficient
RPM	Revolution per minute

List of Figures

List of Tables

1 Introduction

Airflow sensing exists widely among flyers in nature and is a necessary measurement input in aerospace applications. This is not the case yet for flapping wing micro air vehicles (FWMAV). As one of the younger members in the air vehicle family, improving FWMAV's flight stability in presence of wind disturbances is an ongoing challenge without a mature solution of miniaturized airflow sensing instrumentation. This chapter introduces the research motivation for airflow sensing on flapping wing MAVs and the challenge that lies in the flow measurement. The research question and sub-questions are formed with the research objective. Finally an outline of the full thesis research project is presented.

1.1. Research motivation

1.1.1. Airflow sensing in nature and aviation

Atmospheric winds present a considerable challenge to insects, birds and flying vehicles of all sizes. Despite having extremely sophisticated and interactive flow sensing and control capabilities, as airflow speed increases, eventually even the most capable flyer in nature or artificial air vehicle will have to remain grounded. A summary of flying speeds that indicate the wind conditions where different animals and aircrafts can fly in is reproduced by Watkins et al. [95] from Tennekes [88], as shown in Figure 1.1.

In both aircraft operations and unmanned aerial vehicle operations, a reliable measurement of the airflow speed and direction plays an important role in flight stability control, takeoff, landing and vehicle heading. In the case of smaller sized unmanned micro air vehicles (MAV) (0.5-4 m wingspan, 0.5-10 kg takeoff weight [56]), as the airspeed of the vehicle is in the same magnitude of the wind velocity, the vehicle's flight path and stability is more susceptible to the ambient airflow changes.

In MAV applications, to measure the true airspeed, any added-on sensing component has to be balanced with the vehicle's mass and power budget, along with the sensor data's processing power need. The typical wind anemometry techniques used in larger aircrafts or weather forecasting cannot be directly applied onboard of an MAV due to its size and power restriction. This motivates the ongoing research into small-sized airflow sensing instrumentation that are more suitable for MAVs, which is particularly challenging for flapping wing MAVs given the more strict power and payload restriction.

1.1.2. Challenge in flow measurement

Flow measurement techniques have been extensively explored and applied in various academic research branches and industrial applications for over two centuries, through the use of *in situ* sens-

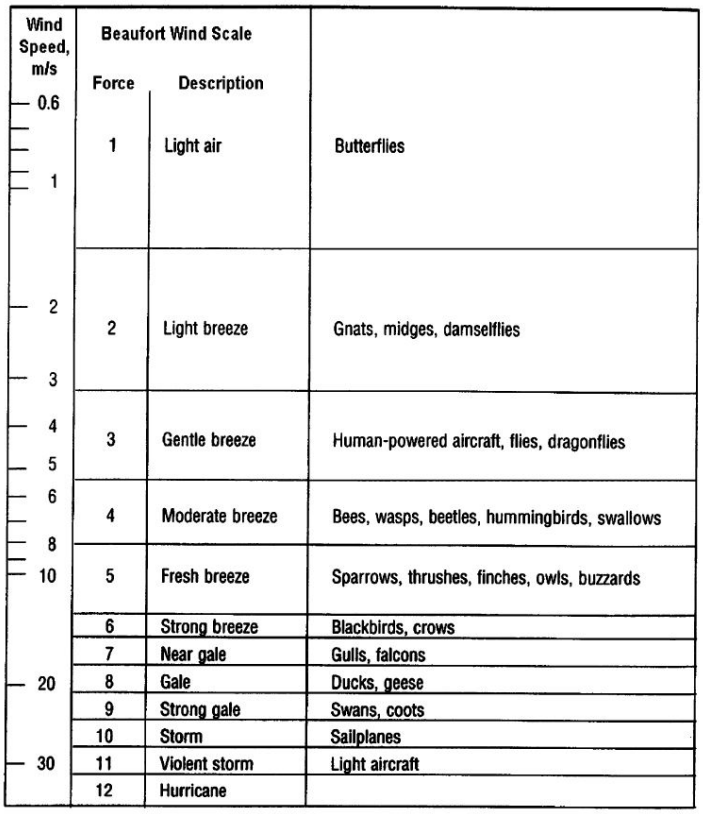

Figure 1.1: The flying speeds of birds and insects reproduced by Watkins [95] from Tennekes [88].

ing elements, starting with the original Pitot tube invented by Henri Pitot in the early 18th century to more complex thermal and optical methods such as hot wire anemometry (HWA) and particle image velocimetry (PIV) [12] nowadays. Figure 1.2 covers the most common measurement principles used in flow measurement.

Most conventional techniques based on pressure difference, heat convection, force and momentum have appeared more often in aerospace applications. With the development of micro air vehicles (MAV), conventional methods reach their limitations due to the larger sized measurement instrumentation and onboard integration capability. For example, although the current trend of flow measurement and visualization by digital particle image velocimetry (PIV) can provide detailed appearance of the air flow around an MAV, such a measurement set-up is not suitable for analyzing the three-dimensional flow field at a point on the MAV in real time [86]. This motivated researchers to look into the development of micro flow sensors that are suitable for MAV flow sensing and future applications.

American open source electronics manufacturer Modern Device designed one series of two wind sensors, RevC (older version) and RevP (newer version) that are potentially small enough and power efficient for MAV applications. Rev.C has less power consumption but worse measurement accuracy due to the lack of ambient temperature compensation. However its smaller size and power consumption is still attractive for drone applications, thus both sensors are investigated in this project. The performance of these small sized thermistor-based sensors with high sensitivity are worth investigating in different flight and airflow conditions to evaluate their possibility to be implemented on MAVs.

Delfly Nimble is an available flapping MAV platform that could use more than just the inertial sensors' information to improve its flight stability when affected by wind disturbances. So far no mature solutions involving wind disturbance monitoring have been implemented onboard a free

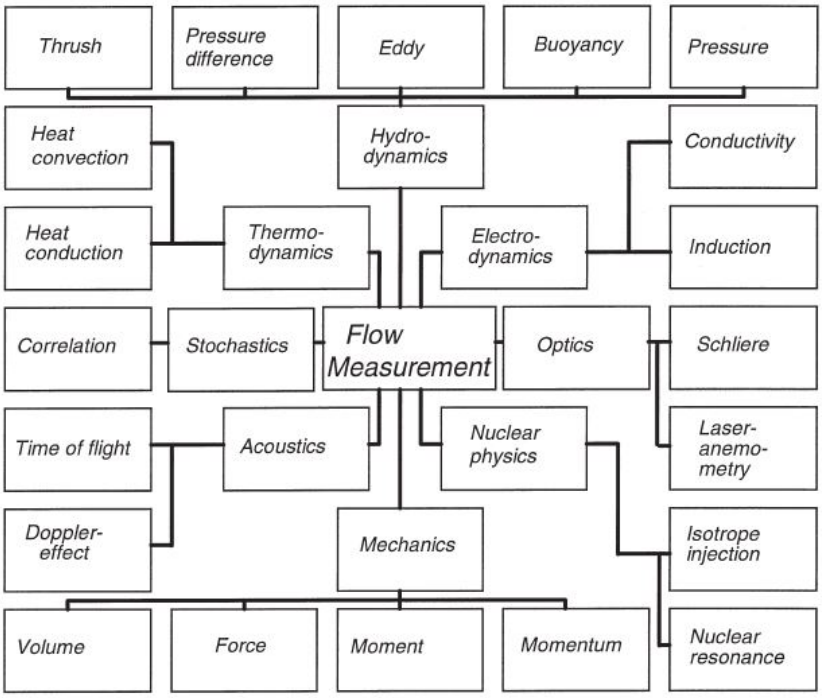

Figure 1.2: Physical principles of flow measurement techniques [90].

flying flapping wing MAV due to its size, mass, and power restrictions. If this proof of concept could be implemented with Delfly Nimble, then similar solutions could be applied to aerial vehicles of bigger sizes.

In Chapter 2, the literature review will go beyond the research motivation to present the state of the art research in miniature airflow sensors and outline how to approach the implementation of an airflow sensor onboard a flapping wing MAV platform to narrow down the engineering knowledge gap on flapping wing drone airflow sensing implementation.

1.2. Research question formation

Current flapping wing MAVs can only operate under little flow disturbance and the flight control could benefit significantly from such flow information. However, measuring disturbances at low airflow speeds is extremely challenging under strict sensor size and power constraints, plus the extra noise from the flapping-related vibrations. Therefore, the following research question is formulated:

Does the low-cost light-weight thermistor-based airflow sensor from Modern Device have sufficient performance to be used for airflow sensing onboard a flapping wing MAV under varying ambient flow and flight conditions?

Based on the main research question, the following sub-questions are formed:

1. How to calibrate a thermistor-based COTS (commercial off-the-shelf) airflow sensor with close-to-none manufacturer data sheet information?
2. How to evaluate the airflow sensor's performance under different flow conditions?
3. How does the aerodynamic perspective and control perspective affect the wind sensor's readings when onboard a flapping wing MAV platform?
4. What should be improved for the airflow sensor to be fully integrated on future FWMAV applications?

1.3. Research objective and outline

Airflow sensing onboard FWMAV is challenging from both electronics perspective and aerodynamic flow measurement perspective given the limited MAV power & payload, and the flapping motion's relative larger influence to low-speed air flow disturbances. The **research objective** of this MSc thesis project is to identify and minimize the engineering implementation challenges of a thermistor-based airflow sensor, and investigate its capability and reliability to sense low flow speeds onboard a FMWAV.

The first task of this thesis project is to investigate the measurement accuracy of one series of two thermistor-based airflow sensors and find out their limits in flow measurements. The airflow sensor with better performance will be integrated on the flapping wing MAV platform Delfly. First, mounted flight tests in the wind tunnel will be performed under different flow conditions to examine how the varying ambient flow and various flight control conditions influence the airflow sensor's measurement accuracy. Then repeatable tethered flight tests at hovering conditions with the airflow sensor onboard Delfly will be performed in the TU Delft Cyberzoo facility to compare with the wind tunnel test results.

The major sub-tasks of this research project can be divided as follows:

- Thermistor-based airflow sensors Rev C and Rev P calibration in a wind tunnel, with the potential increased accuracy at low flow speeds depending on the faculty calibration equipment availability
- Implement one airflow sensor with better measurement quality onboard the Delfly Nimble. Perform fixed flapping tests in a wind tunnel to simulate free flight conditions
- Tethered hovering flights in Cyberzoo with the airflow sensor onboard to examine its measurement performance compare to wind tunnel tests.
- Additional task if time permits: If the previous sub-goals prove the airflow sensor is promising during various sensor measurement campaigns, then perform tethered hovering flight tests in front of a self-built mobile wind generator in Cyberzoo under different types of wind disturbances.

The project is done in collaboration with the TU Delft Micro Air Vehicle Lab (MAVLab). The experiment set-up and data analysis process of the airflow sensor will be useful in a long term should the MAVLab explore other kinds of novel airflow sensors for drone applications.

The thesis report is divided as follows. Chapter 2 introduces the state of the art of airflow sensors and inspiration from literature on how to proceed the experiments on a flapping wing MAV platform. Chapter 3 explains the detailed test set-ups and preparation of the two main wind tunnel campaigns. Chapter 4 presents the result analysis of the first wind tunnel campaign where the candidate airflow sensors' calibration procedure and performances are characterised. Chapter 5 presents the result analysis of the second wind tunnel campaign where the selected ideal airflow sensor is mounted on a flapping wing MAV Delfly Nimble to further examine its measurement performance. Chapter 6 explains the process and results to validate the measurement capability of the airflow sensor in a tethered flight setting. These three major result chapters are outlined in Figure 1.3 with their key test components. Chapter 7 concludes the whole thesis project and recommends future work to improve the airflow sensor's design and areas for direct applications.

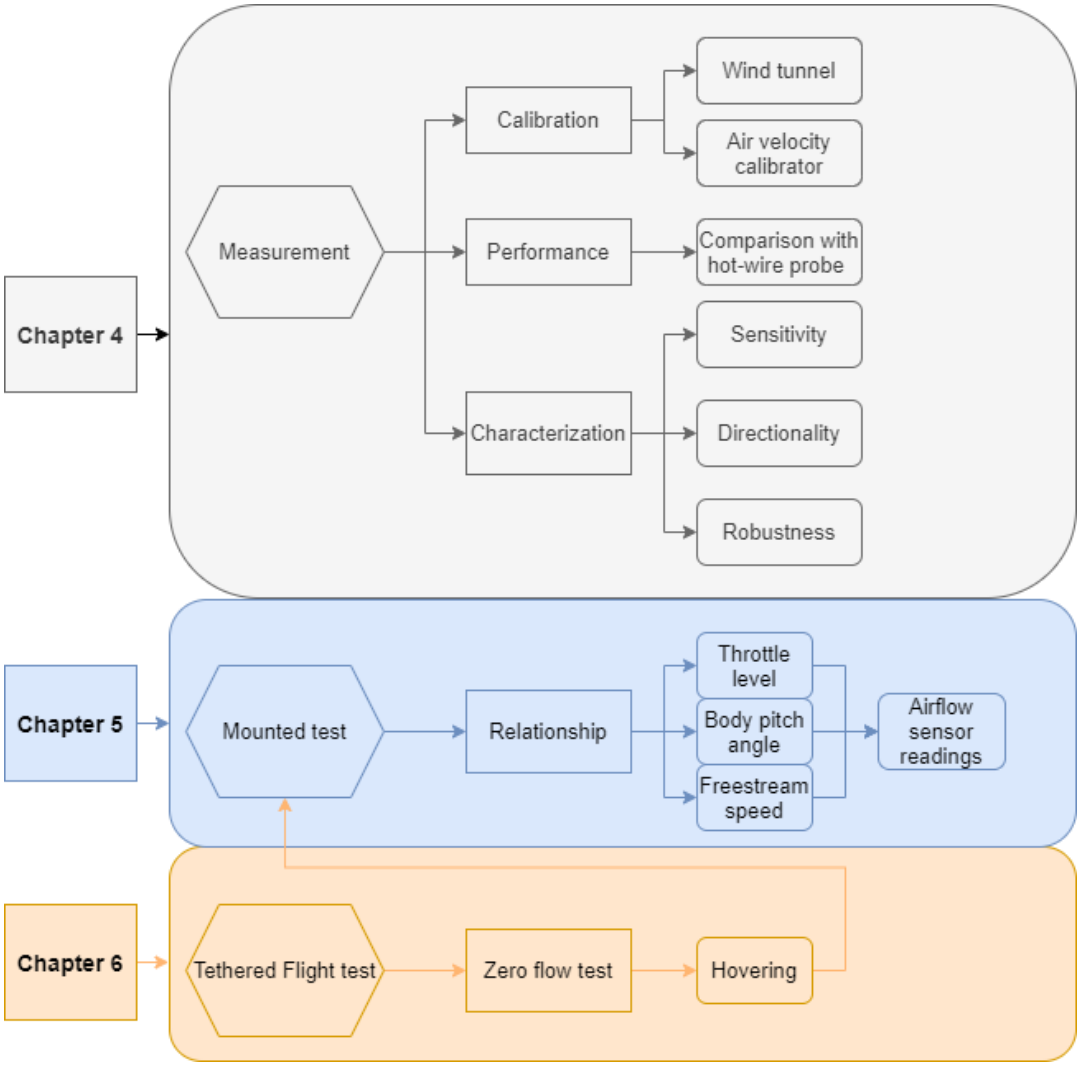

Figure 1.3: Thesis workflow chart with the corresponding chapters with results.

2

State of the art

Effective airflow sensing can bring time advantages to allow an MAV to react to external flow disturbances in unknown flight conditions compared to conventional methods. Conventional sensors such as inertial based sensors detect the vehicle's response to a wind disturbance rather than the disturbing phenomena themselves, causing the response-lag of attitude control [54]. Bio-inspired sensors based on insect or bird's mechanoreceptors and wind sensitive hairs could reduce the response-lag in sensing but are rather under-explored with very limited complete applications [53]]. If the information of incoming wind disturbance could be better known, it is proved that partial knowledge of wind speed and direction helps implement a disturbance rejection scheme that gives smaller position error and improve overall flight control stability [4] .

Therefore, finding a practical sensing solution that is low power with high sampling rate to sense wind disturbance and having an implementable solution on a drone platform could enlarge the active flight area for small-sized aerial vehicles. This is in particular challenging for flapping wing MAVs compared to quadcopters or fixed-wing drones, given the extremely limited carry payload and power limitations of current flapping wing MAV prototypes. Thus if it could be realized on a flapping wing MAV such as the Delfly Nimble, then other larger platforms would also be applicable.

Three main types of air flow measurement sensors are available: pressured based, thermal based, or elastic filament deformation based. Size, weight and power (SWaP) constraints could limit the applicable range of these sensors onto MAVs, in particular more difficult for flapping wing MAVs due to its even smaller size and limited payload. The following literature study will provide more details on flow sensing from bio-inspiration, the choice of a suitable airflow sensor onboard a flapping wing MAV, sensor working principle and performance characterisation, and the selection of an ideal testing environment needed for future experiments.

2.1. Bio-inspiration: flow sensors in nature

Animal flight (birds, insects) and swimming (fish) have been the inspiration for developing flow sensors over the decades. In the study of insect flight, Gnatzy et Tautz [28] have found that insects have the ability to detect air flow velocity by using the wind receptor hair at the tail. These receptor hair gives insects the information to utilize air flow to generate certain aerodynamic forces that allow them to achieve different flight manoeuvres [21]. Thus, as Ellington et al. [21] conclude that it is important to analyze the flow velocity distribution around the wing surface to further understand insect flight.

The function of the receptor hair is realized differently among species. For some species, such as an arthropod with filiform hair cell investigated by Albert et al. [32], uses a single hair cell as an independent sensing element illustrated in Figure 2.1a. For others, such as fish with its lateral

lines, use a bundle of hair cells jointly to achieve pointwise sensing [17]. According to Coombs [17], the fish lateral line forms spatially distributed sensing with directionally-sensitive sensors that can respond to the low-frequency water motions. Coombs further specifies that these motions are caused by the nearby moving sources, the animal's own movements, and ambient motions of the surrounding flow, and distortions in ambient or self-generated motions caused by the presence of stationary objects. Without advanced sensing and processing, it would be extremely difficult to differentiate these flow components. With an array of sensors that forms the lateral line, it provides useful information about the location, distance and direction of moving sources, which help fish to locate food source or avoid predators, similar to how insects use its wind receptor hair to escape from danger [28].

In the above cases, these individual or distributed sensing elements have better sensitivity over the state-of-the-art artificially made flow sensors. Yet, they provide great inspiration on design and manufacturing novel flow sensors by mimicking the biological features to equivalent mechanical features such as shown in Figure 2.1b for an artificial hair cell, of which the mechanical changes can be interpreted by electrical signals.

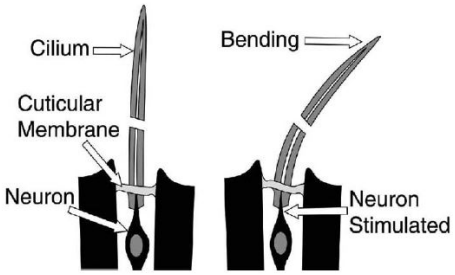

(a) Biological representation of the hair cell sensing mechanism [15]

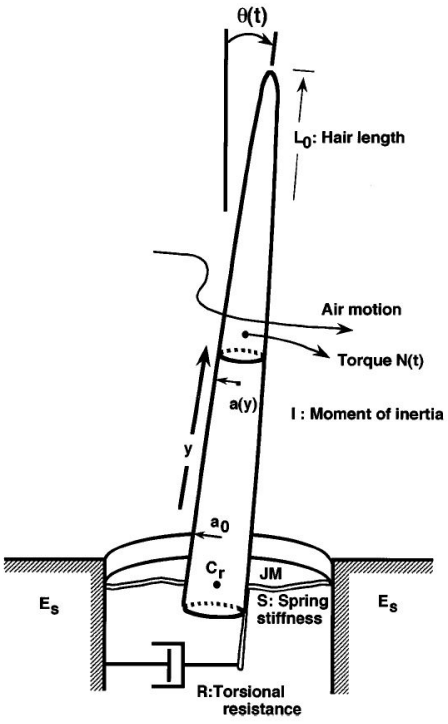

(b) Mechanical representation of the structure of a wind-receptor hair [77]

Figure 2.1: Biological and mechanical representation of a wind-receptor hair.

2.2. Major types of sensors for airflow measurement

With the development of semiconductor industry, micro flow sensors have been developed since the 1970s, with the first silicon based flow sensor being presented in 1974 [66] by van Putten and Middelhoek. Various types of sensors capable of flow sensing and measurement have been extensively studied over the years, from both the biology perspective and electronics perspective. A summary of the relevant review papers from the past three decades are shown in Table 2.1. A few highlights are explained in more details below.

Year	Author(s)	Hair-like	Artificial lateral line	Thermal based	Biology	Ref
1993	Brown and Fedde				✓	[10]
1997	Nguyen			✓		[58]
2002	Fan et al.		✓			[24]
2007	Liu	✓				[45]
2009	Jaalouk and Lammerding				✓	[33]
2011	Nawi et al.	✓				[51]
2012	Tao and Yu	✓				[87]
2012	Kuo et al.			✓		[43]
2014	Mohamed et al.				✓	[54]
2016	Liu et al.		✓			[46]
2018	Han et al.	✓	✓			[30]
2020	Jiang et al.	✓	✓			[34]

Table 2.1: Summary of review papers on the development of miniaturized flow sensors(Hair-like, artificial lateral line inspired, thermal based) and inspiration from biology.

Brown and Fedde pointed out in 1993 that the mechanoreceptors on or near flying animals' feather follicles may act like airflow sensors and allow the flying animals to adjust their flapping behaviour accordingly [10]. In 1997, Nguyen [58] summarized the first twenty years of development in micro-machining techniques for non-thermal flow sensors and thermal flow sensors.

Entering the twenty-first century, Tao et. al [87] reviewed the research trend of hair-like flow sensors and artificially lateral line sensors that were developed up till 2012. Liu et al. [46] reported only on the artificially lateral line sensors developed till 2016. In 2018, Han et. al [30] further reviewed on the key performance parameters, major category and future challenges of artificial hair-like sensors inspired by insects and fish. Overall, there has been a significant development of new materials and fabrication techniques to produce novel flow sensors inspired by nature. However, their design choices lack the practical aspects when considering the integration to an MAV scaling at different sizes and power consumption levels, especially for flapping wing MAVs. This is also partly due to the more recent development of flapping wing MAVs only in the recent two decades, which is made possible with the miniaturisation of sensors and actuators.

Conventional types of airflow sensors such as Pitot tube and hot-wire anemometers have been widely used in aviation industry and fluid dynamics studies over the decades. With the development of micro air vehicles, the need for light-weight airspeed sensors with high sensitivity and accuracy continuously grows as MAVs' flight control is more susceptible to airflow changes due to its smaller size. Numerous non-conventional types of airflow sensors have been developed over the years that are more suitable for MAV applications. Based on the operational principles, there are a variety of bio-inspired sensors for airflow sensing and airspeed measurement. This includes strain based elastic filament velocimetry [62, 69, 83, 86, 99] with piezoelectric or piezoresistive materials, acoustic load [20], thermal load [14, 75], transducing methods such as resistance [29, 79] and capacitance [3, 76], magnetic [7], and optical [31, 73] .

In this section, three of the most studied types of airflow sensors for airspeed measurement will

be introduced with more details, of which the comparison will lead to the selection of an airflow sensor later used in this thesis project.

2.2.1. Pressure based: pitot tube

Pitot tubes remain the most cost-effective method for measuring the mean velocities in fluid flow, and are capable of being easily integrated onboard a moving test object. To get more angular information with respect to incoming flow, multi-hole probes such as a 3-hole or 5-hole pressure probe are often used. With a multi-hole probe system such as the 5-hole one shown in Figure 2.2, five total pressure ports are located on its conical head from P_0 to P_4, and four static pressure ports P_s slightly downstream of the head. As the pressure distribution on the probe's head is a function of its geometry and of the flow direction, by sampling this distribution in five locations P_0 to P_4, the direction and magnitude of the flow velocity can be determined. This technology provides more air flow velocity information than the traditional pitot tube, which is being restricted to only one velocity component [12]. Accurate measurements of wind flow field in temporal and spatial domain can be obtained using arrays of such multi-hole Pitot probes [95].

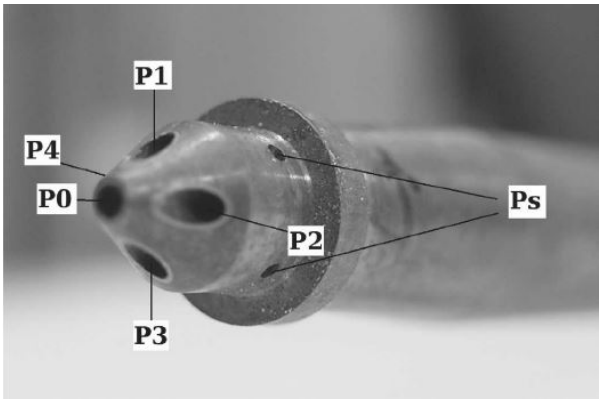

Figure 2.2: A five-hole pitot tube manufactured by TU Braunschweig that can measure five differential pressures at the tip of the probe. The four smaller circumferential holes P_s are the static pressure holes [92].

Inspired by the sensory function of bird's feathers capturing flow disturbance information before it causes an inertial response on the MAV, Mohamed et al. [55] developed a turbulence mitigation system with a 5-hole pressure probe as shown in Figure 2.3. The system proves to be advantageous compared to inertial-only MAV control system. With the extra two holes on the side compared to a 3-hole pressure probe, this probe can provide information on variation in the side slip angle, besides the relation to angle of attack and freestream velocity. The derivation of the differential pressure equations that relate the pressure difference to flow angle information are explained in full details by Rodi and Leon [72] and the key equations are summarized below.

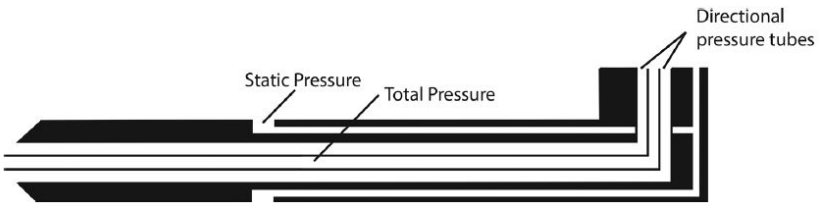

Figure 2.3: Specially fabricated multi-hole probe [55].

As the pressure distribution on a sphere is well-known, the differential pressures measured from the different ports are assumed to be located on a spherical surface, as the example in Figure 2.2. The pressure coefficient is calculated from Equation 2.1 where P is the pressure at solid angle ϕ from

the stagnation point (in this case, ports P_1 to P_4 are located 45° with respect to the center port P_0) and P_∞ is the freestream pressure. Their difference is divided by the dynamic pressure $q = 1/2\rho U^2$, which can then be related to the angle ϕ and a sensitivity factor (f = 9/4 for potential flow [44])

$$C_P = \frac{P - P_\infty}{q} = 1 - f \sin^2 \phi \tag{2.1}$$

Four differential pressures are measured with the pressure ports: $P_0 - P_\infty$ approximates the impact pressure at small angles, $P_1 - P_3$ in the vertical plane of the probe relating to the angle of attack α, $P_4 - P_2$ in the horizontal plane of the probe relating to the side slip angle, and $P_0 - P_4$ also a measure of the impact pressure. After some conversion with trigonometric relationships, Rodi and Leon concludes the differential pressure relations in Equation 2.2.

$$\begin{aligned}
\Delta P_0 &= P_0 - P_\infty = q\left(1 - \frac{(f-1)\left(\tan^2\alpha + \tan^2\beta\right)}{1 + \tan^2\alpha + \tan^2\beta}\right) \\
\Delta P_\alpha &= P_1 - P_3 = 2fq\frac{\tan\alpha}{1 + \tan^2\alpha + \tan^2\beta} \\
\Delta P_\beta &= P_4 - P_2 = 2fq\frac{\tan\beta}{1 + \tan^2\alpha + \tan^2\beta} \\
\Delta P_R &= P_0 - P_4 = fq\frac{(1 - 2\tan\beta - \tan 2\beta)}{2\left(1 + \tan^2\alpha + \tan^2\beta\right)}
\end{aligned} \tag{2.2}$$

The ΔP_α,ΔP_β,ΔP_R equations in Equation 2.2 can be solved analytically to obtain $\tan\beta$ and $\tan\alpha$ without knowing the dynamic pressure q or the sensitivity factor f as shown in Equation 2.3.

$$\begin{aligned}
\tan\beta &= \left(\sqrt{2 * \left(\Delta P_\beta^2 + 2\Delta P_\beta \Delta P_R + 2\Delta P_R^2\right)} - \Delta P_\beta - 2\Delta P_R\right) / \Delta P_\beta \\
\tan\alpha &= \tan\beta \frac{\Delta P_\alpha}{\Delta P_\beta}
\end{aligned} \tag{2.3}$$

Before the use of a multi-hole pressure probe, it would rely on a calibration procedure to relate the angles and flow information with the differential pressures measured by the different ports. This can be achieved with a reference source such as a wind tunnel with speed logging and a microcontroller capable of measuring angle changes.

This multi-hole pressure probe configuration has been used for disturbance rejection control on a fixed-wing MAV with the Slick 360 Micro model by van der Sman et al. [80], which has a weight of 115 grams for the basic setup, and 130 grams for the setup with the multi-hole pressure probes. This extra 15-gram payload consists of the multi-hole pressure probes, acrylic tubes connecting the pressure probe to a differential pressure sensor, and the differential pressure sensors itself. On either side of the wing, the probe is placed 15 cm ahead of the leading edge of the wing. Although the instrumentation is already small in size compared to typical pitot-static tube system and light in weight, this measurement setup is still too heavy and too big to be adapted to an even smaller flapping wing MAV.

Despite the rich angle information that can be derived from the differential pressure measurements, which can be very useful for control schemes in response to the incoming air flow, pressured-based methods also suffer from limited sensitivity once in the low speed regime. As Pitot-static tube's measurements would lead to dynamic pressure through the difference between total pressure and static pressure, which has the following scaling relationship with velocity,

$$q \propto U_\infty^2$$

detecting small pressure changes at very low air flow speeds would require larger transducers with higher sensitivity [84]. This would scale up the instrumentation size and cost quickly. And the measurement results at small dynamic pressure change are often less accurate and noisy with the current commercially available pitot tubes for MAV applications.

Table 2.2 lists a few commercially available pressure sensors with their operating pressure ranges, operating current, operating supply voltage, and unit weight according to their respective data sheets. The selection of this group of sensors is goal-oriented, being low power consumption, light weight and capable of operating in lower pressure ranges. These COTS sensors are often fully calibrated, temperature compensated for sensor offset, sensitivity and temperature effects, and non-linearity with the help of an on-board integrated circuit. There is no direct mentioning of a minimally detectable speed from measured differential pressure according to the product data sheets. The only available information is from practical experience (Source: Paparazzi UAV wiki) for the Eagle Tree MicroSensor, having a minimally measureable speed around 4m/s and a resolution of 0.3 m/s. The common feature shared among these sensors is that the increase of error band at a lower pressure range, with Honeywell HSC series at ±2.5% around ±160pa. The frequency response is also limited, with Eagle Tree MicroSensor having a 10Hz refresh rate for example.

Name	Pressure [Pa]	Current [mhA]	Voltage [V]	Weight [g]
Honeywell HSC 1.6MD	± 160	3.1	3.3	1
Sensortechnics LBAS250BF6S	± 250	1	5	N/A
Eagle Tree MicroSensor	N/A	N/A	3-16	4
MS4515DO	500	3	3.3/5	3
AMS5812	517	5	5	3

Table 2.2: Examples of commercially available pressure sensors more suitable for low-pressure ranges.

Due to the limitations in frequency response from the pressure transducer and the bulky setup with the tubes, pitot tube methods lack performance for a multi-point distributed measurement or higher order turbulence characterisation compared to thermal based hot wire methods. Besides, pitot tube measurements often need to be corrected for viscous effects, shear and turbulence [12] in unregulated flow, which is more challenging considering the rapid changing flow environment MAVs operate in.

In summary, integrating a Pitot tube sensing system onboard a flapping wing MAV would require to resolve the instrumentation size, weight, and transducer sensitivity at low dynamic pressure change, which is extremely challenging given the current Pitot tube's technology limitations.

2.2.2. Thermal based: hot-wire or thermistor

Thermal based techniques relies on the amount of heat transfer between the measuring element to the flow environment. This includes the convection to the fluid, conduction to the measurement instrumentation support, radiation to the ambient environment, and the heat stored in the measurement instrumentation itself. Common measurement instrumentation involves using a hot-wire sensor or a thermistor.

Conventional hot-wire anemometers with probes made of platinum or tungsten wires are widely used in flow measurement where flow velocity fluctuations of fine scales and of high frequencies [35] are being investigated. This kind of flow environment poses a continuous challenge for MAV operations with an increasing vulnerability to turbulence as the MAV's size and speed reduces [81].

Among the two major types of hot-wire anemometers, constant temperature (CT) and constant current (CC) types, the constant temperature anemometer(CTA) is primarily used nowadays for velocity measurements in isothermal flows due to its high frequency response and temporal resolution [11], which would suit better for MAV applications. A constant current anemometer(CCA) is used in conjunction with a resistance-wire that can measure temperature fluctuations for non-isothermal flow measurement applications [11].

Four major types of anemometer probes exist as shown in Figure 2.4: miniature wires, gold-plated wires, fibre-film and film-sensors [35]. The wire or film is stretched between two supporting prongs which hold the sensor immersed in the fluid. Among them, the first choice for potential flow measurement instrumentation would be the miniature wire due to its high frequency response and relative low cost in case of repairing since the wire is normally 5 μm in diameter and easily breakable. In terms of flow directional sensitivity, the hot-wire probes are also available in more than one measurement dimension as shown in Figure 2.5 where the magnitude and direction of the flow velocity vector can be measured and extracted through certain mathematical relationships when the sensors are placed under different angles with respect to the flow vector [35]. This is realizable as heat transfer from a hot-wire depends on the flow yaw, pitch and rolls angles, where locally the flow velocity component normal to the wire dominates, thus the pitch angle is more critical [48].

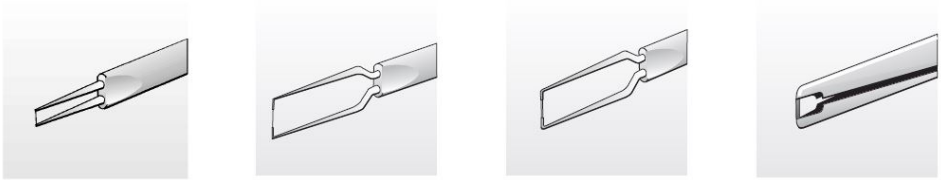

Figure 2.4: 4 types of anemometer probes [35]

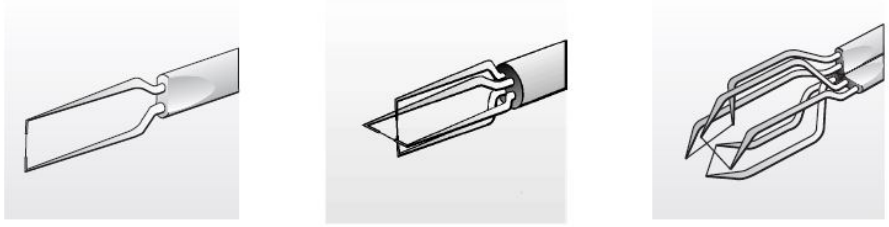

Figure 2.5: One-, two- and three-dimensional versions of anemometer probes for more information on flow direction and magnitude [35].

To better understand the key parameters in thermal-based anemometry and the energy balance in the measurement instrumentation, a differential element shown in Figure 2.6 with length dx and cross-sectional area A of a hot-wire sensor is used as a basic model for heat transfer analysis. This

method is adapted by Lomas [48] in part from Davies and Fisher [18].

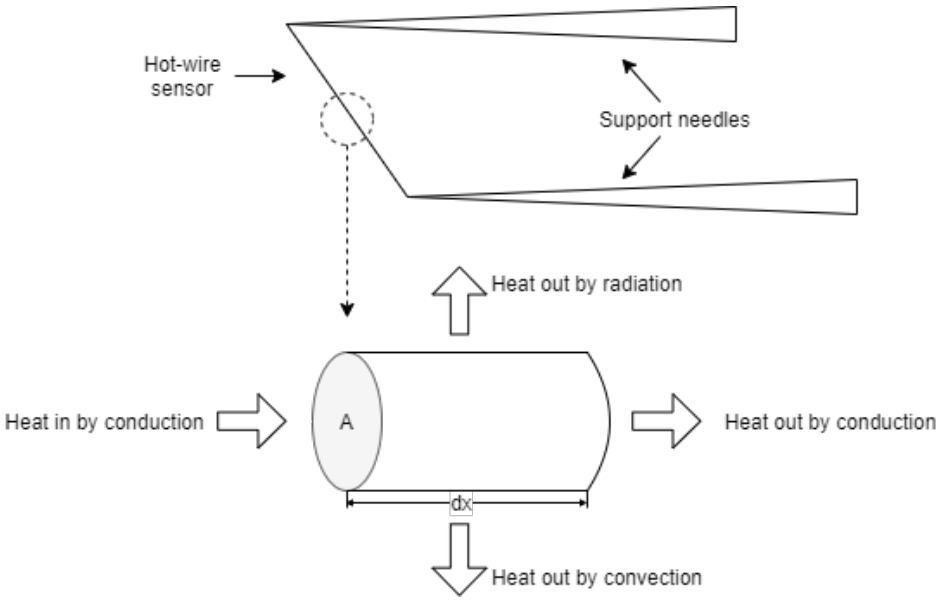

Figure 2.6: The differential element for a hot-wire sensor, reproduced from *Fundamentals of Hot Wire Anemometry* (Lomas 1986 [48]).

The rate of conduction heat transfer into the left and out of the right end of the differential element is:

$$\text{Conduction heat transfer rate in left end } = -\, k_s A \frac{\partial T_s}{\partial x}\bigg|_x$$

$$\begin{aligned}\text{Conduction heat transfer rate out right end } &= -\, k_s A \frac{\partial T_s}{\partial x}\bigg|_{x+dx} \\ &= -k_s A \frac{\partial T_s}{\partial x} - A\frac{\partial}{\partial x}\left(k_s \frac{\partial T_s}{\partial x}\right) dx\end{aligned}$$

where k_s is the thermal conductivity coefficient for the hot-wire sensor material. A Taylor series expansion is used to the conduction heat transfer out of the differential element, which will be useful later for the energy balance equation.

The heat generation rate and heat storage rate of the hot-wire sensor are expressed as following where I is the heat current through the hot-wire, ρ_r is the resistivity of the hot-wire sensor material, ρ is the density of the sensor material, and c is the specific heat capacity of the sensor material:

$$\text{Heat generation rate} = \frac{I^2 \rho_r}{A} dx$$

$$\text{Heat storage rate} = \rho c A \frac{\partial T_s}{\partial t} dx$$

The heat transfer rate out of the differential element through convection and radiation to the fluid are expressed as following where d is the sensor diameter, h is the convective heat transfer coefficient, T_f is the fluid temperature, T_s is the sensor temperature, σ is the Stefan-Boltzmann constant, T_{sur} is the temperature of the surroundings, and ϵ is the emissivity of the sensor:

$$\text{Convection heat transfer rate out} = \pi d h (T_s - T_f) dx$$

$$\text{Radiation heat transfer rate out} = \pi d \sigma \epsilon (T_s^4 - T_{sur}^4) dx$$

Finally, with conservation of energy, the above terms yield to the following energy balance differential equation for the heat balance in a hot-wire sensor:

$$A\frac{\partial}{\partial x}\left(k_s\frac{\partial T_s}{\partial x}\right)+\frac{I^2\rho_r}{A}-\rho cA\frac{\partial T_s}{\partial t}-\pi dh\left(T_s-T_f\right)-\pi d\sigma\epsilon\left(T_s^4-T_{\text{sur}}^4\right)=0 \tag{2.4}$$

Assume the radiation heat transfer is negligible, sensor temperature T_s does not vary with time, and thermal conductivity k_s maintains constant, then Equation 2.4 can be further simplified to the following:

$$Ak_s\frac{\partial^2 T_s}{\partial x^2}+\frac{I^2\rho_r}{A}-\pi dh\left(T_s-T_f\right)=0 \tag{2.5}$$

This differential element heat transfer analysis reveals that for thermal-based methods, the following factors are the influential factors when conducting flow velocity measurement experiments:

- The measurement element(i.e. hot wire or thermistor)'s material properties(e.g. size, thermal conductivity and resistivity)
- The convective heat transfer coefficient between the measurement element and the fluid
- The temperature of the measurement element
- The temperature of the ambient flow

Due to the high frequency response and temporal resolution of a CTA anemometer, it is popular among experimentalists for measurements of the speed and direction of the flow, turbulence measurements and simultaneous measurement of the flow field [11, 48]. However, the sensing wire of the hot-wire anemometer breaks easily due to dust, debris, impact with any physical objects, or sudden wind gusts [95]. It is often placed at a secure and fixed position during an ongoing experiment along with the bulky set-up for signal conditioning and data acquisition, thus not suitable as a practical measurement instrumentation for onboard flow measurements of MAV applications.

Despite the disadvantages of traditional hot-wire anemometry, in recent years, there have been some innovative attempts in making micro-wire-bonded hair-like hot-wire anemometers for air flow sensing [75]. The method originated from silicon-based hot-wire flow sensors which were introduced in the late 1980s [85]. And the full transduction path from mechanical, to thermal and electrical signals [61] have been commercialized successfully with different micro-machining techniques [43] nowadays, using different configurations based on thermoresistive, thermoelectric, or thermoelectronic sensor materials. However, these silicon-based hot-wire flow sensors are more often designed for flow measurement inside an enclosed tubular package [75], which makes them less applicable for open measurement environment. Sadeghi et al. designed a low-cost hot-wire sensor as shown in Figure 2.7 using the standard wire-bonding method for sensor formation[75, 76], which allows the sensor to be suitable for external air flow measurement in open test environment. This wire-bonded hair-like hot-wire anemometer has high sensitivity with minimally detectable flow of 0.01 m/s, and a wide dynamic range up to 17.5 m/s. With an array of at least two sensors, directional flow measurement can also be achieved, which would be useful for flow sensing when an arbitrary flow is present.

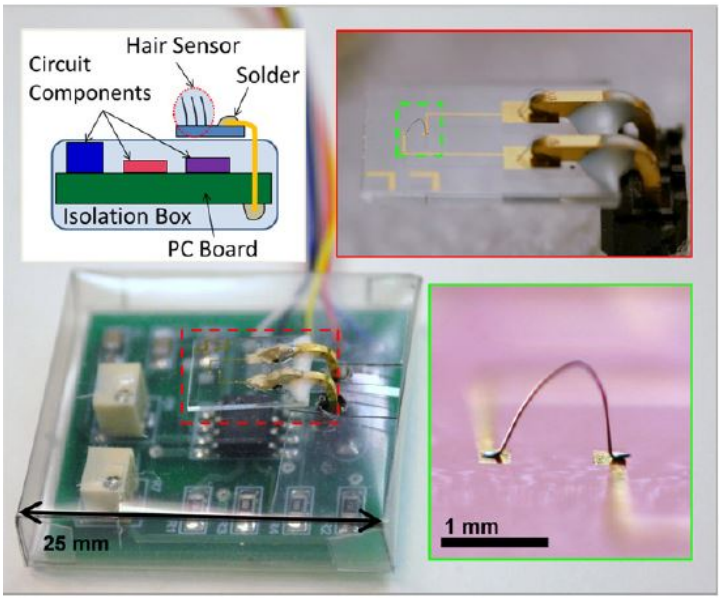

Figure 2.7: The full sensor package integrated with the fabricated hot wire using bond wires, PCB and flow isolation box set-up [75].

Ye et al. [100, 101] further improved the bonding wire technique with a sensing element scheme of eight heaters and eight thermistors integrated on one sensor as shown in Figure 2.8. This arrangement consists of two wind sensing groups (colored in blue and red separately in Figure 2.8a) which allows two independent flow measurement groups that can be later processed to obtain the final measured flow speed and direction. Such an octagon-sensing design improves 2D micro-machined thermal wind sensor's directional accuracy tremendously, with the airflow direction covering the full range of 360 degrees with a maximum error of ±1.5 degrees. This high directional sensitivity is very difficult to achieve and extremely useful in MAV applications where flow field is unknown with high turbulence.

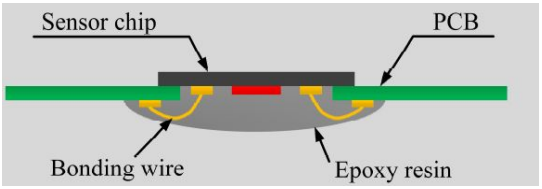

(a) Cross-sectional view of the self-packaging method [101]

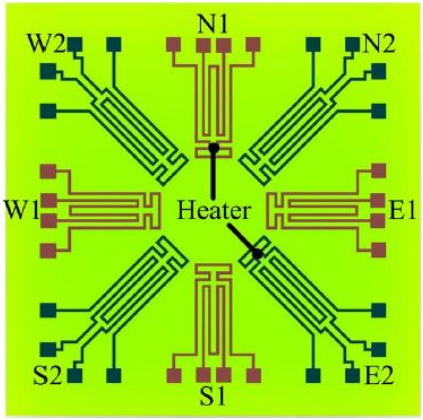

(b) Layout of the two measurement groups(Red: N1-E1-S1-W1; Blue: N2-E2-S2-W2 [100]

Figure 2.8: The design of the octagon-shaped 2D thermal flow sensor.

In summary, once designed with safer packaging and more long-endurance materials, air flow sensors with thermal transduction have great potential to be used in MAV applications where the moving vehicles experience large inertial forces, which minimally affect thermal transduction [75]. With a high frequency response and temporal resolution, thermal-based air flow sensors are also

suitable in rapidly changing flow environment where great operational challenges still remain for MAVs. However, the customized design and fabrication techniques could put pressure on cost and time. Integrated packaging with minimal size, weight and power consumption along with high directional sensitivity still remain a challenge for the sensor design and application.

2.2.3. Elastic filament velocimetry

Elastic filament velocimetry is a method to measure fluid velocity through correlating the fluid forcing with the internal strain of an elastic filament [12]. Figure 2.9 illustrates a modeling of this process with a fixed ended beam. Cantilever-type structure is also common in design [62]. The elastic filament is usually fabricated with an electrically conductive nano-scale ribbon. The ribbon will deflect due to drag from the passing fluid. The deflection due to the combination of the elongation, thinning and piezoresistive effects of the nano-ribbon leads to a change in resistance across the ribbon. This strain gauge effect enables the correlation between the resistance of the elastic filament and the fluid velocity [27]. Such an idea has been developed for over two decades [14, 24, 62].

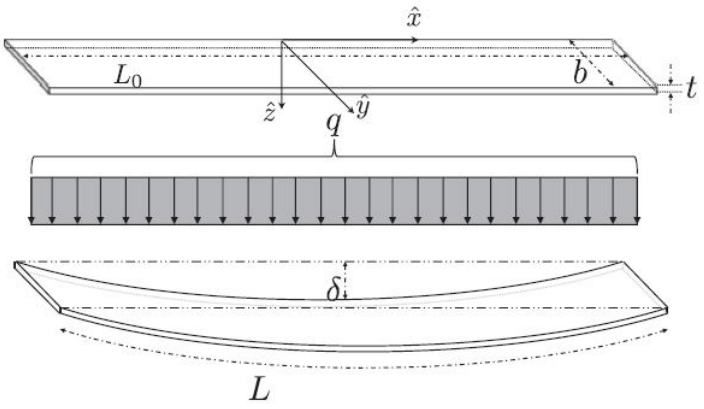

Figure 2.9: A schematic diagram of the nano-ribbon of length L, width b, and thickness t, with a geometrical orientation such that flow is in the direction of $\hat{z}$, causing a distributed load q that leads to a center-line deflection of δ [27].

The earliest air flow sensor inspired by wing receptor hairs of insects was developed by Ozaki et al. [62] in 2000. They translated the bio-inspiration from an insect mechanoreceptor (cereal filiform hairs of Gryllus) studied by Gnatzy and Tautz (1980 [28]) and the cercal wind-receptor hairs of cricket modelled by Shimozawa et al. (1998 [77]) into one of the earliest artificially made sensory hair that is capable of air flow sensing.

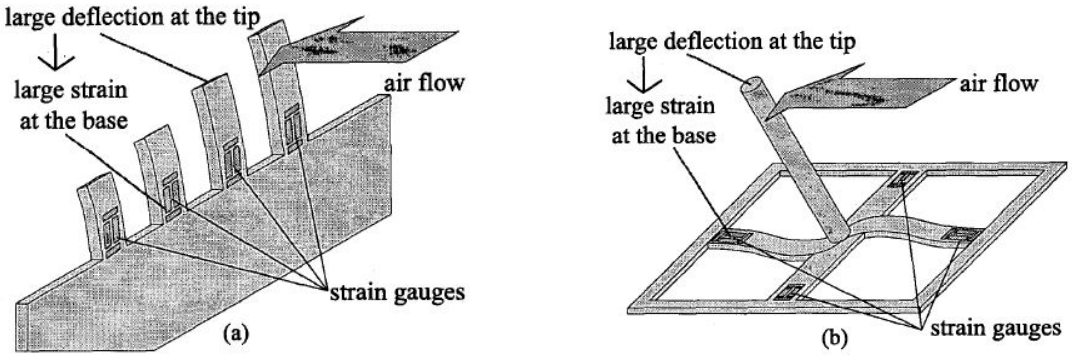

(a) (b)

Figure 2.10: Schematic diagrams of 1-DOF and 2-DOF air flow sensors inspired by wind receptor hairs of insects.

A 1-DOF and 2-DOF artificial sensory hair are fabricated as shown in Figure 2.10. Both sensors have cantilevers and strain gauges integrated at the bottom of the deflect-able filament. The 1-DOF sensors can be made into an array of sensors where each of the sensor consists of a cantilever with a different length. Together they can measure different frequencies of the air flow simultaneously due to the correlation of flow speed with different amount of deflection in the cantilevers. Note that as the 1-DOF sensor measures predominantly the velocity component that is perpendicular to

the cantilever surface, flow directionality information can not be extracted from the measurement outputs, hence Ozaki et al. [62] also developed a 2-DOF sensory hair to account for the flow direction measurement. The 2-DOF sensor is made of a long cantilever sensory hair wire attached to the center of the cross-shaped beam where multiple strain gauges are located, thus allowing the measurement of the direction angle of the air flow.

Both the 1-DOF and 2-DOF air flow sensors output voltage that is proportional to the air flow velocity. A strict linear relationship is not achieved as shown in Figure 2.11a with the example of the 2-DOF sensor, which is common for novel sensors at prototyping stage. This would require proper calibration for each sensor before it can be put into practice. Furthermore, The 2-DOF sensor displays a clear sinusoidal relationship in terms of the air flow incoming direction angle with the sensor output voltage.

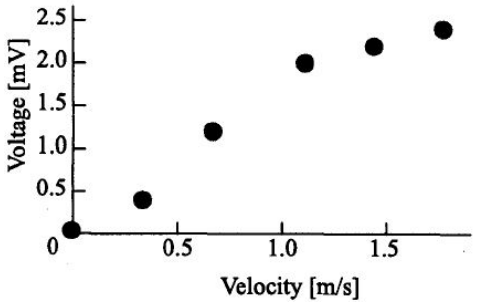

(a) The relationship between the air flow velocity and the sensor output voltage

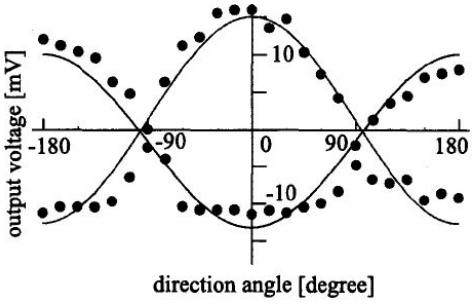

(b) The relationship between the air flow incoming direction and the sensor output voltage

Figure 2.11: 2-DOF air flow sensor output voltage relationship with flow velocity and incoming flow direction angle [62].

Air flow sensors utilizing elastic filament velocimetry often have sufficient measurement sensitivity [62, 86] which can be easily configured through modifying the mechanical stiffness of the sensory filament (e.g. thickness and elasticity) and the piezo-resistivity of the composite [84]. Often times, the sensor's micrometer magnitude of length, width, thickness and measurement sensitivity down to centimeters per second makes elastic filament based hair-like sensors a very promising candidate for air flow sensing in weight and size restricted MAV applications, in particular in flapping wing MAVs where low airspeeds and wind speeds are often present.

In practice, the construction and formation of piezoelectric or piezoresistive air flow sensors that can be used in elastic filament velocimetry is flexible in the sense that the relative geometry and size of the sensing filament can be customized based on the measurement needs in certain flow regime, thanks to the manufacturing technique improvement in microelectromechanical systems (MEMS). However, access to clean room with proper fabrication tools and materials is not always guaranteed and requires collaboration between the aerospace research lab with electrical engineering facilities. For example, the sensor developed by Chen et al. [15] can measure air flow speeds around 0.1 m/s but the production processes require a clean room. Only until recently, in 2020, Sundin et al. [84] proposed a soft material air flow sensor that can be used for MAV applications with a simpler manufacturing method and low-cost materials. The procedure can be carried out using common laboratory tools without the necessity to use a clean room.

A mature solution of hair-like air flow sensor fully integrated on a free-flying flapping wing MAV does not yet exist. The earliest attempt towards this direction has been the 1 μm thin piezoresistive cantilever air flow sensor Takahashi et al. put on the leading edge of an insect-like flapping wing [86] as shown in Figure 2.12. To clarify the distribution of the air flow around the flapping wing surface for further applications, a distributed measurement at multiple points on the flapping wing would be essential. Takahashi et al. proposed such a distributed sensing concept on the flapping wing as shown in Figure 2.12a and also proved through experiments (similarly to Ozaki et al. [62]'s) that the

hair-like piezoresistive cantilever has high sensitivity and directivity. However, actual in-flight tests to further characterize the sensor's performance has not been done, possibly due to the lack of a flapping wing MAV platform.

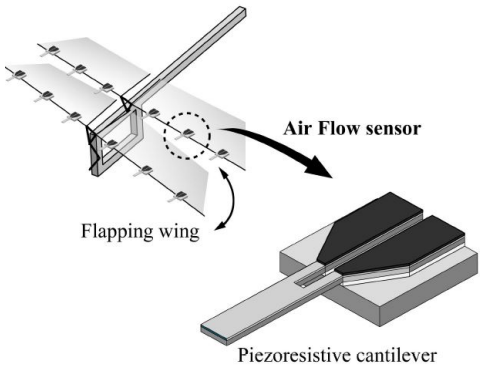

(a) A concept of piezoresistive cantilever-type air flow sensors attached to the leading edge of the wing [86]

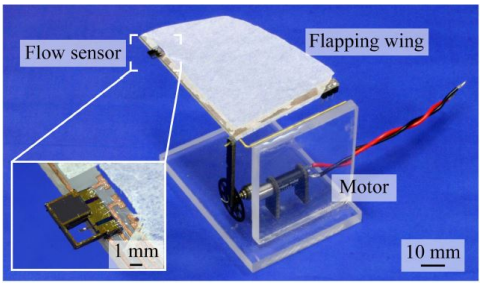

(b) Experimental set-up for proof of concept [86]

Figure 2.12: Air flow sensor tested on an insect-like flapping wing [86].

A more recent attempt to apply a lightweight hair-like air flow sensor on an MAV has been done by Gollob et al. [29], not on a flapping wing MAV, but on a small quadcopter Crazyflie 2.0 manufactured by a Swedish company Bitcraze. Their air flow sensor uses a rigid flap (cantilever) attached to the top of a flexible conductive pillar as shown in Figure 2.13a. This flap deflects with varying incoming wind speeds and its increased surface area compared to thin sensory hair allows the sensor to be more sensitive to the air flow. Like other hair-like air flow sensors [62, 84, 86], Gollob et al. report that their sensor uses a fabrication process that allows the tuning of sensor geometric parameters such as pillar and pad height, width and thickness, for easy integration onto an MAV with different application purposes. After sensor behaviour characterisation through wind tunnel flow tests and actual onboard flight tests, Gollob et al. conclude that although their air flow sensor can not be used for precise flow measurement around the quadcopter, it is sufficient to sense when ground effect is occurring above a set threshold. This proof of concept can motivate future applications such as terrain avoidance for outdoor MAVs. The air flow sensor's low mass at 0.04 grams and low power consumption at 42 μW in operation makes it also a promising candidate for flapping wing MAV air flow sensing applications.

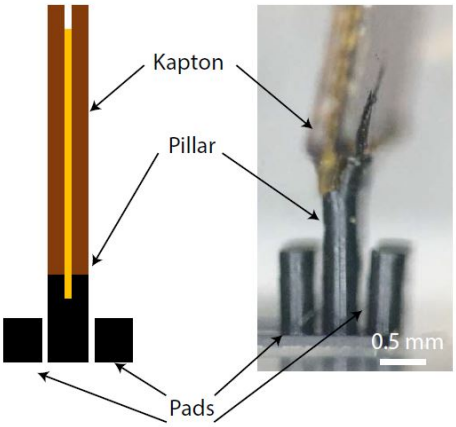

(a) Side view of the air flow sensor schematic (left) and the actual sensor (right) [29]

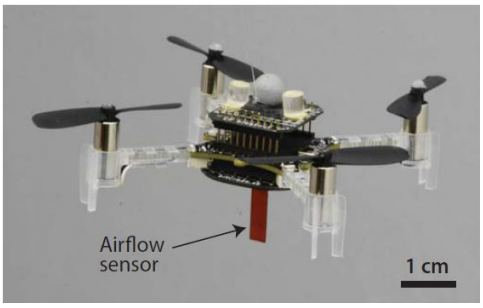

(b) Crazyflie 2.0 quadcopter with air flow sensor attached to the center of the bottom side [29]

Figure 2.13: Lightweight air flow sensor tested on a quadcopter.

2.2.4. Summary of sensor comparison and final selection

Few conventional or non-conventional sensors satisfy all the needs of high sensitivity, high sampling rate, lightweight, and energy efficient for smaller MAV applications such as flapping wing MAVs. To be able to meet the above requirements as much as possible for optimal air flow sensing and airspeed measurement on a flapping wing micro air vehcile (FWMAV), Han et al. [30] summarized a list of key performance parameters that researchers should take into account. This instrumental list is further expanded to the following requirements when choosing a sensor and performing measurements:

- The sensor used on the FWMAV must be of a size and with sensing capabilities suitable to achieve the ideal spatial and temporal resolution for FWMAV flight, i.e., high sensitivity and resolution [57]
- Low power consumption [22] for the sensor due to the FWMAV's short battery power duration. If distributed sensing of airflow is needed, this requirement will even be more strict
- Sensor miniaturization with high integration capability [19] as FWMAV can carry extremely limited payload
- Simple sensor fabrication, ideally without the need to use a clean room, or commercially available off-the-shelf (COTS) sensor products for easier access to repeatable and sufficient testing
- The sensor should be flexible enough to be installed on curved surfaces if needed due to the aeroelastic interactions of the non-rigid flapping wings [102]
- Onboard flight measurements should be taken at appropriate height above the ground during the proof of feasibility stage tests, to minimize the atmospheric boundary layer effects [95].
- The sensing quality and flight stability should be maintained even under interference or in harsh environment [42]

Hot-wire based methods are not considered here due to the extremely fragile nature of the wire. The common engineering decision making method Pugh Matrix is used here to aid the selection of an optimal air flow sensor that could be the most promising in applying to a flapping wing drone. It is balanced based on what is possible based on theoretical design and what could actually be achieved under practical restrains. As shown in Table 2.3, thermistor based and elastic filament based methods are quite close in terms of overall performance.

Key criteria	Weight	Pitot tube	Thermistor	Elastic filament
Size and weight	3	0	1	2
Sensitivity to low flow speed	3	0	1	2
Frequency response	2	0	2	1
Easy access	2	2	1	0
Onboard integration	1	2	1	0
Weighed total		6	13	14

Table 2.3: Pugh Matrix for practical decision making in choosing an air flow sensor for flapping wing MAV applications.

A few of the most promising candidates from elastic filament based methods based on the literature study are summarized in Table 2.4. However, due to limited access to these research prototypes, these types of sensors will not be investigated in this research project. Two COTS thermistor-based sensors shown in Figure 2.14, manufactured by American company Modern Device are selected to be studied and used during the project. Their basic properties and features are summarized in Table 2.5

Year	Sensor	Mass [g]	L × W [mm]	Power [mW]	Range [m/s]	Ref
2009	Aiyar et al.	10^{-5*}	1.5× 0.4	0.087	0~16.9	[6]
2012	Liu et al.	10^{-4*}	3 × 0.3	$0^{\dagger}$	0~19.5	[47]
2018	Gollob et al.	0.04	20×5	0.042	7~8.3‡	[29]
2020	Sundin et al.	‡	15 ×0.3	0.1	4~11	[84]

Table 2.4: Comparison of existing lightweight, low-power consumption air flow sensors that may be usable for flapping wing MAV applications.

(a) Latest sensor model: RevP

(b) Previous sensor model: RevC

Figure 2.14: Modern Device wind sensors RevP and RevC.

Modern Device Rev sensors can directly interface with the ADC on a microcontroller without the need of external electronics such as bridge circuits and amplifiers like some flow sensors do [6, 47], which makes them easy to integrate for direct use.

	Rev.P (Latest model)	Rev.C (predecessor)
Dimension [mm]	17.27 x 40.37 x 0.64	17.30 x 40.00 x 0.60
Weight [g]	1.34	1
Supply voltage [V] (Ideal)	9 ~ 12 (12V)	4 ~ 5 (5V)
Working current [mA]	30 ~ 40	20 ~ 40
Measurable speed [m/s]	0 ~ 67	0 ~ 26.8
Thermistor	Requires a higher voltage to heat the thermistor to operational temperature	Less stable and less accurate
Temperature calibration	Exists ambient temperature compensation	N/A

Table 2.5: Specification comparison of the latest version of the air flow sensor Rev.p and its predecessor Rev.C.

2.3. Modern Device airflow sensor calibration and performance characterization

2.3.1. Sensor working principles

Knowledge of the sensor's working principles helps develop a deeper understanding of the sensor's operation and performance. Therefore, the two key components in the sensor circuitry (Wheatstone bridge circuit and feedback amplifier) are briefly studied and summarized in this section.

The Modern Device's two airflow sensors' circuitry essentially contain a Wheatstone bridge and a feedback amplifier as illustrated in Figure 2.15. A Wheatstone bridge is commonly used in electronics to generate an error signal proportional to the difference between a variable sensor signal (hot-wire probe R_w or sensing thermistor in the case of the Modern Device sensor) and a reference

*Estimated from dimensions provided in reference by Gollob et al. [29]

†External voltage source is not required as the voltage can be generated directly from the piezoelectric material PZT through harvesting the air flow energy

‡Not provided by the author explicitly or approximated from plots

signal from an adjustable resistor R_3 (e.g. the 10 $k\Omega$ reference PTC thermistor in RevP). The Wheatstone bridge is balanced when the voltage difference between e_2 and e_1 is zero. When the bridge is balanced, the following relationship holds where A is the bridge ratio:

$$A = \frac{R_2}{R_1} = \frac{R_3}{R_w} \tag{2.6}$$

To realize the Wheatstone bridge circuit as a constant temperature anemometer, the bridge voltage E is varied in order to maintain bridge balance when the measured flow is changing. Before the system is in operation, the adjustable resistor R_3 is set to a resistance value that is higher than what would be needed to balance the bridge. To maintain the bridge balance, according to the bridge ratio relationship, the resistance value of the sensor R_w needs to increase. This is realized when power is applied and the feedback amplifier G increases the heating current, which increases the sensor temperature and thus increases the sensor's resistance and balance the Wheatstone bridge. An increase in flow velocity cools the sensor mainly through convective heat transfer and unbalances the Wheatstone bridge. Modern feedback amplifiers have a very fast response [11] to increase the sensor heating current to maintain the sensor temperature at a constant level despite the flow velocity changes. The voltage difference across the Wheatstone bridge is proportional to the flow velocity and thus can be used as an indicator to flow speed change [48]. Note that the feedback amplifier, along with the Wheatstone bridge, and the sensor element govern the dynamic response of the anemometer [11], which makes the design choice of these components crucial for a constant temperature anemometer.

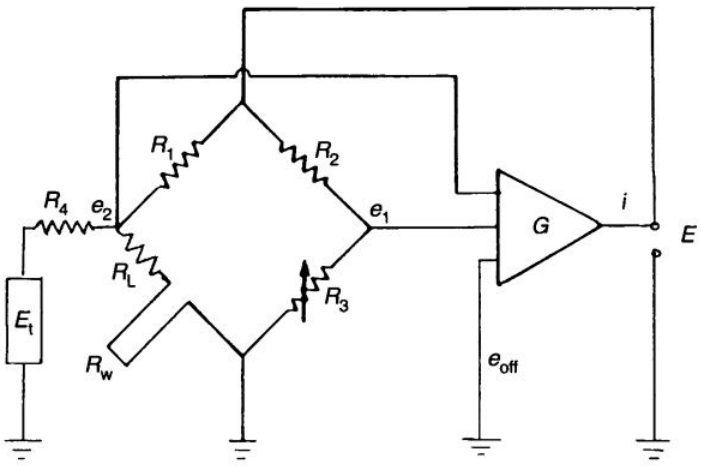

Figure 2.15: Diagram of a constant temperature anemometer(CTA) containing a Wheatstone bridge, a feedback amplifier, and an electronic-testing sub-circuit E_t [11] R_L is negligible during the explanation of working principles.

The RevP version of the Modern Device air flow sensor has onboard hardware compensation for ambient temperature change, through a low-power linear active thermistor integrated circuit MCP9701SOT-23 that is marked S_1 in Figure 2.14a. Temperature compensation is needed to adjust the circuitry's performance to compensate for effects caused by ambient temperature fluctuations. This gives RevP an advantage of built-in hardware temperature calibration but it is not perfect, as the MCP9701SOT-23 integrated circuit has a $\pm 4°C$ (max) accuracy between $0 \sim 70\ °C$ according to data sheet from the manufacturer MICROCHIP.

2.3.2. Calibration method

To be able to use the air flow sensors with reliable measurements onboard a flapping wing MAV, the sensors first need to be calibrated with a reliable reference flow, as the manufacturer Modern

Device provided no detailed data sheet with pre-calibrated coefficients that can relate the sensor's analog voltage outputs to a certain flow speed. A wind tunnel with precise fan speed control and flow measurement set-up would be an ideal environment to generate reference flow speed. Two calibration methods are available to obtain an optimal fit that can correlate the air flow sensor's flow and temperature analog voltage outputs to a certain flow speed.

As the air flow sensor behaves similarly like a hot-wire anemometer, the conventional calibration model King's Law used in hot-wire calibration is adopted here as the first calibration method. With this method, only the air flow analog voltage output is needed from the sensor. The flow during calibration is assumed to be isothermal, and the flow density ρ is assumed to be constant. The air flow sensor is placed in a body-fixed coordinate system. King's Law is most commonly used to determine the non-linear relationship between the fluid velocity and measured voltage, as shown in Equation 2.7, where E is the measured voltage, U is the fluid velocity. A, B and n are calibration coefficients depending on the anemometer property that will be obtained through the optimal fit. The value of n is usually set to 0.5 but in some cases this constant could be adjusted to 0.45 or even 0.4 ([11]).

$$E^2 = A + BU^n \tag{2.7}$$

To obtain the voltage-velocity relation with the King's Law coefficients, the calibration of the air flow sensors is conducted through curve fitting with a fourth-order polynomial ([82]) expanded from Equation 2.7 as follows:

$$U(E) = P_4E^4 + P_3E^3 + P_2E^2 + P_1E + P_0 \tag{2.8}$$

The second calibration method incorporates the use of the temperature analog feedback from the air flow sensor into a custom fit calibration function. The air flow sensor's calibration has a best fit composed of a parametric function with a linear and power curve component for the temperature verses voltage output, and the air flow speed verses voltage output, respectively ([65]). This relationship can be expressed in Equation 2.9 where V_{out} is the air flow analog voltage from the sensor, T is the ambient temperature converted from the temperature analog output from the onboard temperature measurement, v is the measured air flow speed $[m/s]$ and a, b, c, d are calibration coefficients acquired from the best fit.

$$V_{out} = a + bT + cv^d \tag{2.9}$$

Therefore, the measured air flow speed can be written as:

$$v = \left(\frac{V_{out} - a - bT}{c}\right)^{1/d} \tag{2.10}$$

Prohasky and Watkins (2014) proposed using the robust absolute residuals (LAR) surface fitting method and the trust-region fitting algorithm to remove the clear outliers and calibrate the sensor. An ideal calibration and fitting method suitable for this extremely low flow speed applications shall be further examined in this research project, with the help of the wind tunnel tests' data.

2.3.3. Temperature effects: correction methods for drift in the air temperature

As the flapping wing MAV could potentially operate in an environment where the air flow temperature T_a could vary with time, the output voltage from the air flow sensor will be affected by the variation of T_a, which is a common phenomenon for thermistor based sensors. Such temperature effects could either be caused by heat source/sink leading to slow drift, or temperature fluctuations in a non-isothermal flow [11]. The common correction procedure for drift caused by temperature effects in fluid with fluctuating temperatures has been established in great details for constant temperature hot-wire typed anemometers. Peter Freymuth concluded most of these proposed velocity and temperature response equations into 3 major categories [26]:

1. The simplest and most practical method is to assume the heat transfer from the sensor probe to be proportional to a product of temperature difference between the sensing element T_w and the flow temperature T_a, and a calibrated velocity-voltage relationship:

$$E^2 = f(U)(T_w - T_a) \tag{2.11}$$

2. The convective heat transfer is expressed in a non-dimensional form using the Nusselt number Nu, Reynolds number Re, and the Prandtl number Pr

3. Perform a direct calibration of the anemometer under different temperatures to establish the temperature dependence of the anemometer output voltage signal for a given resistance setting of the sensing element

Method 1 requires the least amount of calibration and its methodology could potentially be applied to the Modern Device air flow sensor given that the temperature profile of the sensing element can be made known through further electronics studies. Method 3 requires the most effort to carry out but its completeness and accuracy with actual testing data under various flow temperatures can be used to evaluate the effectiveness of Method 1 or 2.

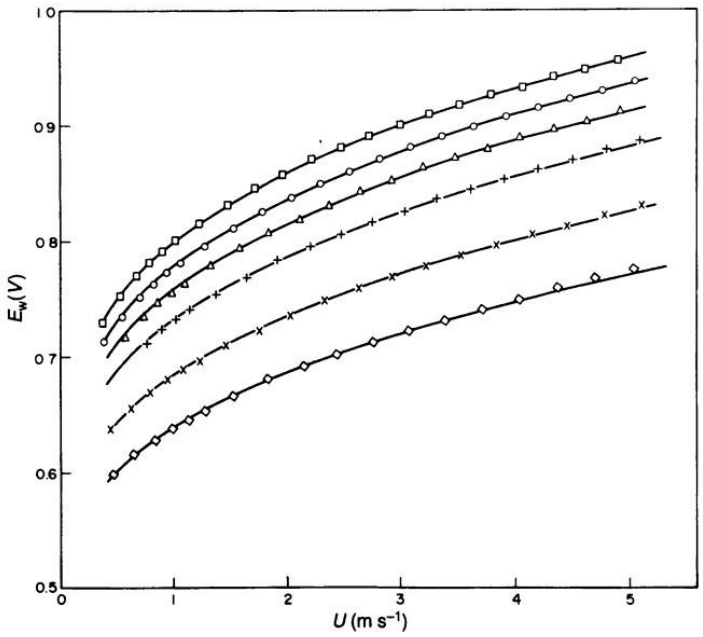

Figure 2.16: The dependence of the hot-wire voltage E_w and air velocity U under different ambient fluid temperatures T_a: (□ : 283 K; ◯ : 293 K; △ : 303 K; + : 313 K; × : 333 K; ◇ : 353 K;) T_w = 473K Reprinted by Bruun 1995 [11] from Koppius and Trines 1976 [40], with kind permission of Elsevier Science Ltd from the *Internal Journal of Heat and Mass Transfer*.

Figure 2.16 shows the experiment result of establishing the velocity and temperature sensitivity of a constant temperature hot-wire anemometer using Method 3. It can be seen that at the same air flow velocity U, if flow temperature T_a increases, for example the flapping wing MAV flies in a warmer room, the anemometer output voltage will be smaller. This is reasonable as less heating current is needed to balance the Wheatstone bridge given the reduced temperature difference between the sensor and the environment, which leads to less connective heat transfer. And at the same output voltage level E, if the flow temperature increases, the measured flow velocity will be higher.

2.3.4. Measurement directional dependency evaluation in laminar flow

Prohasky and Watkins (2014) suggested that the Rev.P sensors are unreliable for excessively directionally variable flows. However, the Rev.P sensor seems to be capable of measuring average wind velocities (V_{avg}) when the direction of incoming wind flow is known reasonably well. Such measurement accuracy is reported to be within $\pm 0.5\ m/s$. Thus further measuring the angular response of different incoming wind conditions are valuable to understand the sensor's performance limits and could potentially provide insights for sensor redesign to improve the hot-wire's angular response. The horizontal and vertical directional dependency data shown in Figure 2.17 is incomplete in terms

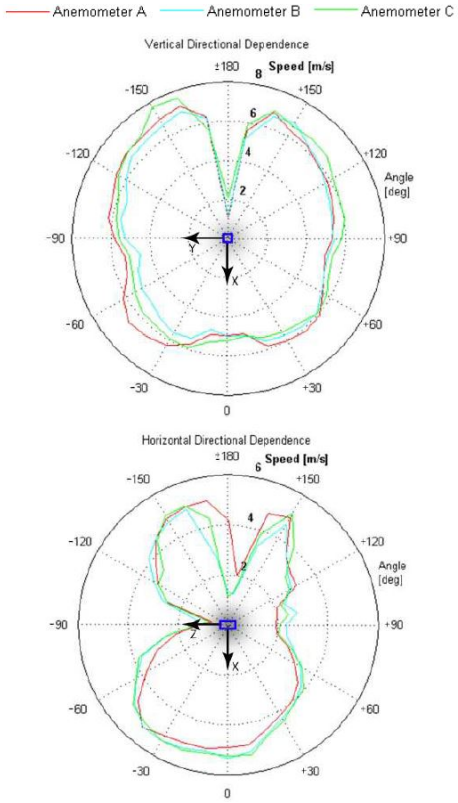

Figure 2.17: Directional dependency of average flow speeds about the XY plane (top) and the XZ plane (bottom) measured repetitively three times, each time using one Rev.P wind sensor [65].

of rotational degree of freedom. However, it is still useful for this project's measurement validation purpose. In Figure 2.18, different rotation planes are illustrated with the RevP sensing element as the original of the coordinate system. This shall allow the evaluation of wind speed measurement quality in XY, XZ, YZ planes which gives a more complete profile of the air flow sensor's directional sensitivity.

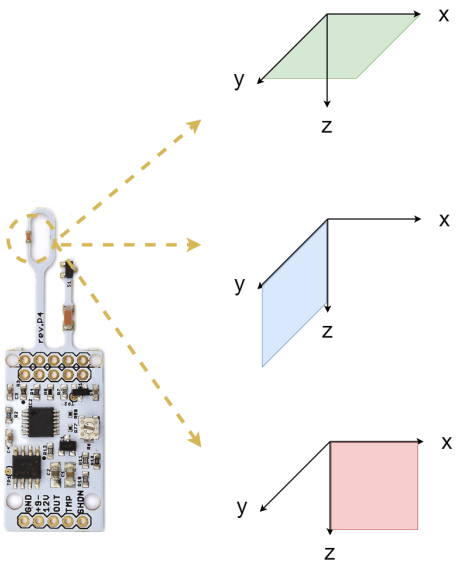

Figure 2.18: Air flow sensor rotational plane definition.

2.3.5. Frequency response in turbulent flow

Hot-wire based methods' primary role as a research tool is for turbulent flow studies. The hot-wire sensing element and associated data acquisition electronics shall be able to provide instantaneous response to any fast flow change ([11]). Therefore, knowing the air flow sensor's frequency response in turbulent flow is of crucial importance. Figure 2.19 shows a sample frequency response plot with power spectral density(PSD) versus frequency. The -5/3 slope is plotted as reference. Similar inquiries into frequency response in turbulent flow and observe how the frequency response drop will provide key metrics to how the low-cost air flow sensor perform, since the outdoor flying environment of drones are usually turbulent with different levels of flow disturbances.

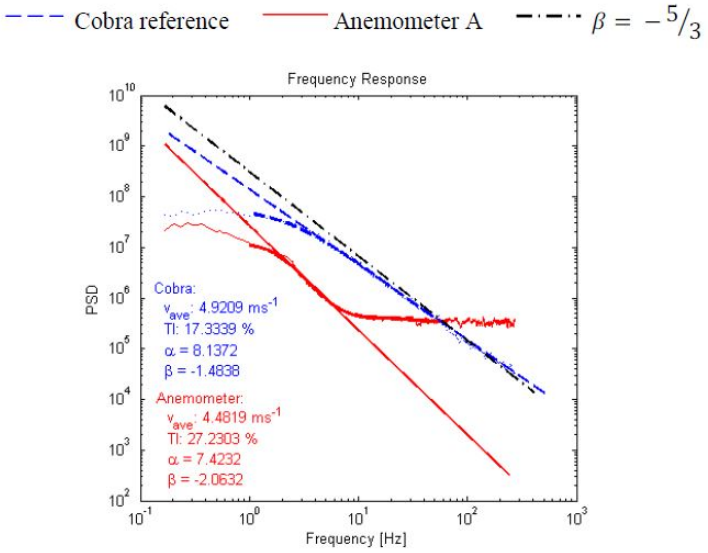

Figure 2.19: Turbulence levels and spectral data from the Rev.P sensor and the reference Cobra probe - -5/3 Kolmogorov slope is plotted as reference [65].

2.4. Flapping wing MAV platform: the Delfly Nimble

As mentioned previously in Section 2.2.3, an fully integrated air flow sensor onboard a flapping wing MAV does not yet exist. Two development challenges continuously remain, the light-weight high sensitivity air flow sensor itself, and a functional flapping wing MAV platform that can carry such a sensor. More challenges surface during the actual integration phase when flapping vibrations affect flow measurements and the added-on sensor brings extra challenges in power and weight balance.

The Delfly flapping wing drone family has gone through a series of design iterations over the years since 2005, the most significant one being from tailed Delfly II to the tailless Delfly Nimble. Delfly II has a tail which passively stabilize the MAV while Delfly Nimble is tailless and requires active attitude stabilisation. The Delfly Nimble is chosen as the flapping wing MAV platform for this thesis project as it is possible to carry extra 1-2 grams' payload with the current thrust-to-weight ratio and the relative longer battery life. And it is easy to control for repeatable flight tests above a fixed waypoint. The key components and performance specs of Delfly Nimble are summarized in Figure 2.20 and Table 2.6. To hover Delfly Nimble in a free flight, a flapping frequency of 17 Hz is needed [36]. The top forward speed is 7 m/s but the most energy efficient cruise speed would be around 3 m/s [36].

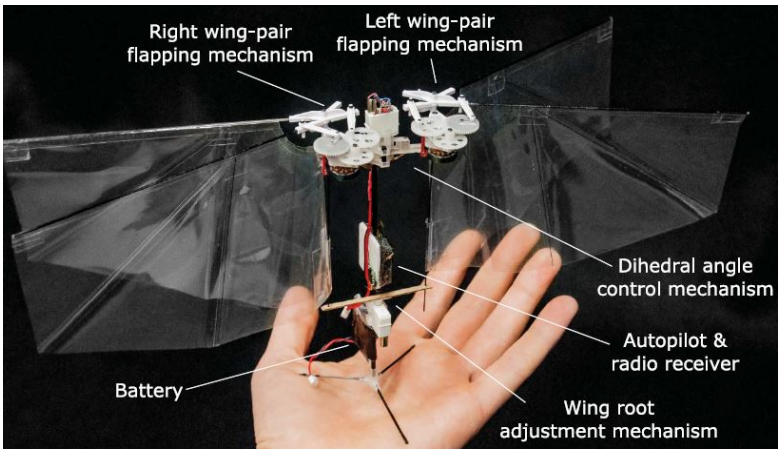

Figure 2.20: Description of the key components of the flapping wing drone Delfly Nimble, an insect-inspired free-flying robotic platform ([36]).

Key parameter	Value	Unit
Takeoff weight	28.2	[g]
Wing span	33	[cm]
Flapping frequency	17	[Hz]
Thrust-to-weight ratio	1.3	[-]
Top speed	7	[m/s]
Flight endurance	5	[min]

Table 2.6: Specification and performance of the original Delfly Nimble [36] at hover conditions.

Delfly Nimble is a programmable and autonomous free-flying MAV through bio-inspired motion changes of its flapping wings ([36]). The onboard DelTang Rx31 radio receiver and the ESP8266 ESP-09 Wifi module allows data-link between the autopilot (Lisa/MXS v1.0 [1] with a STM32F405 processor) onboard Delfly, the ground station and the OptiTrack motion capturing system in Cyberzoo testing facility in TU Delft Aerospace Engineering faculty.

2.5. Integration considerations for the air flow sensor

2.5.1. Sensor placement location

To place the air flow sensor onboard the flapping wing MAV Delfly Nimble, a stable measurement location is crucial as structural vibration during flapping will cause induced movement which adds an unwanted component in the air flow sensing. Two possible locations inspired by birds' biological features could be ideal location to place the air flow sensor, first being on the flapping wing leading edge considering birds can detect wind oscillation through the deflection of covert feathers there as illustrated in Figure 2.21, second being at the head position due to the head stability commonly present in animal flight.

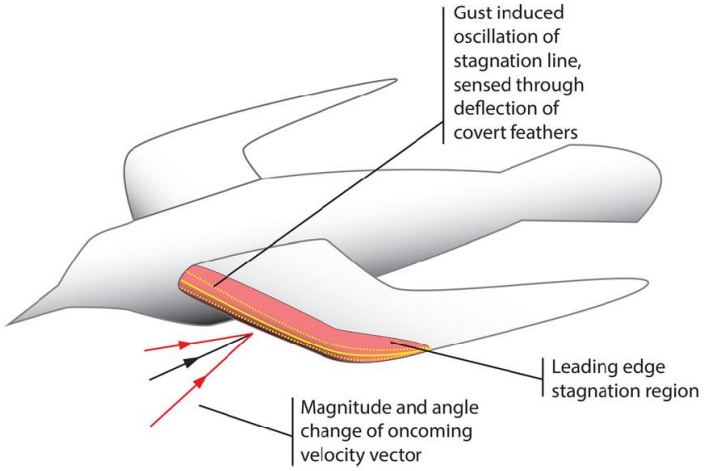

Figure 2.21: Bird gust detection by sensing the stagnation line movement on the wing leading edge[55].

Given the flapping wing MAV Delfly Nimble's design features, for practical reasons, it is extremely difficult to attach an air flow sensor with relatively significant PCB board size onto the thin foil of the wing and the D-shaped leading edge carbon rod. Besides, the size and weight of the air flow sensor will change the aerodynamic forces and moments on one side of the wing causing large yawing and potentially rolling moments, which makes the drone flight control extremely challenging and practically not flyable. Thus, despite being a biologically more advanced solution, wing leading edge placement of the air flow sensor is currently not an option.

This leaves the head position the more suitable placement location. In the field of avian image stabilization studies, birds' ability to stabilize their head with respect to the horizon is crucial for their navigation and flight path planning [41, 94]. The avian head and body stabilization capability have been previously shown in birds sitting on perches with forced vertical oscillations [38]. Pete et al. [64] observed that in long-neck birds such as swans or geese, their necks make large compensatory motions to attenuate the oscillatory displacement of the body throughout the wingbeats. They use whooper swan as a study platform. Through flight video data and modeling of the swan's neck suspension, Pete et al. verified that these swans indeed can passively attenuate oscillatory body displacements during flapping like what has been observed previously. What's even better is that with additional mass carried in the beak, the swan's head is even robust to mild gusts.

Thus, inspired by the fact that the head position is passively stabilized during flapping flight and an ideal stable location with less oscillations, the "head" of the Delfly Nimble, which is the tip of the body fuselage, will be chosen as the placement location for the air flow sensor.

2.5.2. Vibration effects

For flapping wing drones, due to the flapping motion, body vibrations continuously exist. For tailed MAV designs such as Delfly II, the tail section serves as a natural damper to dampen out the

oscillations induced by the motion of the flapping wings. Yet these mechanical vibrations are still significant enough to disturbs the onboard accelerometer's measurements. These measurement distortions from a Delfly II are of the magnitude of 2 m/s^2, which is larger than the accelerations of interest of the order of 1 m/s^2 [93]. Verboom et al.[93] proposed a mechanical damping mechanism with a foamy substructure and flapping cycle based filtering to mitigate the onboard state estimation deficiency caused by disturbance of the accelerometer measurements. This further enables a control scheme that improves the autonomous flight capabilities of a flapping wing MAV.

For Delfly Nimble, a 3D-printed (with PLA materials) light-weight miniature structure is used to tightly bond the autopilot to the body fuselage rod, which aims to further reduce the influence of mechanical vibrations causing the onboard IMU measurement noise. Furthermore, a small 3D-printed structure should be made to tightly bond the air flow sensor to the tip of the fuselage rod, in the hope of reducing the moment arm as the air flow sensor will be at the furthest from the center of gravity and thus have the largest vibration amplitude.

2.6. Testing environment

To create repeatable flow tests under controlled flow environment, which is needed for air flow sensor calibration and onboard flapping wing MAV tests, wind tunnels are ideal testing locations.

Gollob et al. [29] performed tests in wind tunnel to characterize their lightweight contact-resistance-based air flow sensor used for quadcopter ground effect sensing under varying airflows. A minimum air flow necessary for sensor functionality is identified through wind tunnel tests. The sensor support set-up in the wind tunnel with approximately 50x50 cm^2 cross-sectional area is illustrated in Figure 2.22a, where the sensor is distanced from the wind tunnel wall to ensure laminar flow.

To extend to the minimum flow detection level of the air flow sensor, wind tunnel testing environment alone will not be sufficient. As conventional wind tunnels are not capable of providing consistent high-quality low-speed flow along with reliable measurements at these low flow speeds less than 0.5 m/s, the calibration of the air flow sensor at low speeds will be difficult. Extra test equipment to ensure the flow quality at low speeds will have to be sought during the testing stage of the thesis. It is worth noting a novel method of creating low-speed flow through relative movements[49, 75]. The air flow sensor is mounted on an enclosed rate table and is being moved through stagnant air at a constant speed. The rate table moves at a controlled speed and the whole table system is placed in an enclosed chamber to minimize the ambient influence. In this way, low flow speed is created indirectly through the relative speed of the rate table to the stagnant air, with a precisely controlled manner in the low-speed range.

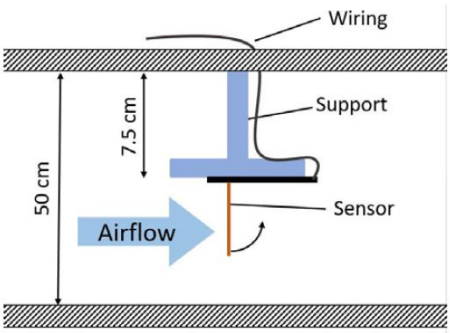

(a) Wind tunnel set-up for air flow sensor characterisation [29]

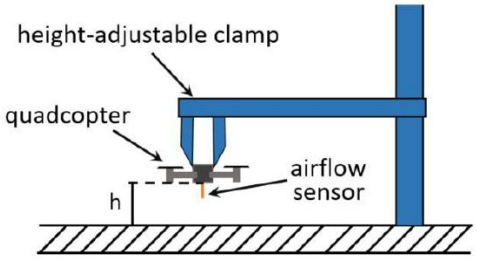

(b) Onboard experimental set-up to test air flow sensor's behavior [29]

Figure 2.22: Lightweight air flow sensor tested on a quadcopter.

The sensor calibration and performance evaluation will be done to both versions of the air flow sensors, RevC and RevP, given that RevC has the advantage of less power consumption and being lighter, while RevP has less dependency on flow directions and is more accurate according to the manufacturer Modern Device. After this stage, the sensor with overall better performance will be placed onboard the flapping wing MAV platform Delfly Nimble. A full integration of the air flow sensor to Delfly Nimble is not yet possible due to power restriction. Nimble's HP-G550 1S 180mAh LiPo battery at a full charge state is only capable of 4.2 V. Adding an extra step-up voltage regulator to provide sufficient voltage to the air flow sensor is theoretically possible but the extra add-on weight makes the actual flight impractical. Therefore, before aiming for a direct tethered flight with external power and data acquisition cables in an unregulated flow environment, evaluating the air flow sensor's data quality under controlled flow environment and repeatable flight conditions should take over priority in the testing stage. Figure 2.22b provides a starting point for a fixed test set-up with adjustable clamp to position the drone in a regulated testing environment. This would require a design and construction of a mechanical set-up during the onboard testing stage in the wind tunnel. The wind tunnel will serve as the wind generator to provide frontal wind to the

flapping wing MAV as illustrated in Figure 2.23. More sophisticated wind conditions with various directions and time-variant amplitudes would require the future work with a more advanced and reliable wind generator for drone testing.

When an incoming flow reaches the MAV's wing, the MAV's speed relative to the air flow is perturbed, resulting in an variation of angle of attack (AOA) along with changes in pitch, roll and yaw angles depending on the impact direction of the incoming wind. Thompson et al. [89] point out that the pitch angle variation plays the most significant role for MAV's attitude and stability control. This motivates a focus on verifying the air flow sensor's sensing ability under changes of pitch angle in future experiments of this thesis project and the design of test rigs that support such testing needs.

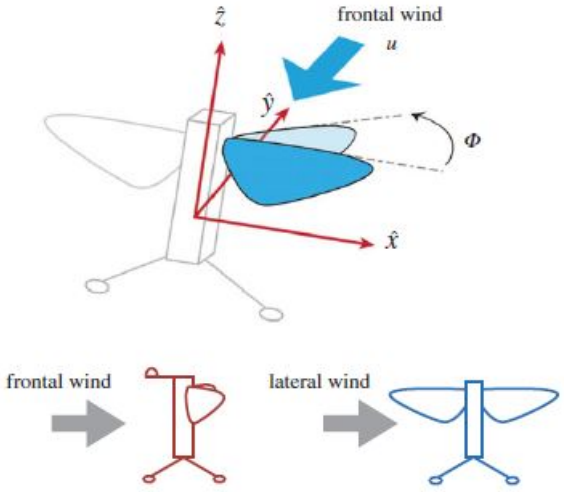

Figure 2.23: Example of incoming wind direction definition.

2.7. Literature review summary

2.7.1. Conclusions

This literature review started with the introduction and motivation behind airflow sensing in nature and its inspiration to the design of 3 major types of sensors capable of airflow sensing for airspeed measurement applications. To choose an airflow sensor capable of airflow sensing especially at a low-speed range ($0.5 \sim 4\ m/s$) that can be used on a flapping wing drone, the availability of the sensor for research use and the practical considerations in terms of size, weight and power (SWaP) restraints have to be considered. In the end, the Modern Device airflow sensors RevC and RevP are chosen as candidates for the thesis project.

As there is very limited reference and calibration data provided by the manufacturer, to be able to use the sensor reliably and understand its data quality, a large amount of the experimental work of the thesis will go into using reliable reference flow sources to calibrate the sensor and design test rigs with experiments that can further characterise the sensor's performance. These steps are crucial as at low flow speed ranges, the effective external flow could be at the same magnitude of measurement noise and drift. Besides, the inevitable flapping induced mechanical vibrations create an artificial flow speed caused by relative movements of the air flow sensor and make the distinction of actual ambient flow speed more challenging.

To be able to gather data that can be used to calibrate and characterise the airflow sensor's performance, the main workflow of the measurement and data acquisition can be summarized using Figure 2.24, mainly in the step of data acquisition and data processing. The further use of the data during the data distribution stage will be out of the current scope of the thesis project and can be considered for future projects to incorporate the airflow sensing into a disturbance rejection and stabilisation scheme. A brief proposal of directly relevant applications using the air flow sensor will be explained briefly in the following subsection.

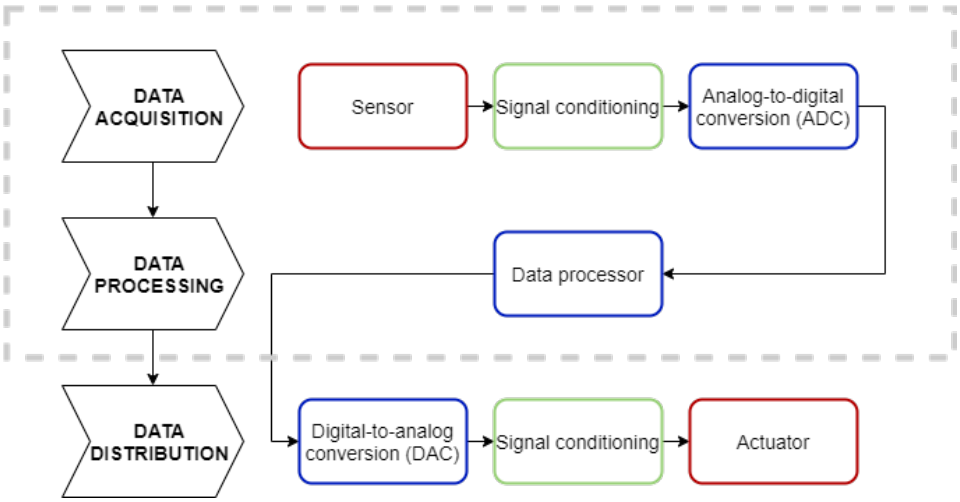

Figure 2.24: General block diagram of an electronic measurement and control system, reproduced from Wolffenbuttel [98]. Area encapsulated in dotted line will be the focus of the thesis project .

To conclude, the literature review helps narrow down the selection of a usable airflow sensor and the key steps to evaluate its performance and usability on a flapping wing MAV. It helps define the following steps in proceeding the thesis, and hopefully to further narrow down the engineering knowledge gap on equipping a flapping wing MAV with onboard airflow sensing.

- Propose the use of a thermal type micro air flow sensor detecting the ambient air flow velocity ahead of the leading edge of the wing

- Implement the flow sensor onto the FWMAV and quantify the characteristics of the sensor through its calibration complexity(zero wind, repetition, accuracy), measurement sensitivity and robustness
- Evaluate the vibration energy level of the sensor during fixed flapping tests and compare with that during the hovering flights.
- Evaluate if the sensor can measure airspeeds effectively during a hovering flight

Challenges remain in the field of miniaturized sensors capable of air flow sensing at low-speed ranges. No mature solution that mimics bio-inspired novel airflow sensing mechanism has existed yet that is easy to reproduce and can be well integrated onto a flapping wing MAV in free flight for disturbance sensing and rejection. In addition, when it comes to air flow sensor's performance and possibility to integrate, with the improvement of one performance parameter, it often comes at the cost of other parameters. Thus, at the proof of concept stage, certain compromises will have to be made to stay focused on maintaining sensing quality and usability in flight.

2.7.2. Potential future applications

Once the air flow sensor's performance is characterized, its use in airspeed measurement could bring more applications to flapping wing MAVs, mainly including wind speed estimation improvements and control scheme implementations in response to flow disturbance.

There have been a lot of research on the meteorology of wind-estimation using research aircrafts ([39]). But fewer practical methods have been applied to light-weight MAVs, which are more susceptible to wind velocity changes. The wind velocity is the vector difference between the avian vehicle speed relative to earth (also known as inertial velocity) and its speed relative to the airflow (also known as true airspeed) [92] as expressed in Equation 2.12. The Modern Device sensors can be used to improve the airspeed measurements potentially and with proper model construction to improve the actual wind speed estimation

$$\vec{v}_{\text{wind}} = \vec{v}_{\text{ground}} - \vec{v}_{\text{airspeed}} \tag{2.12}$$

Besides wind speed estimation, response to flow disturbance in control applications is another big ongoing research topic. This has deep roots in inspiration from biology as well. For example, birds can utilize their mechanoreceptor sensory information to effectively detect gusts [54] and react in a timely manner with their active preflex mechanism [16]. This kind of avian sensing motivates the development of more advanced sensory system for disturbance response, where air flow sensing plays a crucial role.

Two types of disturbance mitigation systems can be used to ensure that the MAVs can maintain a stable flight in various conditions: phase-advanced and reactive(i.e. inertia based) [54]. Phase-advanced flow sensing aims to measure incoming flow changes ahead of the vehicle's response to such flow disturbances and can be used in control schemes such as nonlinear dynamic inversion for disturbance rejection control [80]. Inertia-based techniques measure the vehicle's response to the variations of flow over the MAVs through rate changes in linear and angular accelerations, which limits the time of window for the MAV to adjust accordingly to minimize the influence caused by disturbance. Mohamed et al. [55] examined the fixed-wing MAV disturbance rejection performance of the phase-advanced sensory system compared to a conventional inertial-only control system and concluded that phase-advanced system shows significant performance improvement.

Such a sensing-reacting fused network has not yet reached a similar technology readiness level in artificially-made MAVs for outdoor flights compared to animal flight, especially lacking for flapping wing MAVs as the outdoor wind impact force can easily surpass the maximally produced lift of the state-of-the-art flapping wing MAVs. Traditional treatments of wind disturbance rejection schemes applied to fixed-wing or rotary-wing flight also can not be directly applied to flapping wing applications due to the unsteady aerodynamics nature [4]. Autonomous flight in gusty conditions

and improved flight efficiency have remained a challenge in MAV development, especially for small and agile MAVs such as flapping wing MAVs.

One of the most recent experimental efforts to improve flapping wing MAV's flight performance from Chirarattananon et al. [4] uses only the flapping wing MAV's position and orientation feedback provided by an external motion capture system as shown in Figure 2.25. They have verified that with partial knowledge of wind speed and direction, the disturbance rejection schemes are capable of estimating and compensating for the wind disturbances, which leads to a faster stabilization of the MAV and the reduction of the root-mean-square position errors by more than 50% under 0.8 m/s horizontal wind disturbance. Despite being able to prevent the flapping wing MAV from crashing and significantly reducing the position estimation error under wind disturbed flight, such a system requires the external assistance of the motion capturing cameras for state inputs and will not be suitable for applications in an unknown environment. A fully integrated onboard solution for disturbance rejection on a flapping wing MAV does not exist yet and remains challenging due to the size, weight, and power restrictions. In the future, the flight with the air flow sensor onboard Delfly Nimble in front of a mobile wind generator could be realized in a setup similar to what is shown in Figure 2.25.

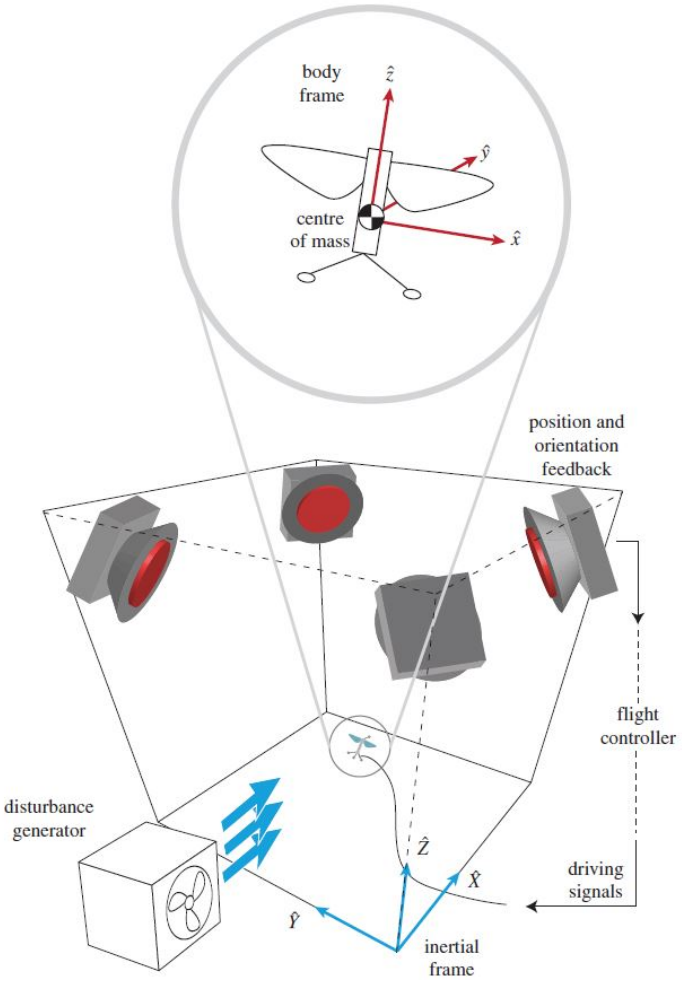

Figure 2.25: Indoor flight arena experimental set-up for improving flapping wing MAV's flight performance in the presence of gusts [4] Motion capture camera system provides MAV position and orientation feedback. The inertial and body-fixed frames are specified.

It is worth mentioning other non-airflow based sensory methods for disturbance sensing, primarily force-based methods which could be combined with airflow sensing methods in the future. By applying compliant strain gauges to self-sense the dynamic deformation due to flapping wings' shape changes associated with lift and thrust generation, Wissman et al. [97] point out it is important to develop feedback systems on flapping wings through distributed sensing. The wing level information along with knowledge of incoming wind will enable better control of the FWMAV, which is more susceptible to wind change during flight compared to quadcopter-type MAVs. However, strain gauges often would require more system-level customized design and integration when implementing on the FWMAV compared to air flow sensing methods.

To conclude, if the proof of concept of effective air flow sensing can be realized in this thesis project, then it opens up the possibilities to increase the flapping wing MAV's flight performance through more advanced sensing and control schemes when facing wind disturbances, which is one of the biggest challenges for flapping wing MAV development.

3

Experimental procedure

3.1. Summary of wind tunnel test campaigns

Wind tunnel campaigns are needed to calibrate and evaluate the two airflow sensors' performance. The low-speed wind tunnel W-tunnel in the TU Delft Aerodynamics Building has the ideal test environments to perform these campaigns. In this chapter, the experimental procedures of the two wind tunnel test campaigns performed in the W-tunnel are described in Section 3.2 and Section 3.3.

Table 3.1 further shows more details of the planned tests at different test locations, with different test objects, reference tools, and the actual test goals. According to the manufacturer Modern Device, the sensor model Rev P has better measurement accuracy and less directional sensitivity, in the 15% range. This shall be further confirmed through the first wind tunnel test campaign. And assume the new version of the airflow sensor Rev P has better performance characteristics, it will be used for the following Delfly onboard tests.

Test location	Test object	Reference tools	Test contents
W-tunnel campaign 1	RevC, RevP	Hot-wire probe, Pitot tube	Calibrate the sensor at different flow speeds. Perform rotational tests to evaluate directional sensitivity.
W-tunnel campaign 1	RevC, RevP	Hot-wire probe, Pitot tube	Evaluate turbulence intensity, at freestream speed ranging from 0 – 10 [m/s].
W-tunnel campaign 2	Rev.P, Delfly	Pitot tube	Perform mounted flapping tests with an airflow sensor onboard, at different flow and flight conditions, and vary RC throttle level and body pitch angles of Delfly.
Cyberzoo	RevP, Delfly	OptiTrack	Perform tethered hover tests with an airflow sensor onboard.

Table 3.1: Major groups of tests for the wind tunnel campaign 1 and 2.

3.2. Wind tunnel campaign 1: sensor characterisation

The goal of the wind tunnel campaign 1 is to identify a feasible calibration procedure for both airflow sensors and characterise their performance under different flow conditions by comparison with a hot-wire probe.

RevC and RevP sensor calibration will be performed both in the W-tunnel and in an air velocity calibrator, with the calibrator featuring more measurements at low flow speeds $U < 5m/s$. As a performance comparison, the same calibration procedure is done with a hot-wire probe to allow further flow measurements in the W-tunnel. In the laminar flow regime, RevC and RevP's directional sensibility will be investigated through rotational tests under different ambient flow speeds. The rotational tests will be repeated 3 times for 3 sets of RevC and RevP sensors to check for product difference out of manufacturing. In the turbulent flow regime, an add-on grid with porosity

56.25 % is placed 20 cm upstream of the investigated sensor and hot-wire. The turbulence intensity and frequency response from the acquired measurements will be compared to evaluate the air flow sensors' performance under the influence of turbulence.

3.2.1. Measurement set-up in W-tunnel

A. Wind tunnel speed control

The wind tunnel campaign location W-tunnel is shown in Figure 3.1. It has an open test section with two exchangeable contraction sizes depending on the experiment need. For the wind tunnel campaign 1 where the airflow sensors' performance are characterised, the 40×40 cm^2 contraction is used along with a $40 \times 40 \times 40$ cm^3 sized test box connected to the contraction. For the wind tunnel campaign 2 where the mounted Delfly tests with the airflow sensor onboard will be performed. The contraction with cross-sectional dimensions of 60×60 cm^2 and a contraction ratio of 3.62 ([50]) will be used. Such a configuration was built specifically for a set of Delfly related experiments in 2012 ([63]), where the measurements were performed for freestream velocities in the range of 2-6 m/s, which overlaps with the desired low range of test flow speeds for this thesis project .

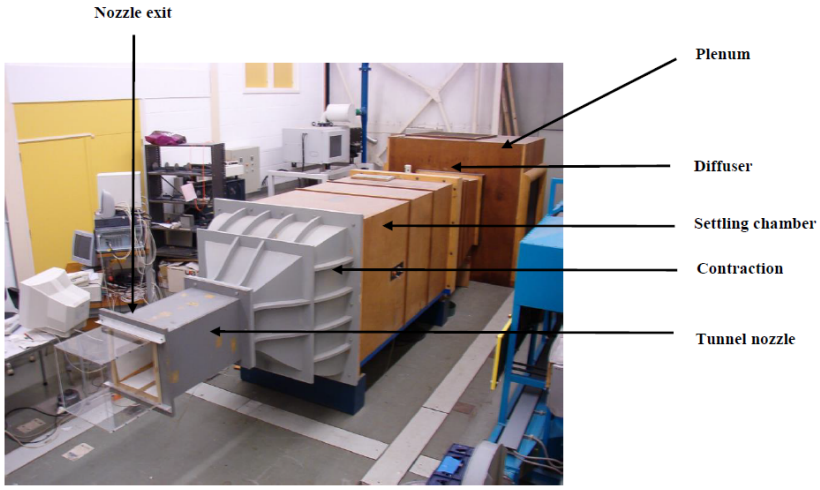

Figure 3.1: TU Delft wind tunnel facility W-tunnel section diagram [5].

The wind tunnel's freestream speed is regulated by setting the fan RPM on the tunnel computer. The corresponded freestream speeds with respect to different RPMs for both contraction used in two wind tunnel campaigns are displayed in Figure 3.2. Different contraction ratios lead to the difference in resulted freestream flow speeds when the fan RPM is set the same. As wind tunnel campaign 2 was performed later than campaign 1 throughout the thesis, small operational adjustment was made to increase the resolution at the very low speed range as can be seen in Figure 3.2b. This extra consideration was taken due to the increased difficulty to generate low speed flow reliably and the need for accuracy at the low speed range.

B. Test set-up

The airflow sensor calibration and performance characterisation is done in a $40 \times 40 \times 40$ cm^3 sized test box connected to the wind tunnel contraction nozzle exit as illustrated in Figure 3.3. The cross-sectional dimensions of the test box is more than 10 times larger than the tested airflow sensor, thus the tunnel wall boundary layer effects are negligible. The use of the test box is also to minimize any external disturbance from moving sources in the surrounding environment.

A support rod is placed in between the center points of the test box's lateral faces and is capable of controlled rotation if needed. There are two rotation mechanisms implemented in the test

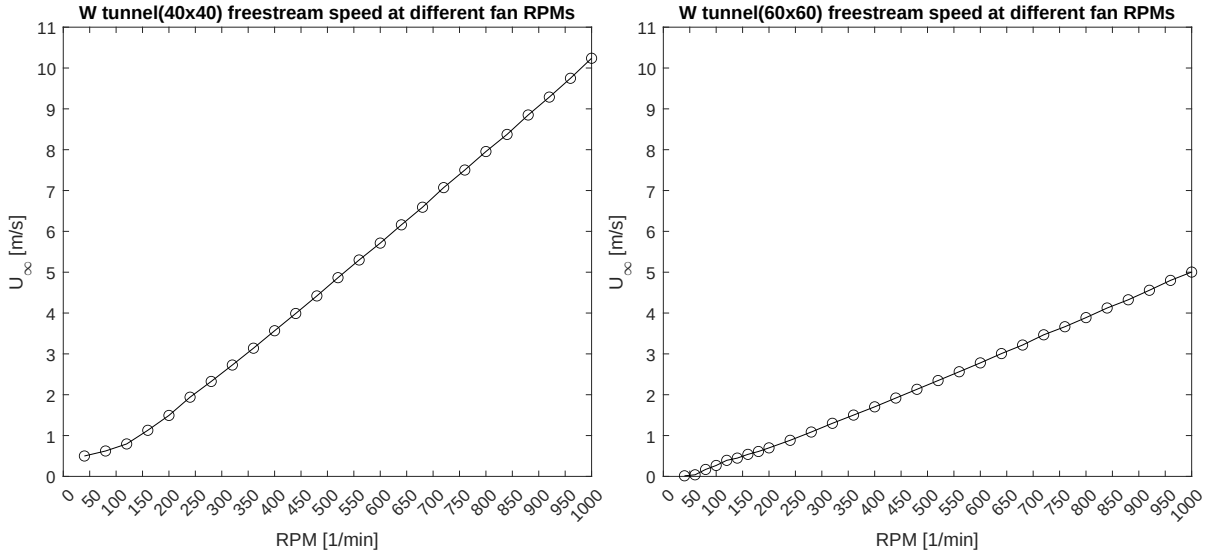

(a) Freestream in $40 \times 40 cm^2$ contraction

(b) Freestream in $60 \times 60 cm^2$ contraction

Figure 3.2: W-tunnel fan RPM setting corresponding to different freestream velocities.

box, of which their locations are indicated as the green and blue arrow in Figure 3.3. A close view of the rotation mechanism inside the test box is shown in details in the same figure. A 3D-printed sensor support holds the airflow sensor tightly while being connected to another 3D printed small disk that attaches onto the shaft of the stepper motor. This whole set-up is fixed onto the support rod through the motor casing with a self-designed clamping mechanism. The other rotation mechanism is installed with the help of a custom-made metal support structure on the outer face of the test box to enable the rotation of the whole support rod. The whole structure is stable even under larger freestream speeds $U_\infty > 10\ m/s$, providing a reliable platform to calibrate and characterise the airflow sensors' performance.

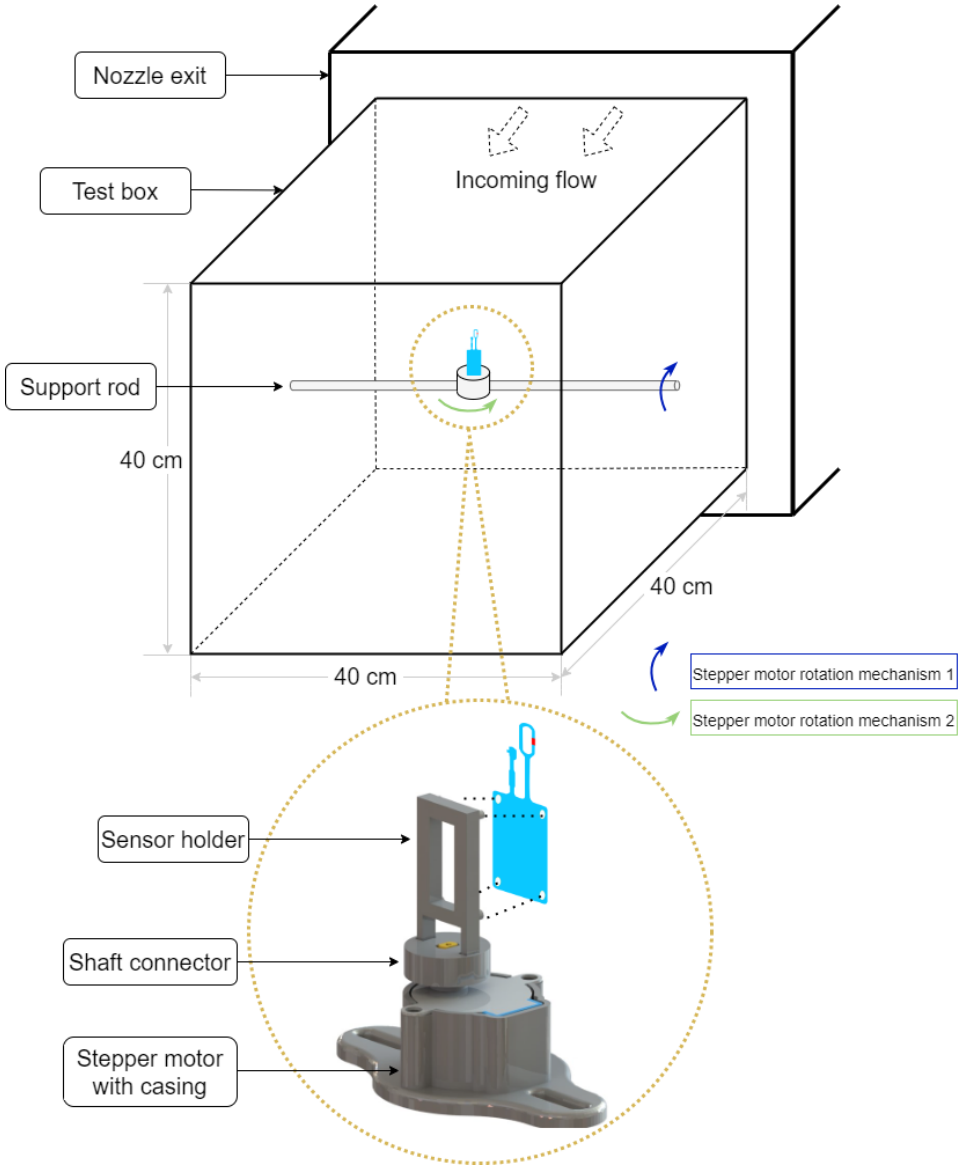

Figure 3.3: Illustration of the airflow sensor placement in the W-tunnel test box, with the rotation mechanisms that rotate the airflow sensor in different planes. The original motor mount casing is from open source community `https://www.thingiverse.com/thing:3923529`.

An example of the test set-up is shown in Figure 3.4. A laboratory power supply bench is used to power up the airflow sensors. Rev C is supplied with 5V DC and the model Rev P with 12V DC. Data acquisition of the airflow sensor's analog voltage readings is done with the National Instrument Data Acquisition (DAQ) chassis NI9215 (with 4 channels ±10V simultaneous 16-bit analog-to-digital converter) and then post processed in MATLAB. In order to investigate the airflow sensor's directional sensitivity, measurements need to be performed when the airflow sensor's sensing element faces the incoming freestream at a different angle. This is done through the two rotational mechanisms as illustrated in Figure 3.3, with a 5V DC step motor (Model 28BYJ-48) programmed and controlled through Arduino with motor drivers. The stepper motor rotates the airflow sensor for 360 degrees at a step size of 5 degrees. Data is sampled at 5 KHz for 5 seconds at each step to allow enough settling time before the sensor is in motion again.

The planes of rotation XY, YZ and XZ are defined in Figure 3.5, with the sensing thermistor of the airflow sensor as the point of origin. The front side of the sensing component has the most

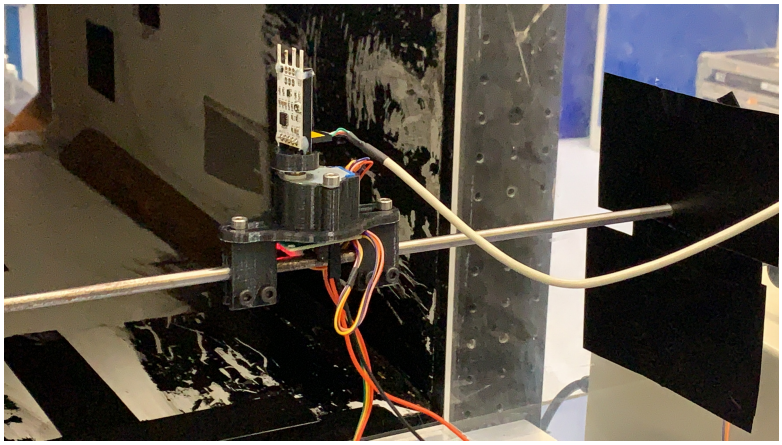

Figure 3.4: Test set-up for rotations in different planes to investigate Rev sensors' directional sensibility. The test set-up shown here enables the RevC sensor to rotate in XZ plane defined in Figure 3.5.

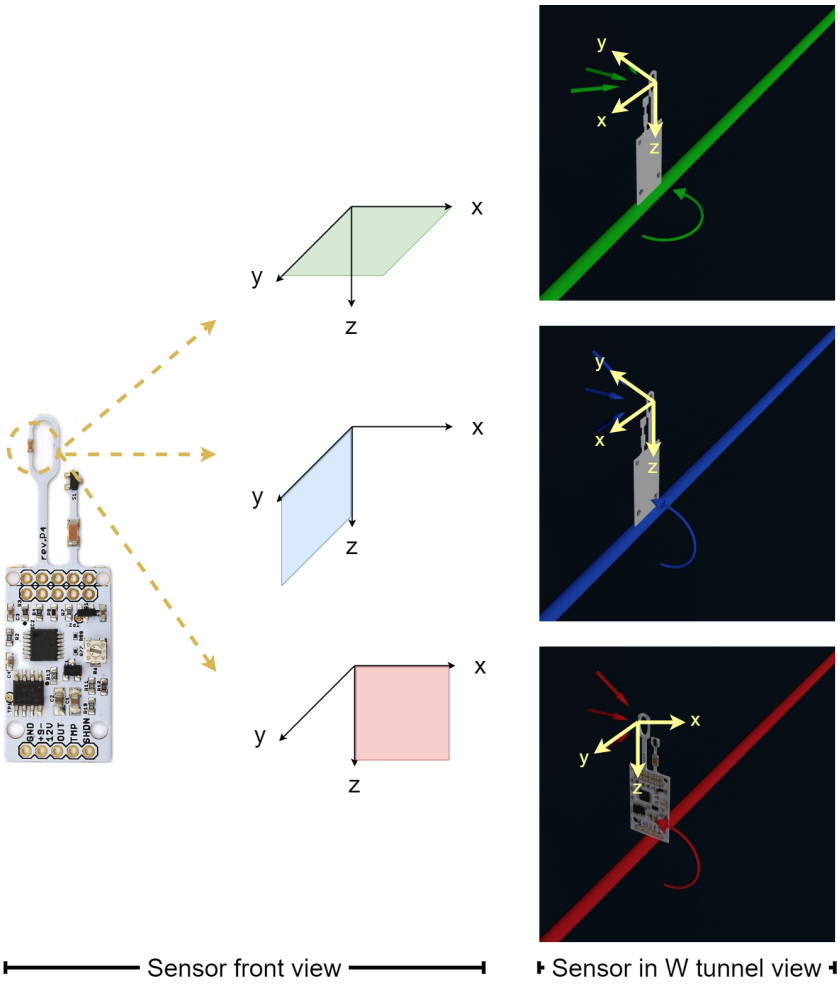

Figure 3.5: Illustration of the planes of rotation to investigate the airflow sensor's directional sensitivity with RevP sensor as an example.

optimal performance when it is facing the incoming flow directly. Thus for sensor calibration and performance characterisation, the airflow sensor's PCB side with electronics always faces the incoming flow directly. For rotational tests to determine the sensors' directional sensitivity, to realize

the different planes of rotation with respect to the direction of incoming freestream in the wind tunnel, the initial placement orientation of the airflow sensor for the XZ plane is 90 degree counterclockwise of the ones in the XY, YZ plane. This is directly illustrated in Figure 3.5 with the airflow sensor placed on the support rod at different initial orientations before the rotations start.

The final key component in the test set-up is the hot-wire system, which is needed for measurement performance comparison with the two airflow sensors. When the hot-wire probe is used, the airflow sensor is no longer placed at the center of the support rod. The two measurement tools are placed 5 cm apart from each other as shown in Figure 3.7a, with 2.5 cm from the center at each side. This distance is a balance such that the hot-wire probe and the airflow sensor measures the flow stream in the center of the wind tunnel as much as possible while avoiding the instrument bodies' wake-wake interaction in case of close proximity. The hot wire and the sensing element of the airflow sensor are being kept at the same height and parallel with the tunnel exit plane to ensure the simultaneous contact of the incoming flow when they reach both sensing instruments.

The hot-wire probe needs to interface with a DANTEC mini-CTA bridge and then connects to the National Instrument Data Acquisition (DAQ) chassis NI9234 for data collection. The LABVIEW software provides a visual programming environment that enables the data acquisition of the voltage output from the constant temperature anemometer (CTA) bridge and save the flow measurement results. More details regarding the hot-wire bridge operation are explained in subsection 3.2.2

C. The add-on turbulence grid

According to the internal W-tunnel operation manual from the Aerospace Engineering faculty server, the minimum achievable turbulence intensity level of the W-tunnel flow is at the order of 0.5 %. With the goal to characterise the airflow sensor's performance under more turbulent flow conditions, the freestream's turbulence level has to be increased. This is achieved by placing a grid the size of the test box cross-sectional area 20 cm upstream of the test target, right at the cross sectional space between the tunnel nozzle exit and the test box indicated in Figure 3.5.

Property	Variable	Value
Grid line thickness	d	5 [mm]
Grid line gap	g	15 [mm]
Porosity	$[1 - {}^{d}/_{(d+g)}]^2$	56.25 %

Table 3.2: Turbulence grid geometrical specifications.

The grid's geometric design parameters are listed in Table 3.2 and illustrated in Figure 3.6. Four of these pieces together form the complete grid that is placed in the test box to increase the freestream turbulence level. Each piece of the full grid is 3D printed with common printer filament material polylactic acid (PLA) and bonded together with cyanoacrylate glue. A deburring tool is used to make sure all the edges are smooth with no surface residuals. The actual grid in action can be seen in Figure 3.7b. The porosity of the grid is configured to be 56.25 % for practical reasons, since the W-tunnel already has a pre-manufactured metal grid with the same porosity but used on the larger test section 60×60 cm^2. For future experiments that need to increase freestream turbulence level, this set of grids can be reused for comparability.

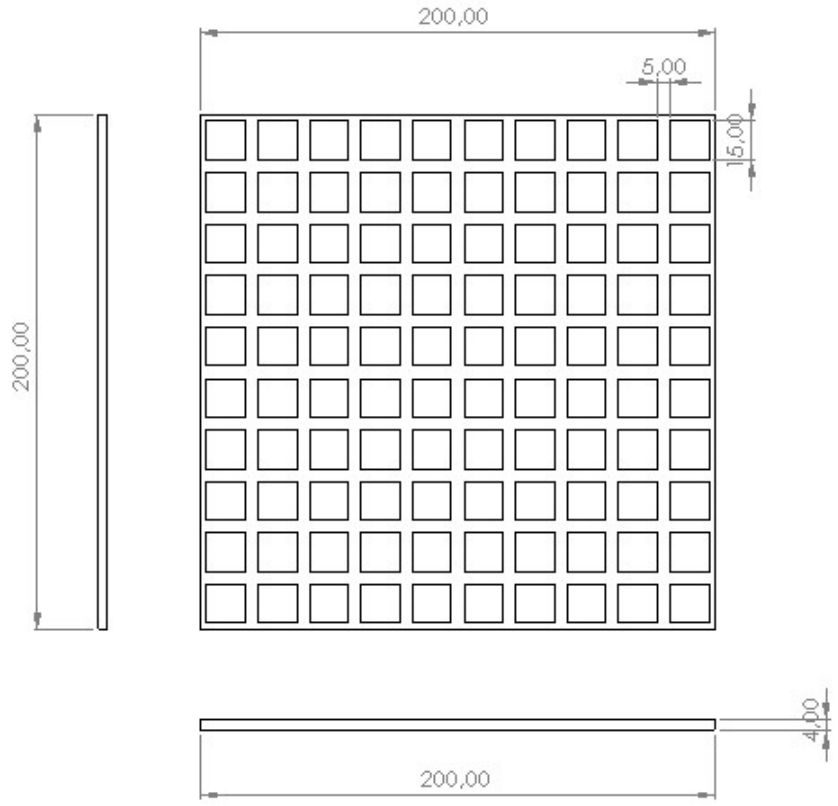

Figure 3.6: One of the four components that forms the full turbulence grid, all dimensions are specified in mm.

The test set-up with and without the add-on grid can be seen in Figure 3.7. The grid is used to increase the freestream turbulence level, which provides the extra turbulent flow condition to compare the hot-wire probe and the airflow sensors' performance. As a first impression of their measurement difference in turbulent flow, only one grid porosity and grid upstream placement location is used here, given the limited test time and the focus of the thesis being a complete overview study of the airflow sensors instead of just one feature. To be able to examine the airflow sensor's performance under various turbulence intensities and the corresponding dynamic frequency responses when changing the freestream speeds, a more advanced set-up for regulated turbulence generation such as with a closed-loop control set-up developed by Quinn et al.[67] could be adopted depending on the experiment needs.

Note that the instantaneous velocity field of the turbulent flow fluctuates rapidly in all three spatial dimensions [25], but here due to the limitations of instrumentation, the measured velocity is one-dimensional, with the component along the freestream being the dominant contribution.

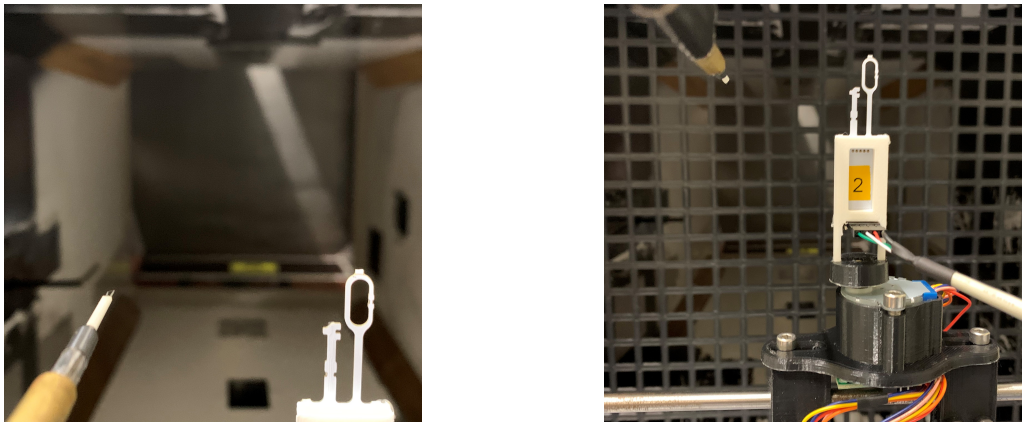

(a) Without add-on turbulence grid

(b) With add-on turbulence grid 20cm upstream of the sensors

Figure 3.7: A RevP sensor placed near the hot-wire probe facing incoming freestream in the W-tunnel.

3.2.2. Hot-wire system

To be able to evaluate the measurement performance of the Modern Device airflow sensors, a conventional hot-wire anemometer is the best and easily accessible laboratory instrument that are suitable for velocity measurements, flow turbulence investigations and a more accurate determination of high frequency flow fluctuations. Other tools such as a turbulent flow instrumentation (TFI) Cobra probe [65] is also suitable and even provides more directional information but also significantly more expensive.

For the choice of the hot-wire system, the wind tunnel facility at the TU Delft Aerodynamics building has a state-of-the-art constant temperature anemometer (CTA) TSI IFA-300. It has the complete hardware set-up with all the components needed for a common CTA measuring chain shown in Figure 3.8. There is also custom-made software in LABVIEW provided by the aerodynamics research group that works with the TSI ThermalPro program, which provides detailed steps to get the resistance values (operate resistance, cable resistance, hot-wire probe resistance), calculate the offset and amplifier gain values (as illustrated in Figure 3.9) to prepare the hot-wire system for more accurate measurements with less signal saturation.

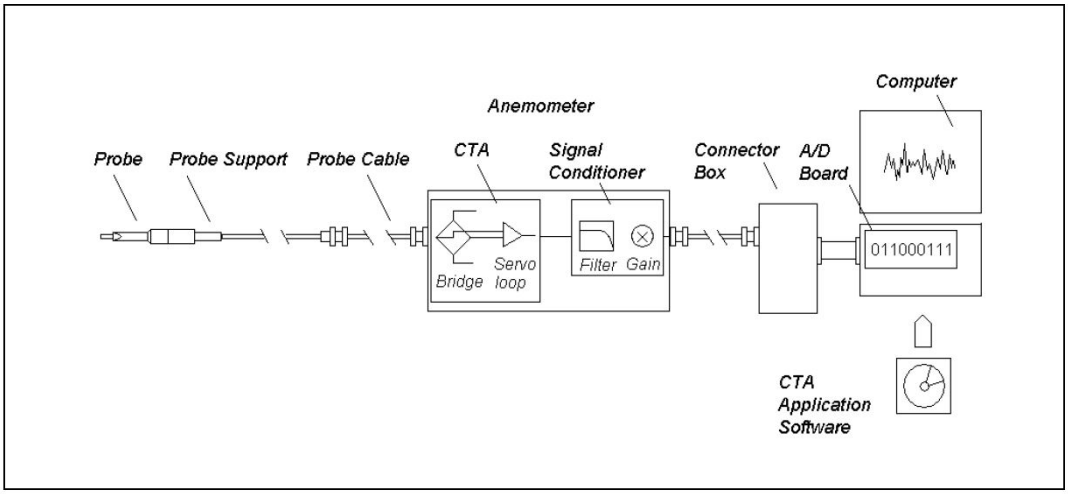

Figure 3.8: Typical constant temperature anemometer (CTA) measuring chain [35].

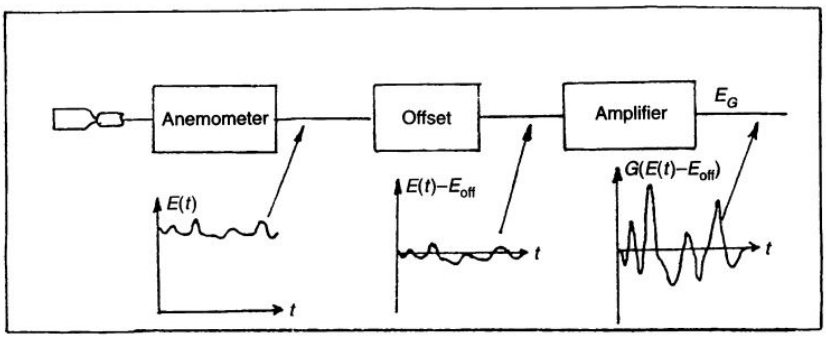

Figure 3.9: The principle of a signal-conditioning unit applied in hot-wire anemometry[11].

This IFA-300 system would be the ideal system to use for the hot-wire related experiments. The wind tunnel test slots are booked during the time this system is available, which is fortunate since it was sent for repair abroad not long ago. However, during the first wind tunnel test slot, it was discovered the bridge in the IFA-300 was not functioning properly, thus it has to be sent for inspection and repair again. Given the logistics during the COVID-19 pandemic, this would lead to at least a 3-5 month delay for the thesis. In order to still be able to carry out the test plan as much as possible, an alternative has to be sought quickly, especially considering booking a test slot in the wind tunnel facility also takes waiting time. Fortunately, the author was able to borrow a smaller CTA system (Model: MiniCTA manufactured by DANTEC) from a university start-up company Dimple Technology. A three-day short window was open in their agenda, which was rather lucky considering they have full tests running all year around. This unexpected solution avoided wasting the pre-booked test slots. However, since the CTA system was stripped off from a totally different testing environment, there was no time to build a well-considered software solution like the one for the IFA-300. Thus, the MiniCTA will just provide the raw analog voltage signals to the National Instrument DAQ NI 9234 that was available at the moment.

A single channel anemometer MiniCTA as shown in Figure 3.10 is used with a 5 μm tungsten hot-wire probe. As both time averaged results and spectra information are needed during the calibration process and performance assessment, a high sampling rate with a large number of samples are used during all data acquisition. A sampling rate 5 kHz is used which is sufficient for spectral analysis frequencies up to 2.5 kHz according to the Nyquist criterion.

Figure 3.10: Constant temperature anemometry device MiniCTA from Dantec Dynamics. Picture source: `https://www.dantecdynamics.com/solutions-applications/solutions/fluid-mechanics/constant-temperature-anemometry-cta/minicta/`.

3.2.3. Measurement set-up with the air velocity calibrator

The air velocity calibrator model 1127 from the company TSI is used to provide controllable flow speeds at the lower range, as shown in Figure 3.11.The device is connected to a pressurized air supply. Air travels through a settling chamber and exits through a nozzle. The amount of air exiting through the nozzle onto the calibrated target is controlled by manually rotating two knobs that are placed on the calibrator. One knob is coarse and the other one is for fine adjustments to set closer to the desired output flow speed. The calibrator comes with 3 nozzle sets for low velocity applications as shown in Figure 3.12. The nozzle set can be installed onto the calibrator depending on the application need. For velocity range between 0.1 to 5 m/s, Nozzle set #3 is used throughout the experiments. An externally connected Mensor DPG 2100 pressure transducer measures the differential pressure dP between the settling chamber and the ambient environment to obtain velocities of flow emerging through the exit nozzle. A type-T thermocouple is installed onto the air velocity calibrator to provide more accurate temperature readings in the flow settling chamber. The pressure readings, temperature feedback, along with a pre-calibrated relationship from TSI are fed into a LABVIEW program that records the reference flow speed and output voltage signal from the calibrated target.

(a) Components of Model 1127 Air velocity calibrator [91]

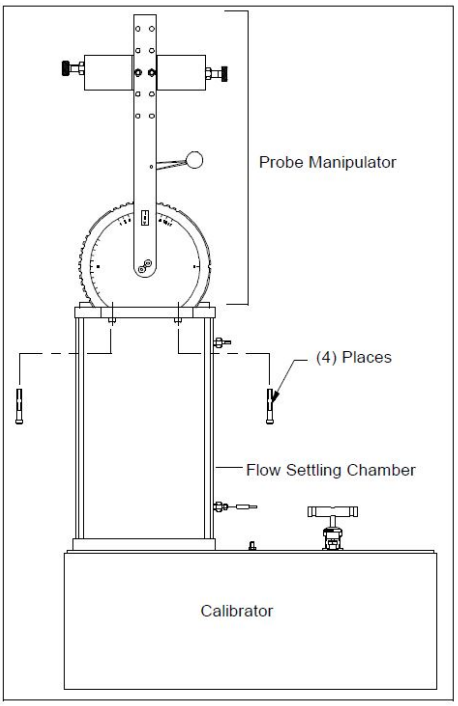

(b) The main calibrator of Model 1127

Figure 3.11: The air velocity calibrator used for calibration at low flow speeds below 5 m/s.

According to the user manual from the manufacturer TSI [91], when nozzle set #2 or #3 is used, differential pressure across the secondary nozzle is measured since the pressure change in the settling chamber is too low to measure with accuracy under low flow speed ranges. By relating this differential pressure to the control velocity V through the secondary nozzle with isentropic relations shown in Equation 3.1 to Equation 3.4, the true exhaust speed exiting to the calibrated target can be calculated with a given polynomial relation from TSI by using the control velocity V, as expressed in Equation 3.5.

$$a_0 = \sqrt{\gamma R(T + 273.15)} \tag{3.1}$$

$$M = \left[2 \frac{\left(\frac{P+\Delta p}{P}\right)^{\frac{\gamma-1}{\gamma}} - 1}{\gamma - 1} \right]^{\frac{1}{2}} \tag{3.2}$$

$$a = \left(\frac{a_o^2}{1 + \left(\frac{\gamma-1}{2} M^2\right)} \right)^{\frac{1}{2}} \tag{3.3}$$

$$V = M \cdot a \tag{3.4}$$

$$U_{\text{calibrated}} = \mathrm{k} + \mathrm{aV} + \mathrm{bV}^2 + \mathrm{cV}^3 + \mathrm{dV}^4 + \mathrm{eV}^5 + \mathrm{fV}^6 + \mathrm{gV}^7 + \mathrm{hV}^8 + \mathrm{iV}^9 \tag{3.5}$$

$$\begin{aligned} \mathrm{k} &= -1.3657 \times 10^{-2}, \mathrm{e} = 2.0689 \times 10^{-8} \\ \mathrm{a} &= 5.7953 \times 10^{-2}, \mathrm{f} = -1.7582 \times 10^{-10} \\ \mathrm{b} &= -1.7365 \times 10^{-3}, \ \mathrm{g} = 8.9361 \times 10^{-13} \\ \mathrm{c} &= 6.7386 \times 10^{-5}, \ \mathrm{h} = -2.4661 \times 10^{-15} \\ \mathrm{d} &= -1.5064 \times 10^{-6}, \mathrm{i} = 2.8118 \times 10^{-18} \end{aligned}$$

Nozzle Set #1				
Exit Nozzle	**Secondary Nozzle**	**Calibrator Model**	**Velocity Range (m/s)**	**dP Range (mmHg)**
10 mm Dia.	#1	1128A 1127, 1128B, 1128C	3 to 50 3 to 150 10 to 215	.04 to 10 .04 to 100 0.4 to 260
Nozzle Set #2				
10 mm Dia.	#2	1128A 1127, 1128B, 1128C	1 to 16 1 to 49 3 to 100	.04 to 10 .04 to 100 0.4 to 700
Nozzle Set #3				
14 mm Dia.	#3	1128A 1127, 1128B, 1128C	0.1 to 1.6 0.1 to 5 0.3 to 10	.04 to 10 .04 to 100 0.4 to 700
High Velocity Nozzle Set				
6 mm Dia.	#1	1128C	10 to 340	0.4 to 700

Figure 3.12: Different velocity ranges of nozzle sets available for the air velocity calibrator. Nozzle set #3 used in this test campaign is highlighted in the red rectangle.

Figure 3.13 shows the actual test scenes where the airflow sensor RevP's sensing components are directly placed above the air velocity calibrator nozzle exit. Figure 3.14 shows a clear view of how the hot-wire probe is placed at the center of the calibrator's exit stream. Note that a custom-made holding structure is used to hold the airflow sensor or the hot-wire probe tightly above the nozzle exit. Like in the wind tunnel tests, the hot-wire probe has to be handled with extra care since any direct contact of the wire with a surface will damage the wire and cause it to have to be sent for repair.

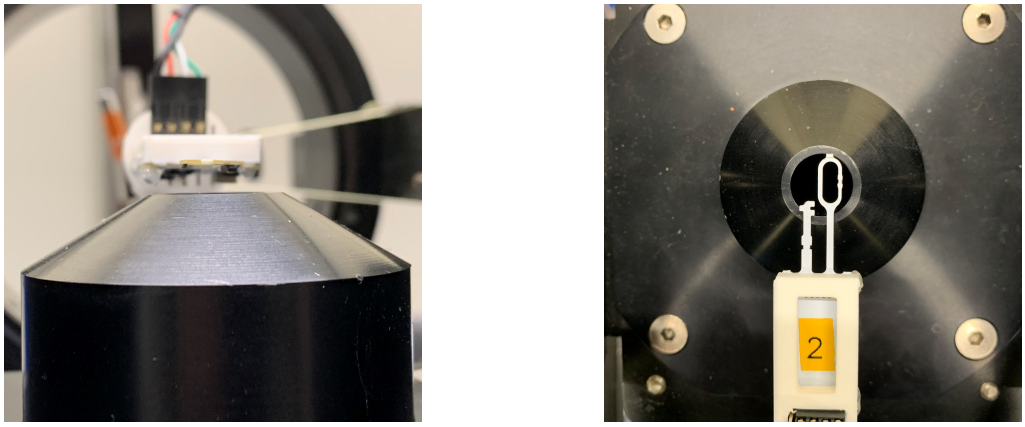

(a) Side view (b) Top view

Figure 3.13: A RevP sensor being calibrated with the air velocity calibrator.

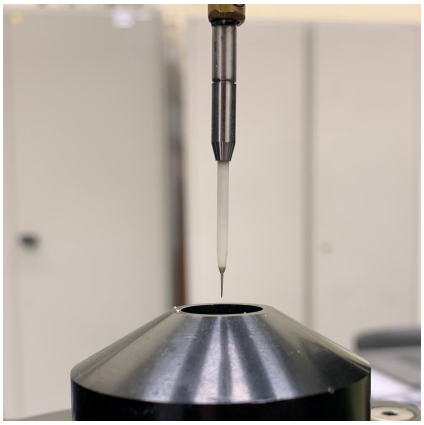

Figure 3.14: A hot-wire probe being calibrated with the air velocity calibrator.

3.3. Wind tunnel campaign 2: mounted Delfly test

3.3.1. Measurement set-up in W-tunnel

After wind tunnel campaign 1, the airflow sensor with the better performance will be selected to use during the wind tunnel campaign 2. The goal of the wind tunnel campaign 2 is to investigate if the airflow sensor is able to measure various ambient flow speeds effectively despite the vibrational influence from the flapping motion. Various factors such as Delfly body pitch angles, throttle levels and freestream speeds will be changed to test the airflow sensor's measurements.

A self-designed test rig mount with clamping mechanism to fix Delfly Nimble's position can be seen in Figure 3.15. As pitch angle is the most significant for MAV's attitude stability when encountering perturbation [89], the airflow sensor's performance under various pitch angles need to be investigated. The used test rig that clamps right beneath the Delfly autopilot module is capable of rotations that allows the placement of Delfly Nimble at a desired pitch angle. Once fixed at a certain angle, a level sensor is placed on the clamping arm to verify the body pitch angle.

The airflow sensor is placed on top of the Delfly Nimble fuselage (a square-shaped carbon rod) with a lightweight, small-sized 3D-printed structure binding it tightly to the fuselage. This placement location is chosen for two reasons. First, there is very limited space along the rest of the fuselage rod. Second, putting the airflow sensor ahead of the leading edge potentially makes the airflow sensing phase-advanced, meaning the incoming flow change can be sensed before the flow reaches the MAV. The flapping wing MAV wake influence or wing-wing interaction is also assumed to be

negligible at this location, which means the least influence to the airflow sensor's measurement.

(a) Side view

(b) Back view

Figure 3.15: Delfly being clamped onto a custom-made W-tunnel support structure for fixed flapping tests, placed at the exit of the $60 \times 60\ cm^2$ contraction section.

3.3.2. Flapping wing MAV preparation

Before the wind tunnel tests can proceed, the flapping wing MAV Delfly Nimble has to be flight-ready, which means in manual free flight situations, the FWMAV should be trimmed nicely such that it does not drift during a hovering flight, meaning no slight rolling, pitching or yawing movements. This indicates there is no structural deformation or deviation causing unwanted roll/pitch/yaw torques that otherwise will not be observed during the mounted tests in the wind tunnel since Delfly will be clamped, which could cause measurement inaccuracies that are rather difficult to identify and correct for. The following checklist is summarized based on experimental experiences after hundreds of hours of flying and debugging the FMWAV. The relevant mechatronic parts can be referred to in Figure 2.20.

- The gears in the gear box can rotate smoothly with no tension.
- All the metal pins that fix the gearbox components should be straight, which minimizes undesired structural tension or uneven flapping stroke plane.
- The metal pins that fixate the gears and arms on the flapping mechanism should not be inserted too tight. The pin cap should not protrude too high above the gear surface which could prevent a smooth rotation to enable flapping.
- The dihedral arms on the dihedral angle control mechanism should be approximately straight on a line when Delfly Nimble is hold vertically, i.e., the left and right wing-pairs should be approximately aligned in the same plane.
- Both wing-pairs should have similar tension at the wing root taping points above the yawing arm. The wing-pair root should be taped and hot glued tightly onto the carbon rod and not sliding up and down during flapping.
- The autopilot board should be aligned in parallel to the left of the body fuselage rod, at the center of gravity of the whole Delfly. If not bound tightly, crashes could tilt the autopilot and cause flight stability issues with the wrong initial angular information.
- To correct for further excessive amount of pitch and yaw, adjust the dihedral and yaw servo trim values in the airframe through trial and error with more hovering tests.

A few extra small but important experiment practices with the Delfly Nimble are briefly explained here.

First, since Delfly Nimble is fully hand-made, each Delfly Nimble will possess small mechanical and structural difference. Thus, only one Delfly Nimble is used throughout the wind tunnel tests. This ensures the comparability of data but also at the cost of more repair and maintenance effort of the MAV during the limited wind tunnel testing slot time. For example, the servos overheat quickly after operating continuously throughout a testing day. Small test breaks for the MAV to cool down is needed if large power drawing fluctuations are observed through the power supply current readings. Eventually, these low-cost servos have to be replaced due to malfunction. In general, as a realistic test planning with a flapping wing MAV, at least 50 % of the time should be allocated for repair and maintenance, and the resetting of the test-up in future experiment planning.

Second, a good clamping mechanism to hold the entire Delfly Nimble is important. This directly affects the amount of the body fuselage vibration. As Caetano et al. [13] point out from previous wind tunnel tests with Delfly Nimble's predecessor Delfly II that the clamping position affects the natural frequency of a flapping wing MAV given the cantilever system formed by the clamp rigidly attaching to the body structure, along with other less influential factors such as the mass and materials of the ornithopter. They conclude that the most suitable clamping position to hold the flapping wing MAV is near the mean aerodynamic and inertial force application point. On Delfly Nimble, this location is at the autopilot board. With all the electronics and wiring concentrated there causing practical difficulty, in the end, the only possible ideal clamp location is right beneath the autopilot board. For the future, should more wind tunnel tests need to be performed, a better global fixture system to mount Delfly at certain pitch or yaw angles more precisely would be desired.

3.3.3. Data acquisition

There are two sources for data acquisition in the wind tunnel campaign 2. The onboard Delfly Nimble information is directly logged to an SD card which is connected to the autopilot board. The previous used National Instrument NI 9214 DAQ chassis will continue the data sampling with the airflow sensor and logging is done on the computer through the LABVIEW program.

Data acquisition source	Obtained data	Symbol	Sampling frequency $[Hz]$
On-board Delfly	Linear accelerations	a_x, a_y, a_z	512
	Angular accelerations	a_p, a_q, a_r	512
	Throttle level	δ_T	100
	Body angles	ϕ, θ, ψ	500
NI 9214 DAQ chassis	RevP temperature analog voltage	E_{temp}	5000
	RevP airflow analog voltage	$E_{airflow}$	5000

Table 3.3: Wind tunnel campaign 2 data acquisition overview.

4

Results: Wind sensor characterisation

In this chapter, the key results of the airflow sensor calibration and performance characterisation are discussed. The airflow sensors RevP and RevC are calibrated using a static calibration method by calibrating the system at various mean velocities [11]. Two calibration references are used by utilising the flow generation in a wind tunnel and in a commercial air velocity calibrator. Two calibration fitting models are applied in Section 4.1 and Section 4.2. The measurement resolution improvement at low flow speeds are explored with the use of the air velocity calibrator. In terms of measurement performance, the airflow sensors' directional sensitivity in the three-dimensional space are investigated in Section 4.3. A constant temperature hot-wire anemometer is used to compare with the two airflow sensors' measurement performance in both laminar and turbulent flow described in Section 4.4 and Section 4.6. In the end, conclusions that lead to the selection of the RevP sensor as the ideal airflow sensor onboard a flapping wing MAV are drawn.

4.1. Calibration with King's Law

4.1.1. Calibration in air velocity calibrator

Both RevP and RevC airflow sensors are being calibrated in the air velocity calibrator for flow speeds between $0 \sim 5\ m/s$. The used of the air velocity calibrator is to provide more calibration resolution at the low flow speed regime. 26 calibration steps are taken including a zero velocity measurement at the beginning. Each calibration point is sampled for 5 seconds at 5 KHz and the results are time averaged. This data sampling applies to all the calibration tests throughout the test campaign. The curve fit that interpolates the voltage and speed results are based on the fourth order polynomial derived from King's Law.

RevP airflow sensor

Figure 4.1 shows the percentage error and the absolute error (defined in Equation 4.1 and Equation 4.2) between the measured results and curve-fit results for the RevP sensor. Overall, the King's Law fit method works better on the hot-wire results, with the curve slope less steep at the beginning of the calibration and a less than 1% overall percentage error excluding the first two calibration points at the extremely low flow speeds, where measurement from the pressure transducer is being pushed to its sensitivity limit. Given the steeper slope of the RevP curve at the lower 20 % of the calibration velocity range, a smaller calibration step could be taken in the future to further refine the calibration at extremely low flow speeds.

$$\text{Percentage error} = \frac{\text{Absolute error}}{\text{Reference flow speed}} \times 100 \tag{4.1}$$

$$\text{where} \quad \text{Absolute error} = abs(\text{Curve fit speed} - \text{Reference flow speed}) \tag{4.2}$$

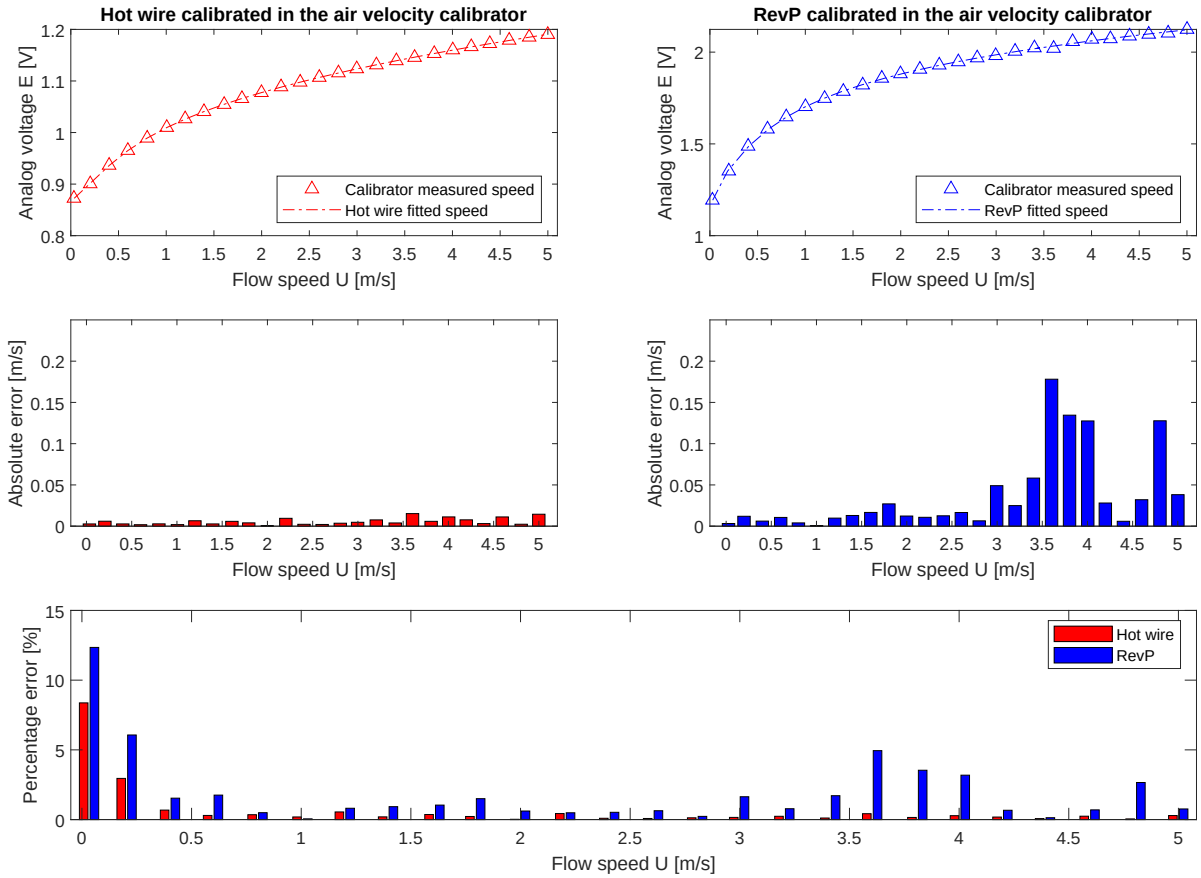

Figure 4.1: Hot-wire anemometer and RevP calibrated in the air velocity calibrator with King's Law.

RevC airflow sensor

Figure 4.2 shows the absolute error and percentage error between the measured results and curve-fit results for the RevC sensor. At flow speeds $U < 1m/s$, the calibration results for the RevC sensor have larger percentage error compared to RevP's results, while there is no significant difference for the rest of flow ranges.

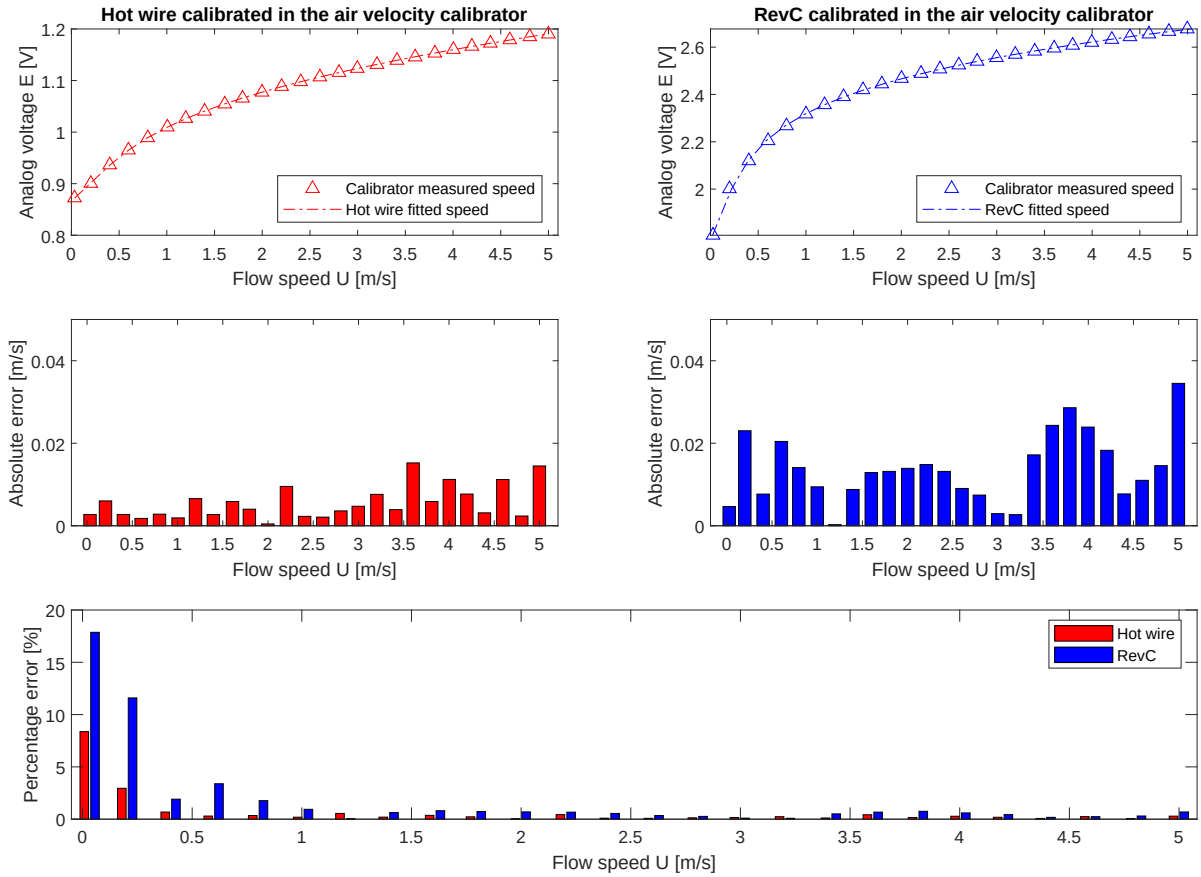

Figure 4.2: Hot-wire anemometer and RevC calibrated in the air velocity calibrator with King's Law.

4.1.2. Calibration in wind tunnel

Both RevP and RevC airflow sensors are being calibrated in the W-tunnel for flow speeds between 0.5 ~ 10 m/s. This range is wider than the potential wind disturbance range for Delfly Nimble (0 ~ 4 m/s) considering the airspeed range when Delfly is pitching forward at an optimal speed around 3 m/s. This also means that the calibration results can be used on other MAVs with an airspeed less than 10 m/s. For larger ranges, a re-calibration will need to be performed with larger reference flow speeds. In the current wind tunnel calibration, 25 calibration steps are taken. A strict zero measurement is not able to be achieved due to the ambient flow noise even when the wind tunnel is not operating.

RevP airflow sensor

Overall, for the RevP sensor, the percentage error is comparable to that of calibration in the air velocity calibrator in terms of order of magnitude. The higher the flow speed is, the lower the percentage error is(less than 0.5 %), which makes King's Law curve fit more suitable for large flow speed ranges. The steeper slope of the RevP curve can also be observed here in Figure 4.3, which shall be dealt with an increase in measurement resolution at the low flow speed ranges.

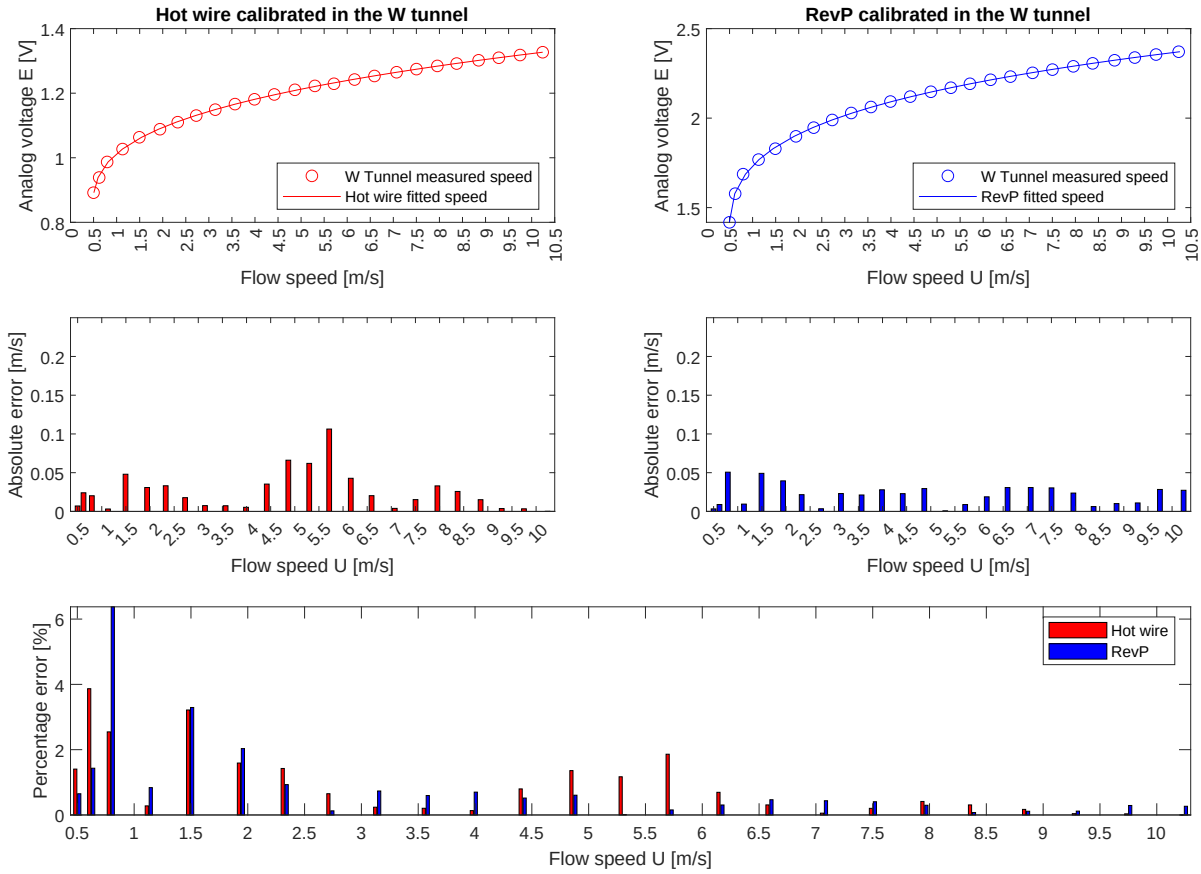

Figure 4.3: Hot-wire anemometer and RevP calibrated in the W-tunnel with King's Law.

RevC airflow sensor

In the wind tunnel,the RevC sensor has very close calibration results compared with RevP as can be seen in Figure 4.4. At flow speeds $U < 1\ m/s$, the calibration results for the RevC sensor have smaller percentage error compared to RevP's results, with a maximal difference at around 4 %. This information at the low speed range should be viewed with caution since the reference flow speed from the wind tunnel at low speeds are less reliable. It is also not directly measured at the flow region close to the airflow sensor, since the W-tunnel has its own flow speed determination system. While in the calibrator, a Mensor DPG 2100 pressure gauge is directly connected to the calibrator chamber for pressure readings. Note that for all the above calibrations, both RevP and RevC sensors have the same $O(10^{-2})$ order of magnitude in terms of absolute error, indicating a comparable measurement performance.

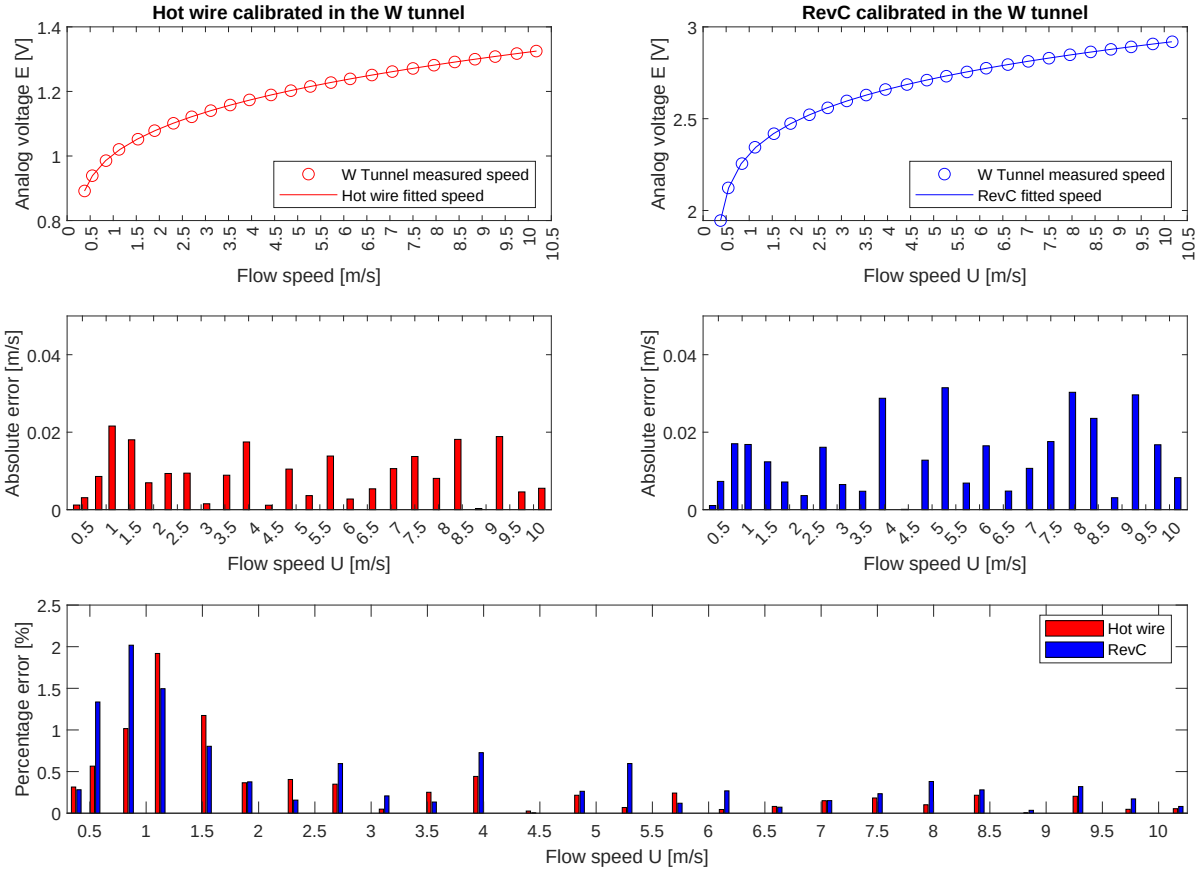

Figure 4.4: Hot-wire anemometer and RevC calibrated in the W-tunnel with King's Law.

4.1.3. Improved low speed resolution

RevP airflow sensor

The calibration results of RevP in both the air velocity calibrator and the W-tunnel is displayed together in the same Figure 4.5 in the hope of refining the measurement resolution at the lower end of the flow speed ranges. The two calibration curves intersect approximately at flow speed $U = 1\ m/s$, which is chosen as the refining point where below this value, calibration results from the calibrator is used and above this value, wind tunnel calibration results are used. The combined calibration results dataset form a new calibration curve shown in Figure 4.6 and the respective polynomial coefficients are summarized in Table 4.1. Note that in Figure 4.5, the calibrator results deviate slightly from W-tunnel calibration results as the flow speed increases. This could happen due to the placement of the calibrated target above the exit nozzle. Despite the sensor is centered right above the calibrator exit nozzle, it is impossible to reproduce the exact distance that is used by the manufacturer to acquire the calibration polynomial relationship. The true flow speed would be lower than the polynomial calibrated speed due to the loss of effective air pressure caused by the placement gap. Thus this leads to smaller analog voltage output from the calibrated target sensor considering less heating current is needed with less convective heat transfer from a smaller flow speed.

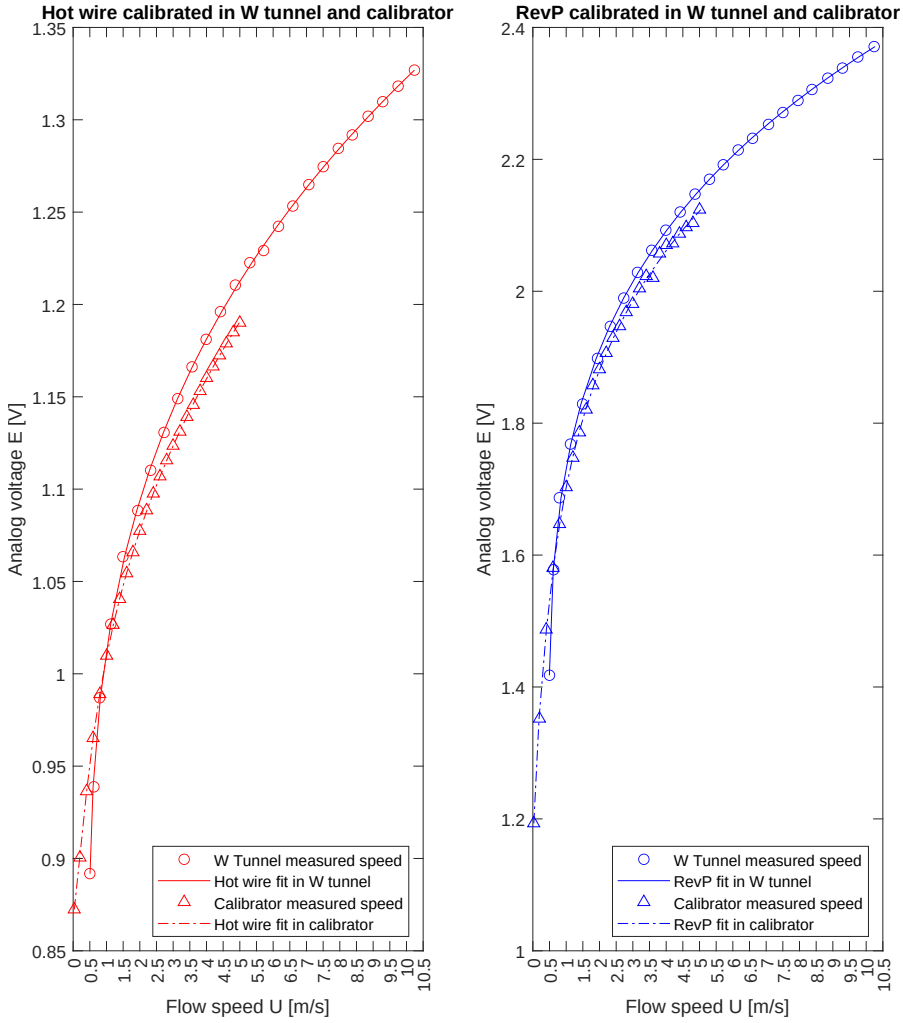

Figure 4.5: Comparison of hot-wire anemometer and RevP's calibration results with different calibration tools using King's Law.

	P_4	P_3	P_2	P_1	P_0
Calibrator	8.4080	-46.2862	97.5318	-91.6633	32.1309
W-tunnel	4.5646	-22.2505	42.5811	-38.4583	14.3975
Combined	4.7396	-22.1532	37.7390	-26.0497	5.3855

Table 4.1: RevP sensor King's Law calibration coefficients under different conditions.

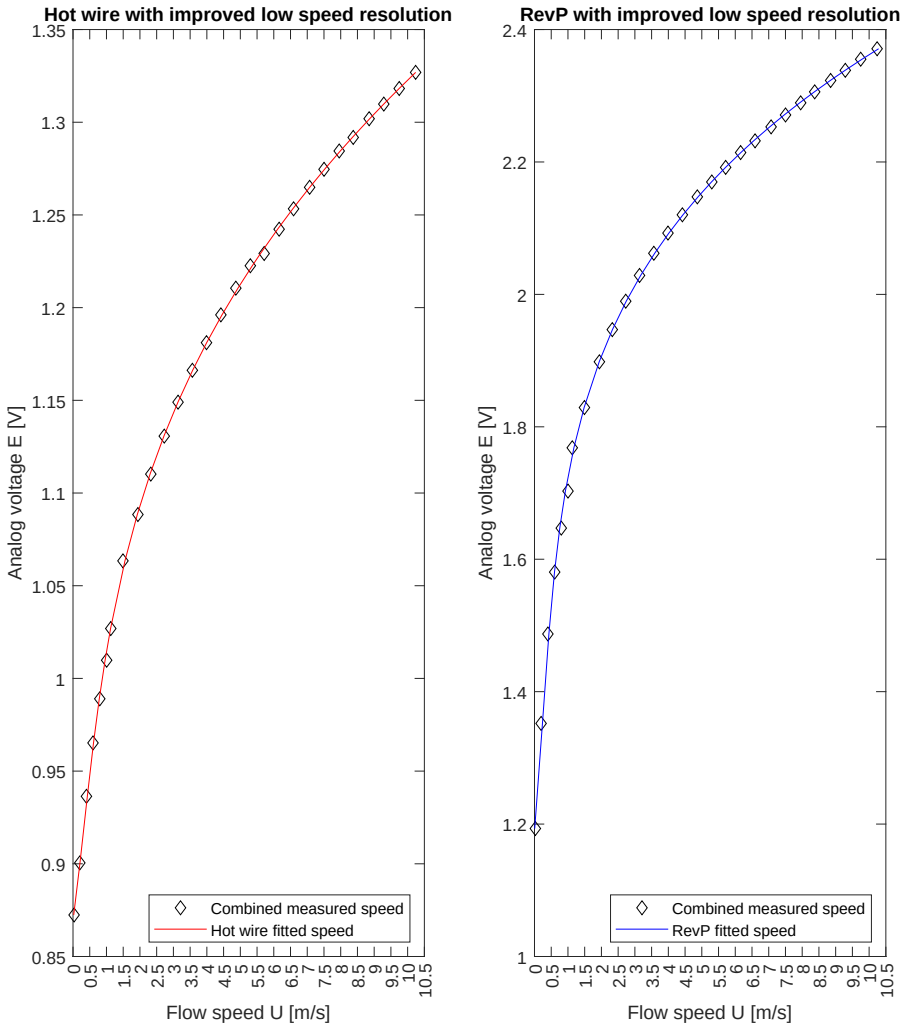

Figure 4.6: Combine hot-wire anemometer and RevP's calibration results by increasing the low speed resolution.

RevC airflow sensor

The same low speed resolution improvement procedure is also applied to the RevC airflow sensor. The calibration curve comparison of the two calibration references is shown in Figure 4.7. The respective polynomial coefficients are summarized in Table 4.2, with the improved calibration curve displayed in Figure 4.8.

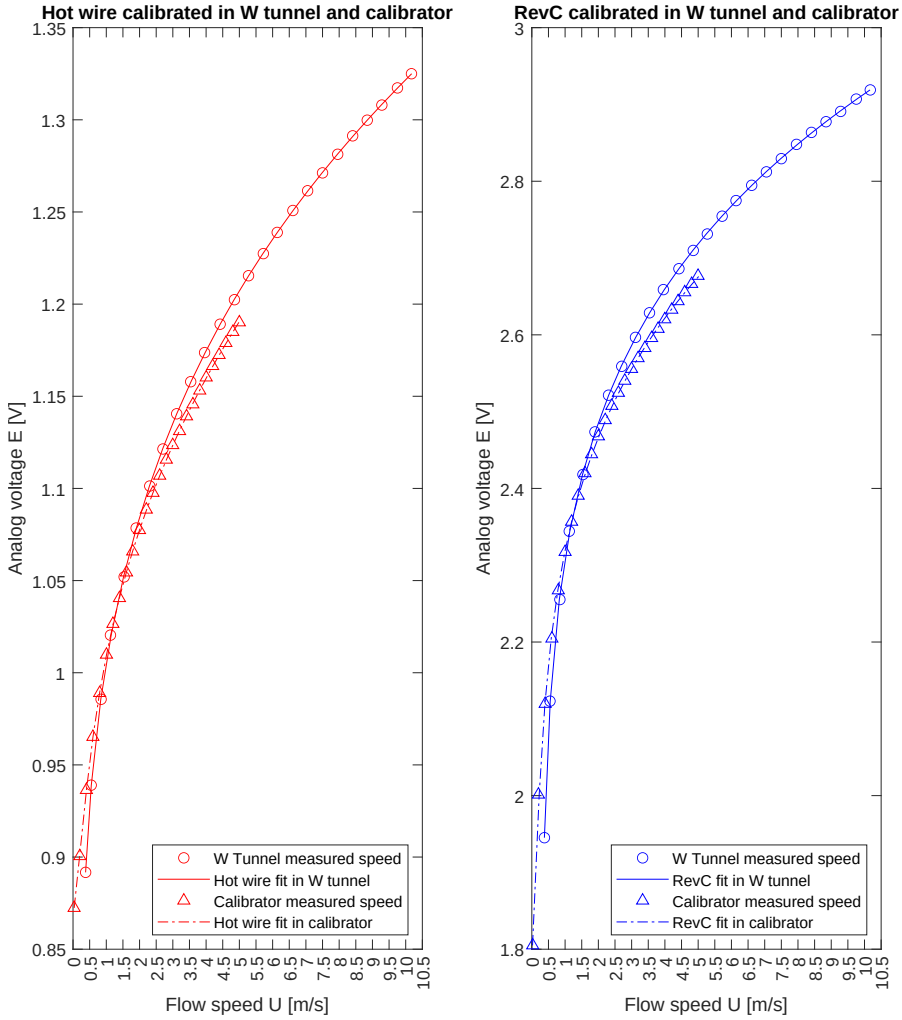

Figure 4.7: Comparison of hot-wire anemometer and RevC's calibration results with different calibration tools using King's Law.

	P_4	P_3	P_2	P_1	P_0
Calibrator	8.6632	-64.4621	180.3544	-223.9036	103.6955
W-tunnel	6.6905	-49.9006	140.4989	-176.4594	83.4985
Combined	8.3263	-65.5758	195.9443	-261.9220	131.6547

Table 4.2: RevC sensor King's Law calibration coefficients under different conditions.

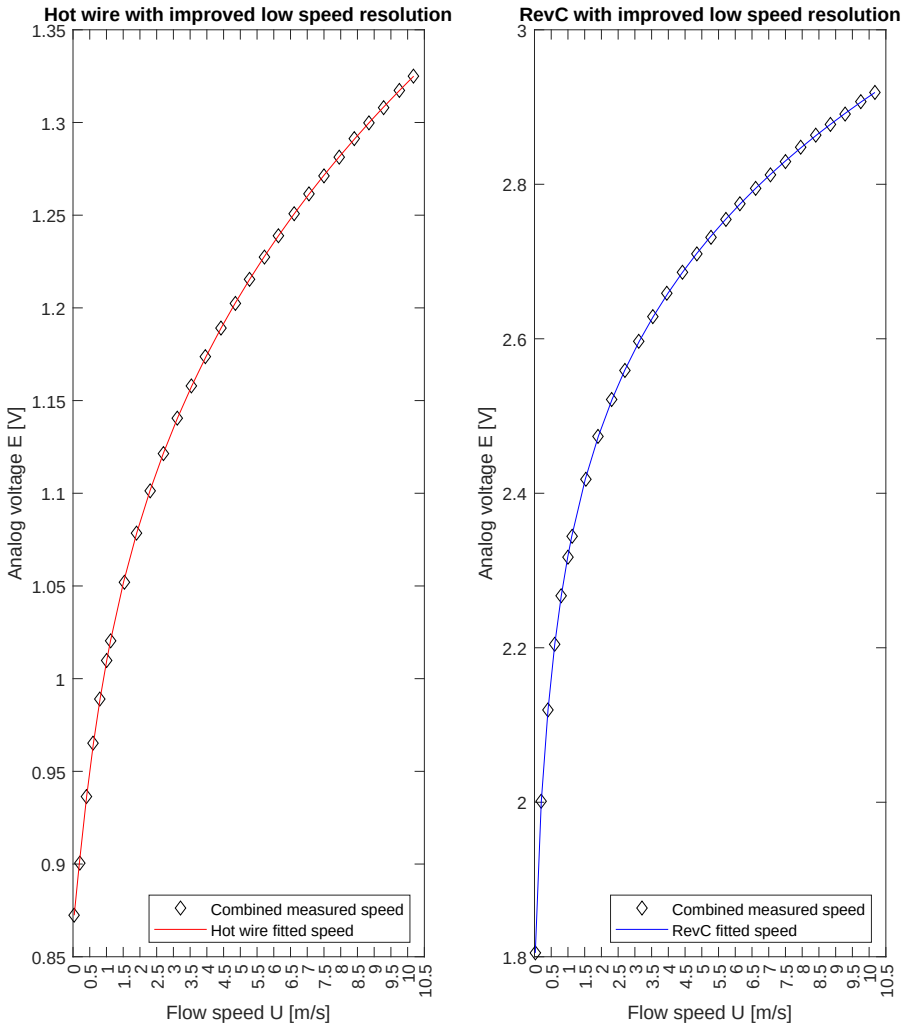

Figure 4.8: Combine hot-wire anemometer and RevC's calibration results by increasing the low speed resolution.

4.2. Calibration with custom fit function

The King's Law calibration method from the previous section does not utilize RevP airflow sensor's temperature analog measurements. However, the RevP airflow sensor could be used under different ambient temperatures given the change of testing locations and testing time throughout the year. Thus having a calibration model that uses the ambient temperature information could be useful in practice. This model is referred to as a custom fit for calibration. The same calibration results from the RevP calibration in the previous section are used here for comparability.

4.2.1. Calibration in air velocity calibrator (RevP)

Comparing the calibration results in the calibrator using two calibration models as shown in Figure 4.10, it can be seen that the custom fit model has a very close percentage error in terms of magnitude compared to the King's Law fit, with the King's Law model being more accurate at the higher flow speeds. In practice, this custom fit model can serve as a sanity check option if the testing environment temperature deviates significantly from the calibration environment temperature approximately 20 $^{\circ}C$. Note that in Figure 4.10, the percentage error of the first measurement point with the custom fit is approximately 240 %, a huge number due to the extremely low flow speed at the start of the measurement, thus it is treated as an outlier and removed in the percentage error plot to achieve better data visualisation for the rest of the percentage errors which are significantly

lower.

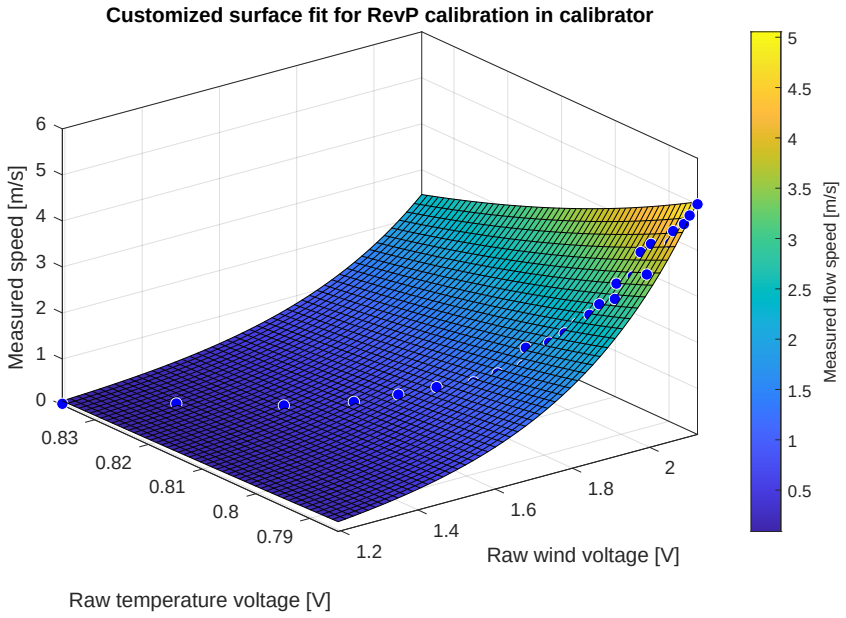

Figure 4.9: RevP calibrated in the air velocity calibrator with the custom fit function.

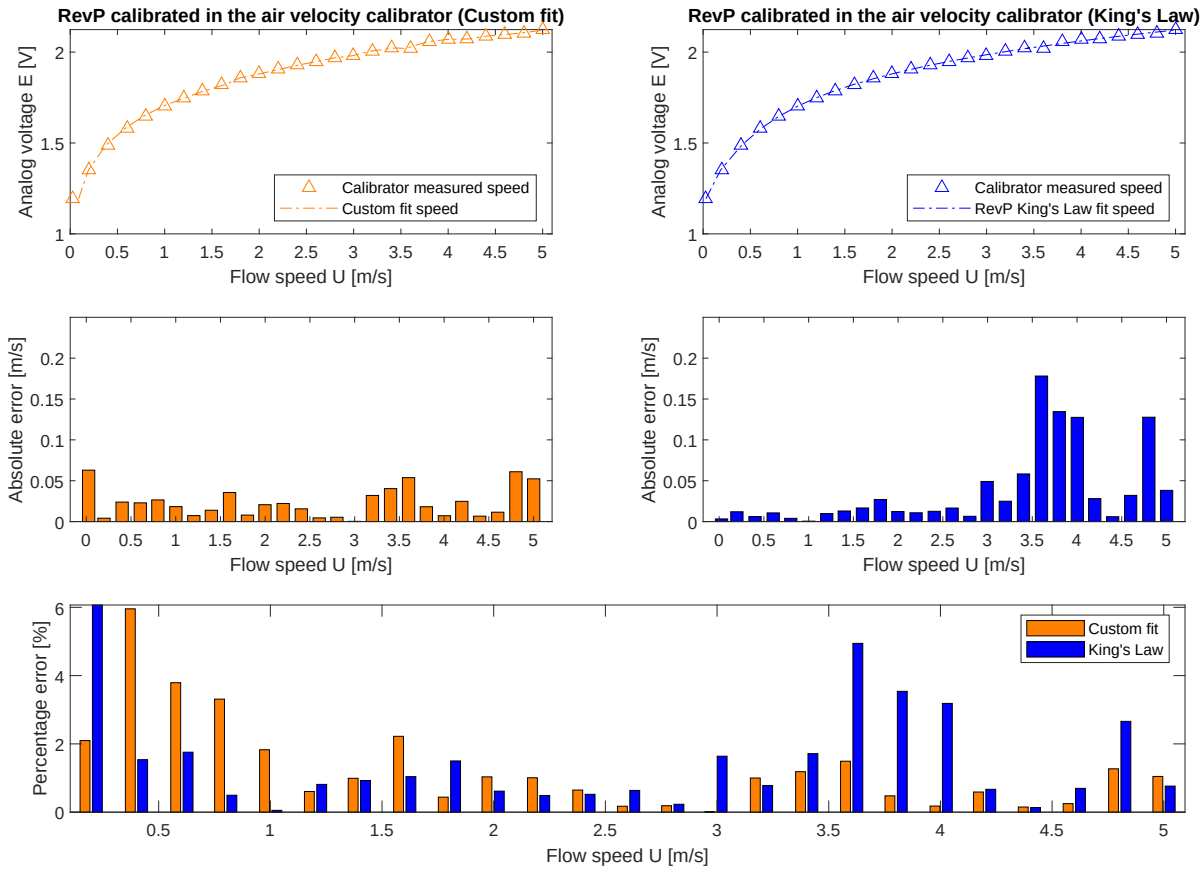

Figure 4.10: Hot-wire anemometer and RevP calibrated in the air velocity calibrator with the custom fit function.

4.2.2. Calibration in wind tunnel(RevP)

Figure 4.12 further confirms that the two calibration models perform very closely, especially at larger flow speeds $U > 5\ m/s$. The discrepancy mainly happens at the lower end of the speed range $U < 2\ m/s$, with the custom fit model producing a larger percentage error. Note that in Figure 4.12, the percentage error of the first measurement point with the custom fit is approximately 48%, a huge number due to the extremely low flow speed at the start of the measurement, thus it is treated as an outlier and removed in the percentage error plot for better data visualisation of the rest of the percentage errors which are significantly lower.

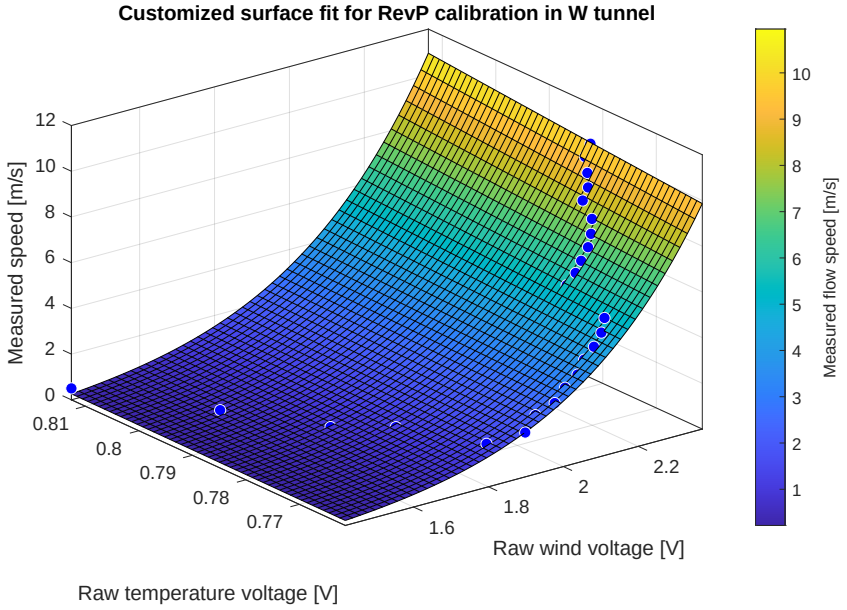

Figure 4.11: RevP calibrated in the W-tunnel with the custom fit function.

It can be observed from both Figure 4.9 and Figure 4.11 that despite having approximately 5 % fluctuations in temperature voltage output, which is reasonable given the onboard thermistor module for temperature measurement having $\pm 4°C$ fluctuations according to its datasheet [52], the temperature voltage output from the RevP airflow sensor displays large non-linearity. This raises question on how reliable the onboard hardware compensation for ambient temperature change is, which can only be known through a more detailed study of the circuitry of the sensor board.

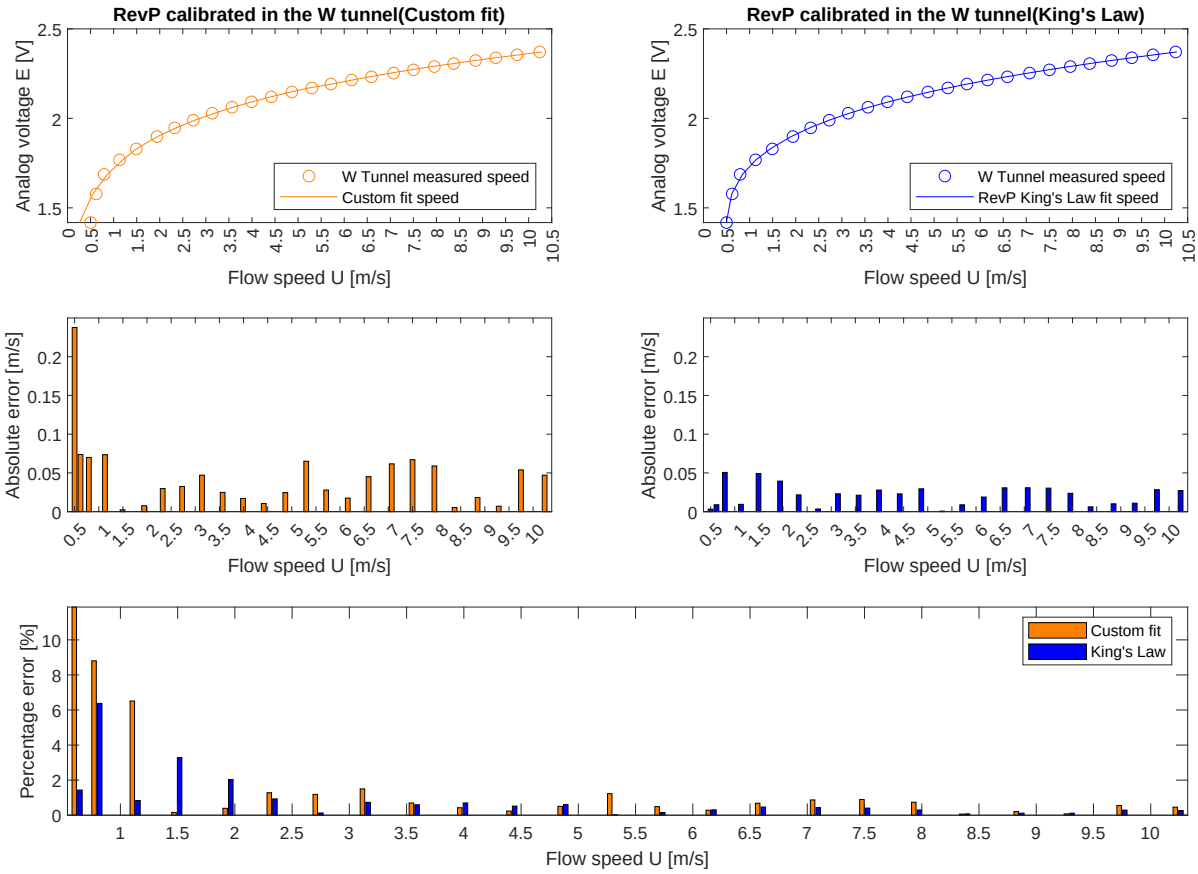

Figure 4.12: RevP calibrated in the W-tunnel with both King's Law and the custom fit function.

4.2.3. Improved low speed resolution (RevP)

The method to improve the low speed resolution as explained in Subsection 4.1.3 is also applied here to the custom fit calibration model as shown in Figure 4.13. Calibration coefficients based on the custom fit model from the W-tunnel and the calibrator tests are summarised in Table 4.3 for future use. Note that the coefficients are with 95 % confidence bounds based on the custom fit function option in MATLAB by using the custom fit model as the fitting function.

	a	b	c	d
Calibrator	-5.14	0.08588	5.073	0.05764
W-tunnel	0.4325	-0.01314	1.546	0.1506
Combined	0.8397	-0.01728	1.223	0.1823

Table 4.3: RevP sensor custom fit calibration coefficients under different conditions.

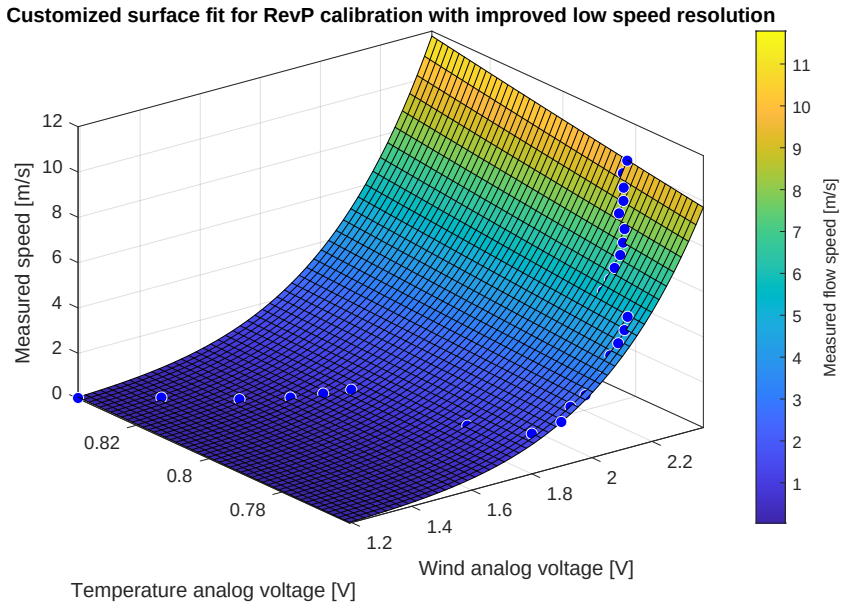

Figure 4.13: Combine RevP's custom fit calibration results by increasing the low speed resolution.

4.2.4. Combination of two calibration models

To compare King's Law and the custom fit calibration models, the calibration curves based on measurements from both the W-tunnel and the air velocity calibrator are shown in Figure 4.14. Figure 4.15 further shows the calibration results with improved low speed resolution based on results in Figure 4.14. It can be seen that with the same calibration datasets, both models have almost identical calibration curves and can be used to calibrate the airflow sensor, with the custom fit model utilising the extra temperature information.

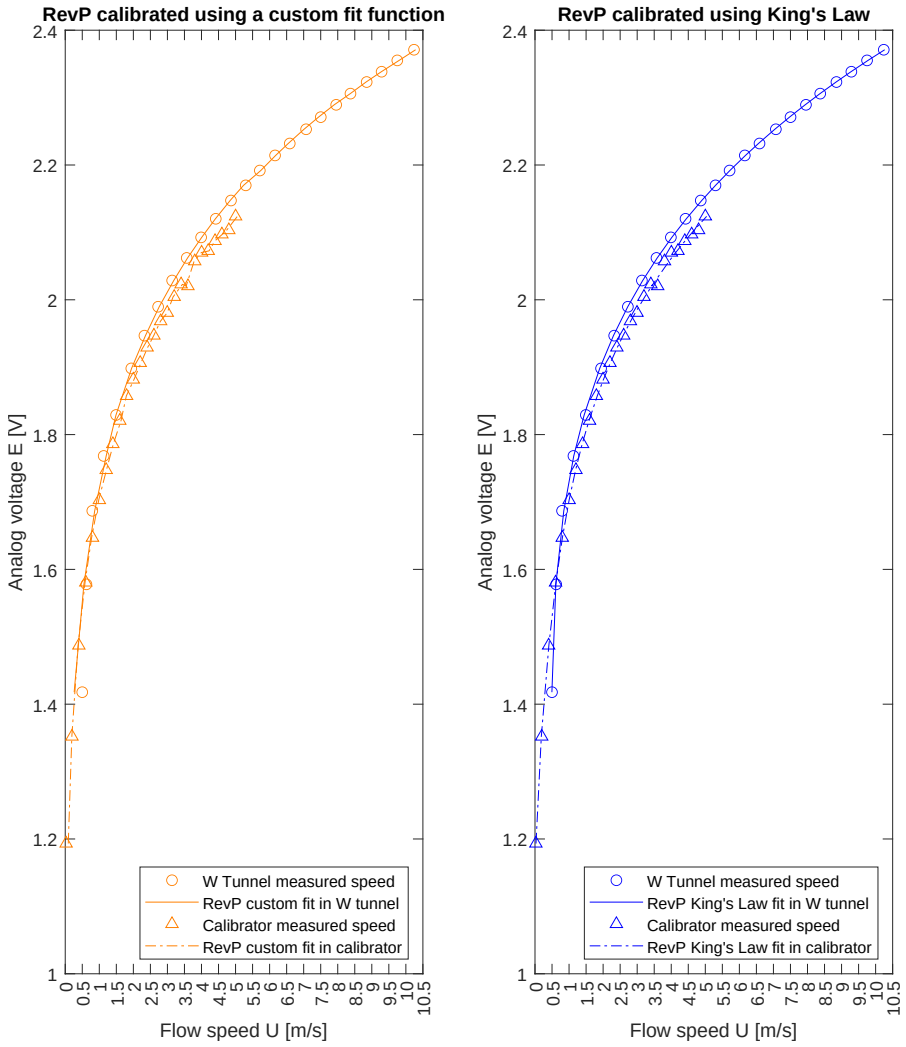

Figure 4.14: Comparison of two calibration models for RevP calibrated in the W-tunnel and the air velocity calibrator.

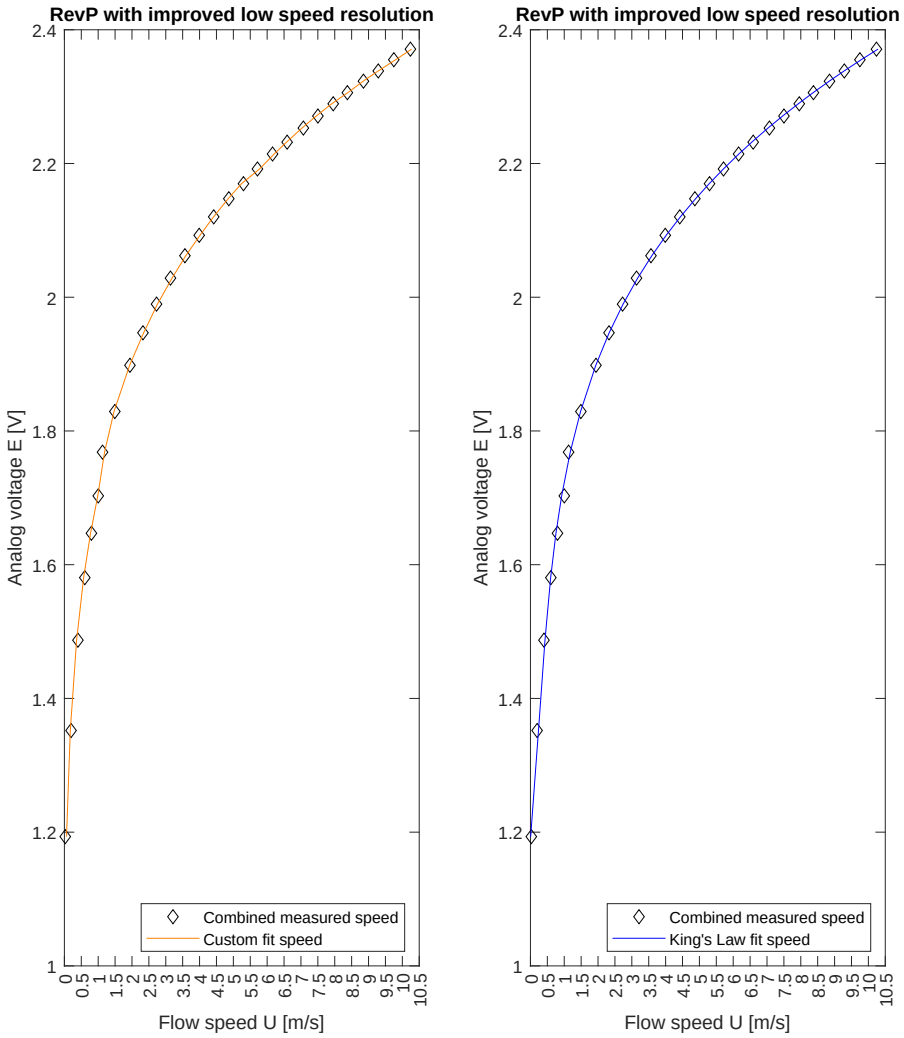

Figure 4.15: Increase the low speed resolution when using different calibration models for RevP calibrated in the W-tunnel and air velocity calibrator.

4.2.5. RevC calibration issue with temperature

Reference flow temperature used for RevC's temperature calibration is obtained by averaging the readings from the mixed temperature dataset and equals to 20.3953 $°C$. The non-linearity shown in Figure 4.16 results from the difficulty of accurate temperature measurements with such low-cost equipment. It is thus not possible to fit a clear relationship between the raw temperature outputs with a reliable reference source of ambient temperature. This means no calibration coefficients can be obtained for RevC's temperature outputs and thus this output can not be used in future applications, which leaves King's Law the only calibration model that can be applied to RevC at the moment.

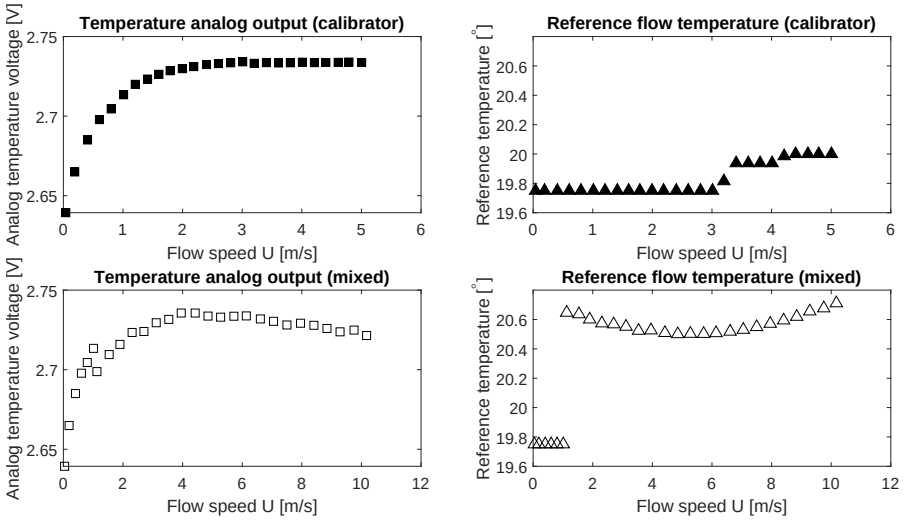

Figure 4.16: RevC analog temperature voltage output calibration difficulty.

4.3. Directional sensitivity

4.3.1. RevP airflow sensor

The direction sensitivity of the airflow sensor RevP is investigated by rotating the sensor with controlled stepper motor input in pre-defined XY, YZ and XZ planes as illustrated in Figure 3.5. At each rotation step, airflow sensor RevP's voltage outputs are sampled at 5 KHz and the recording lasts 5 seconds. Results are then time-averaged per rotation step. The stepper motor rotates the sensor at approximately 5 degrees per step and completes a full circle. Due to the slight difference in motor gear ratio compared to the designed specification, the actual change of angles is at 4.946 degrees per rotation step. This means when the rotation finishes one full circle, the sensor does not return to its starting position exactly, causing a small velocity jump that can be seen in Figure 4.18 for example.

From Figure 4.17 to Figure 4.19, the RevP outputs are fit with the combined King's Law coefficients from Table 4.1 and non-dimensionalised with the respective freestream flow speeds measured from the W-tunnel. It can be seen that with the increase in freestream speed, the RevP sensor becomes more directionally sensitive overall in all planes of rotations, with the XY plane being the least sensitive and the XZ plane the most sensitive. In all three planes of rotations, $-30 \sim 30$ degree is a region where the airflow sensor measurement is not affected by the angle between the incoming flow and the sensing thermistor. Beyond ± 30 to ± 45 degrees, the measurement results are still acceptable but the deterioration starts and becomes the worst when the incoming flow is tangent to the airflow sensor's sensing thermistor. This means if the airflow sensor is placed aligned with the wing surface, then its measurement performance is extremely unreliable if there is a lateral flow disturbance.

Note that these rotational tests are repeated for three sets of brand-new RevP airflow sensors given the available time in the wind tunnel testing slots. The potentiometer on the RevP sensor is untouched, considering the manufacturer claims that they pre-tune all of the sensors during their quality assurance stage. However, it can be seen from Figure 4.17 to Figure 4.19 that the RevP sensors still display output differences as the three colored curves representing 3 RevP sensors do not overlap with each other fully. Translating this into practical use, this means that when getting a new airflow sensor, either a new calibration procedure should be performed for each sensor, or a small software and hardware offset need to be applied, to improve the measurement accuracy. The first method requires significantly more time and effort, while the second method requires some fine adjustment with the potentiometer or in the software, and a validation source to compare with.

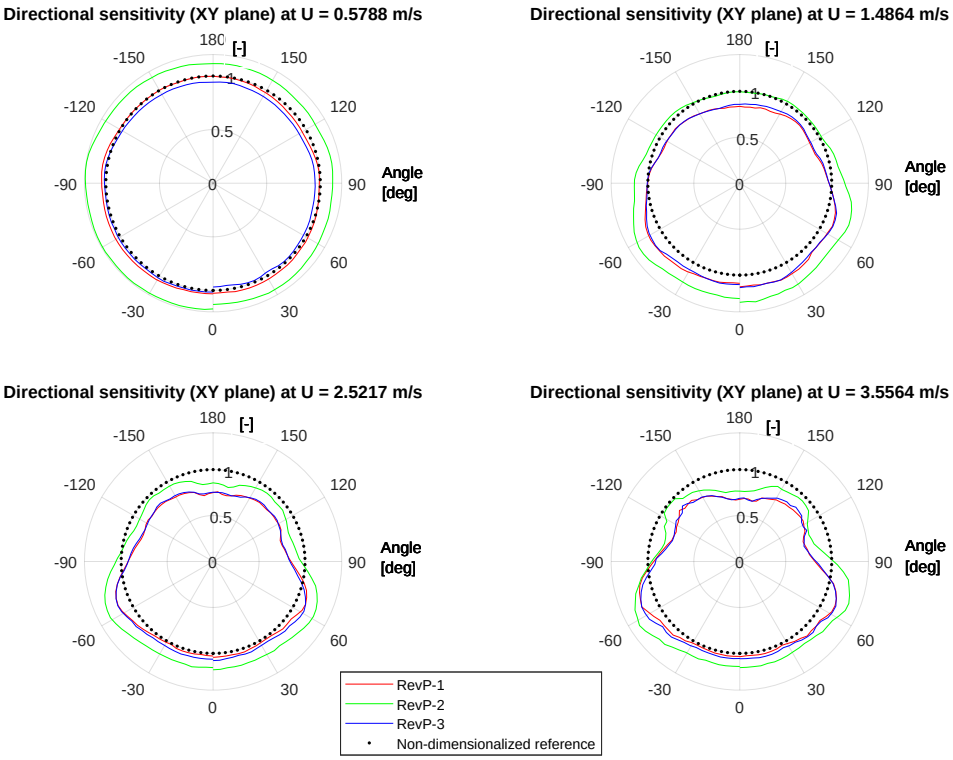

Figure 4.17: RevP: directional sensitivity about the XY plane at different mean flow speeds.

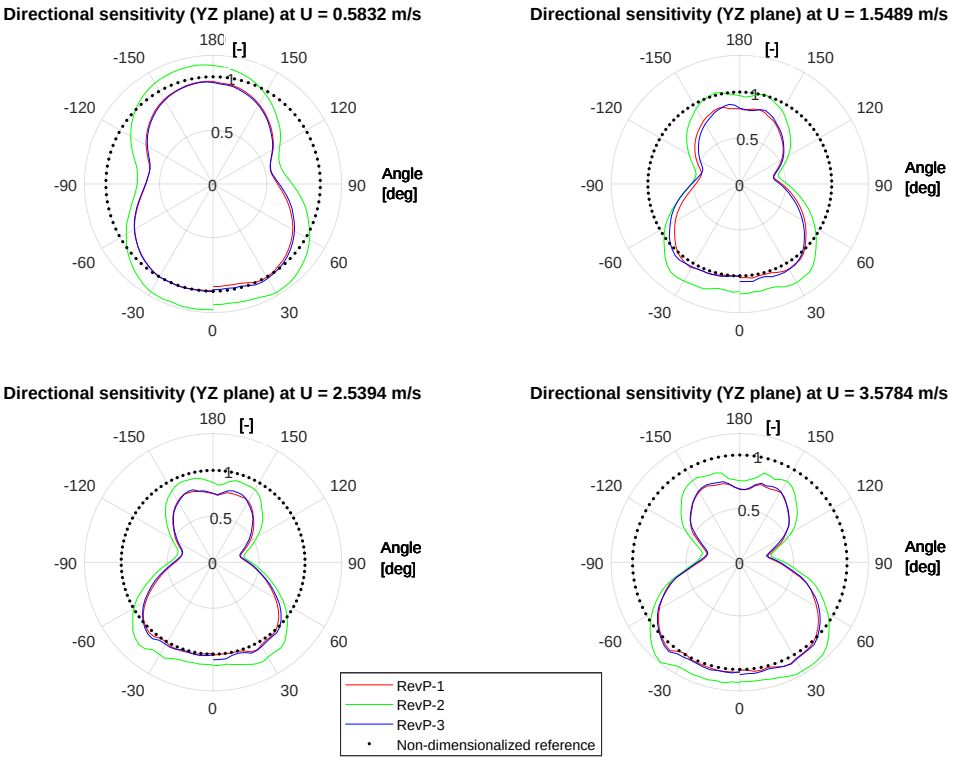

Figure 4.18: RevP: directional sensitivity about the YZ plane at different mean flow speeds.

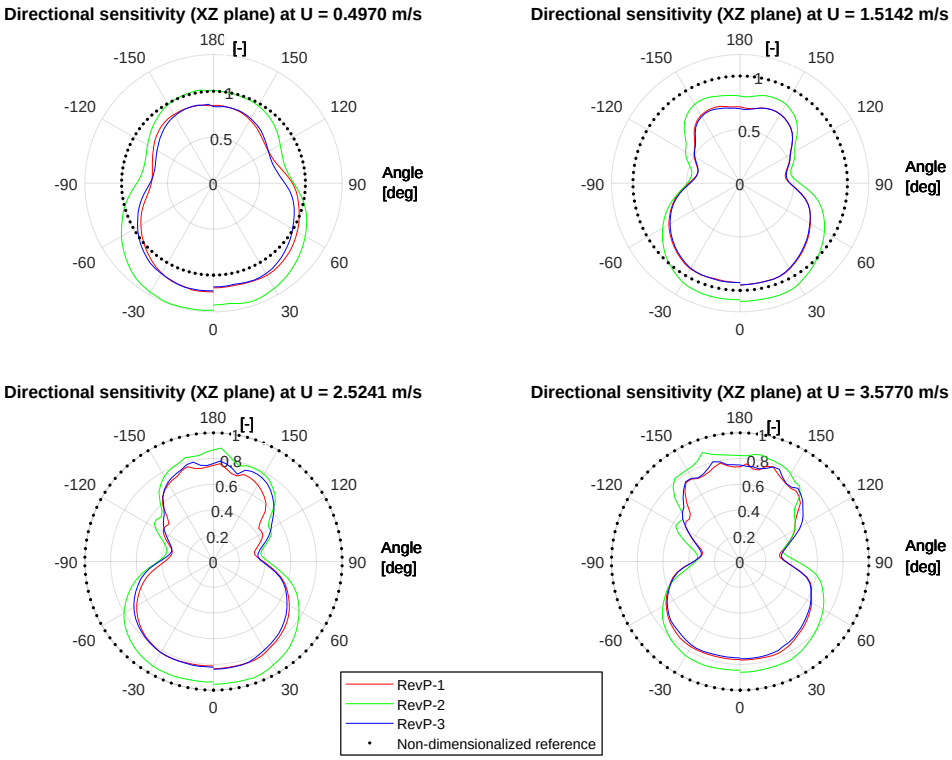

Figure 4.19: RevP: directional sensitivity about the XZ plane at different mean flow speeds.

4.3.2. RevC airflow sensor

The directional sensitivity of the airflow sensor RevC is investigated similarly like for the RevP sensor. The processed results are shown from Figure 4.20 to Figure 4.22. Overall, the RevC sensor is more directional dependent compared to the RevP sensor in all three planes of rotations, as reflected by the larger deviation from the non-dimensionalized reference. The $-30 \sim 30$ degree range is still the acceptable interval in all three planes of rotations where the airflow sensor measurement is not affected by the angle between the incoming flow and the sensing thermistor. One notable difference between the RevP and RevC performance is the repeatability of measurements. Despite each sensor has manufacturing difference and the small difference that might occur from different sets of tests, the RevC sensor has a lot worse measurement repeatability compared to RevP. This means if RevC sensor were to be used for airflow sensing, it would require a sensor-specific calibration prior to any potential applications for each new sensor. Otherwise, there is a high chance the calibration coefficients acquired through wind tunnel test campaign 1 will lead to measurement inaccuracies.

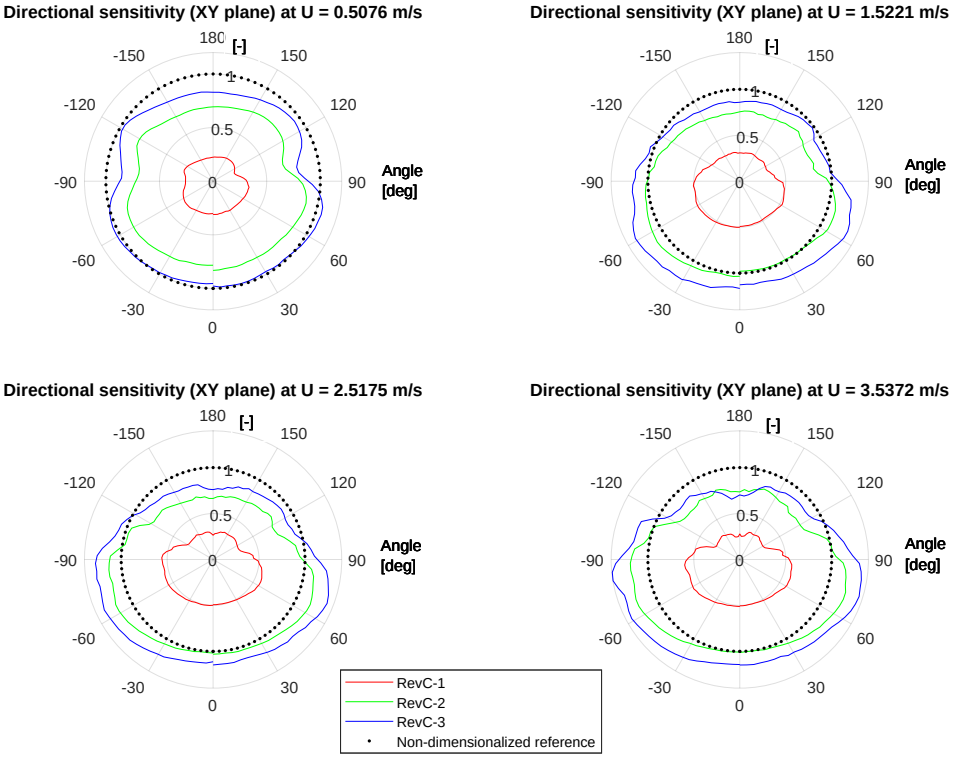

Figure 4.20: RevC: directional sensitivity about the XY plane at different mean flow speeds.

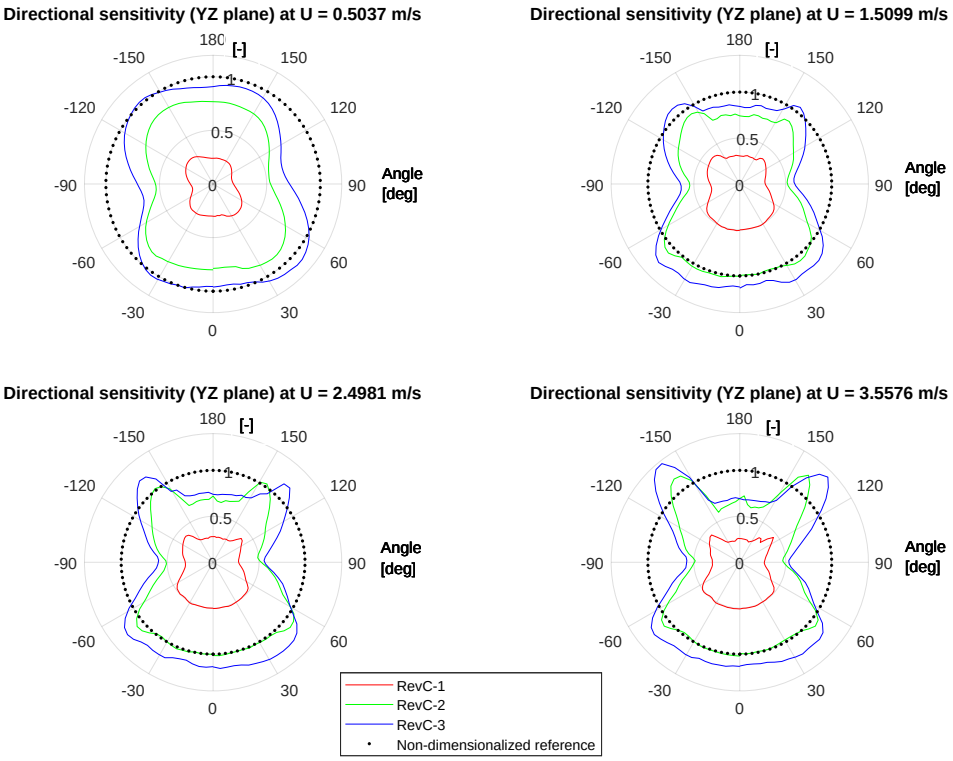

Figure 4.21: RevC: directional sensitivity about the YZ plane at different mean flow speeds.

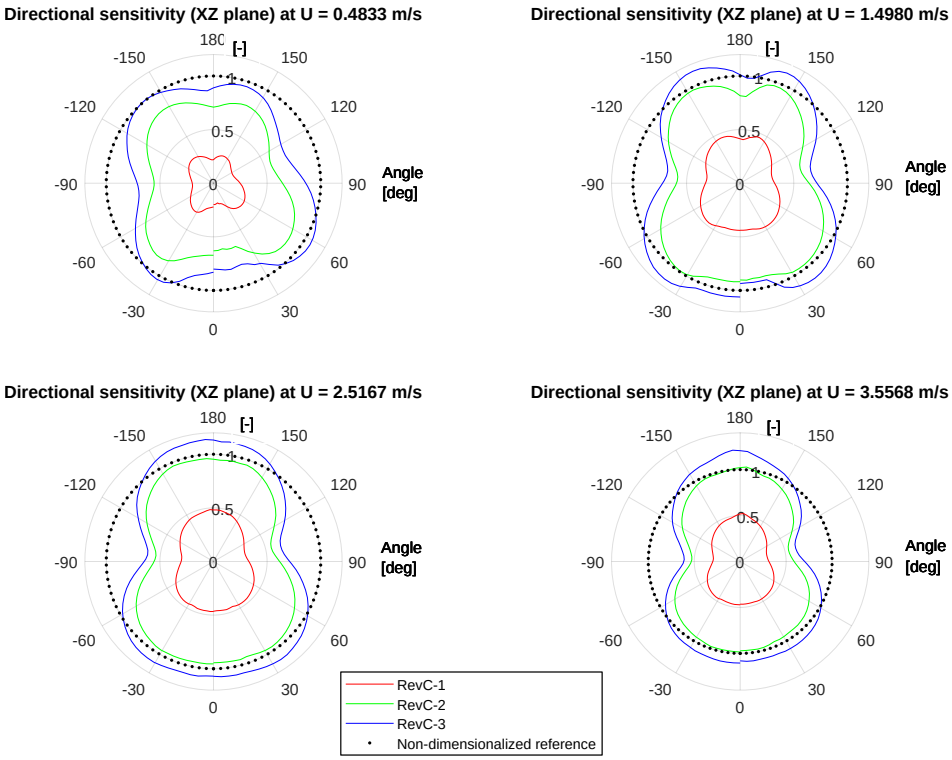

Figure 4.22: RevC: directional sensitivity about the XZ plane at different mean flow speeds.

4.3.3. Case study

To utilize the rich information from the directional sensitivity results, two simple case studies are presented here with the use of a RevP airflow sensor.

Flight at no wind disturbance

When an MAV is operating at no wind disturbance conditions, for example an indoor flight arena with confined space, the best airflow sensor placement configuration would be to align the MAV's axis that has more angular changes with RevP's Z axis, since RevP is almost omni-directional in the XY plane of rotation. In this way, the relative motion of the MAV to different directions will not effect RevP's measurements and its outputs could potentially be a reliable source of airspeed measurement. If this alignment could not be achieved due to different application needs, then within approximately $-45 \sim 45$ degrees' range, the RevP sensor can still be a reliable source of airspeed measurement.

Flight with small wind disturbances

Once there are small wind disturbances from the environment, till approximately 3.5 m/s, the directional dependence deteriorates as the wind speed increases, making the airspeed readings more prone to inaccuracies given the wind incoming direction is unknown. Given the worst directional performance near the ± 90 degree regions in all three planes of rotations, wind disturbances that come near a tangential direction with respect to the airflow sensing face could potentially bring the most challenge to the MAV's flight stability since the input airspeeds will be more than 50% less than the actual values. To solve this problem, more than one RevP sensor could be used for the airflow sensing. What's more, this directional sensitivity could be useful. The incoming wind direction can be extrapolated to a certain degree by using more than one RevP sensor. This would be interesting for MAV applications that can carry more than one airflow sensor in the future.

4.4. RevP and RevC comparison with hot-wire

As mentioned in Subsection 3.2.1, the minimum achievable turbulence intensity level of the W-tunnel flow is in the order of 0.5%. Turbulence intensity is defined as the root-mean-square (RMS) of the turbulent velocity fluctuations divided by the mean flow speed as expressed in Equation 4.3. When operated in the laminar flow regime, the left plot of Figure 4.23 confirms this order of magnitude in turbulence intensity. A small outlier is present around 1 m/s. After examining the raw data, a disruption to the measurements is found. This happened most likely due to some unexpected unknown external factor in the W-tunnel operating room, which could cause ambient flow disturbance at such a low freestream speed.

$$I = \frac{u_{RMS}}{\bar{u}} = \frac{\sqrt{\frac{1}{N}\sum_{i=1}^{N}(u_i - \bar{u})^2}}{\bar{u}} \tag{4.3}$$

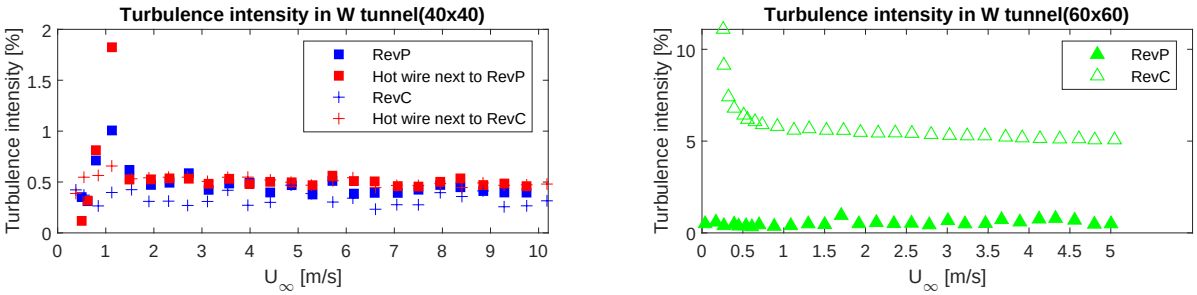

Figure 4.23: Turbulence intensity comparison among hot-wire, RevP, and RevC measurements of the flow in W-tunnel test section 40x40 (left) and 60x60 (right).

The same set of sensors were later used again during the wind tunnel test campaign 2 to just verify the same order of turbulence intensity for the freestream despite using the larger tunnel contraction and without the use of a test box for the Delfly tests. The results are shown in Figure 4.23. The RevP sensor's measurement results show the turbulence level is indeed in the order of 0.5 %. However, the RevC's measurement shows the turbulence level 10 times higher. This is unlikely since the wind tunnel configuration has not changed over the course of two months. When examining the raw analog voltage output data, the fluctuation level of the signal is consistently much higher. This could happen with the malfunction or deterioration of the sensor components. However, without the access to the hot-wire probe during the test campaign 2, this was not able to be further investigated to determine the exact cause to the higher signal oscillations.

4.5. Power consumption comparison

The current consumption of both airflow sensors under different freestream speeds are collected from the readings of the power supply benches during the wind tunnel tests. The power supply bench could only provide readings up to 2 digits, hence the segmented data in Figure 4.24. It can be seen that the RevC sensor consumes less heat current at most testing conditions. This is due to its sensing thermistor requiring less power to be heated up. If the freestream speed is around 2 m/s, then the current drain is about 1.5 % of the Delfly's peak operating current at a large thrust level. With a higher supply voltage needed, RevP would drain the battery power more than 2 times faster than RevC.

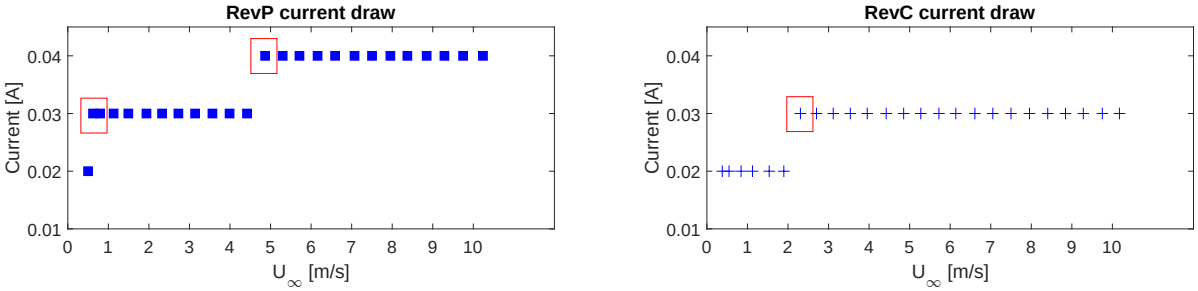

Figure 4.24: Comparison of RevP, RevC sensor's power draw from power supply bench.

4.6. The influence of turbulence grid

The turbulence level of the W-tunnel freestream with and without the add-on grid is shown in Figure 4.25. The turbulence intensity investigated here is of the freestream flow 20 cm downstream of the turbulence grid. As grid generated turbulence intensity decays with downstream distance at a certain rate (proportional to $x^{-5/7}$) [70], the turbulence intensity calculated here is only reflective of the flow approaching the measurement instruments at the core stream in the wind tunnel. Note that the hot-wire probe and the airflow sensors all could only provide one-component velocity measurements here.

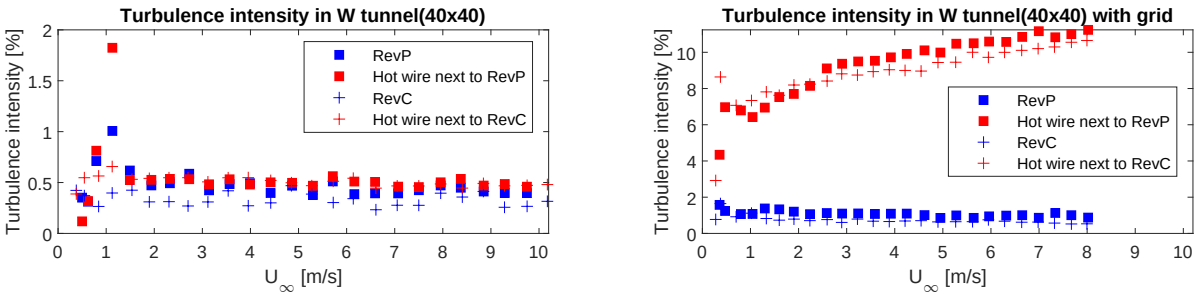

Figure 4.25: Turbulence intensity comparison among hot-wire, RevP, and RevC measurements of the flow in W-tunnel test section 40x40, without the add-on grid (left), and with the add-on grid (right).

The higher turbulence intensity shown on the right of Figure 4.25 confirmed the add-on grid's turbulence generation capability. Note that calculated turbulence intensities from the hot-wire measurements range from approximately 7 to 11 % as freestream speeds increase. This is a lot higher than what the RevP and RevC airflow sensors' results, which are less than 2 %. This requires further signal filtering before any conclusion can be drawn, due to the higher frequency components the hot-wire is capable of picking up. Low pass filters are commonly used in such an occasion, which cut off the frequency response that are beyond the range of interest to prevent the unnecessary inclusion of the higher frequency components of the measurement output noise in turbulent flow measurement [68]. To determine an ideal cut-off frequency, spectral analysis with power spectral density is performed on the raw output signal from the hot-wire measurements as shown in Figure 4.28 and Figure 4.29. As the energy level of the different frequency components decreases and enters a plateau around 100 Hz, the cut-off frequency is selected to be 100 Hz. An eighth-order butterworth filter with the MATLAB zero-phase lag digital filtering function *filtfilt* is used to filter out the higher order frequency components,which are primarily contributed by noise.

Figure 4.26 shows the turbulence intensity of the turbulent flow after the noise removal with the filtering. The freestream turbulence intensity is approximately 7 % with the hot-wire measurement results. This indicates that the RevP and RevC sensor's sensitivity reaches a threshold in sensing larger flow velocity fluctuations, with the RevP having about 0.5 % better performance than RevC in terms of the turbulence intensity. Methods such as the square-wave test or the sine-wave test com-

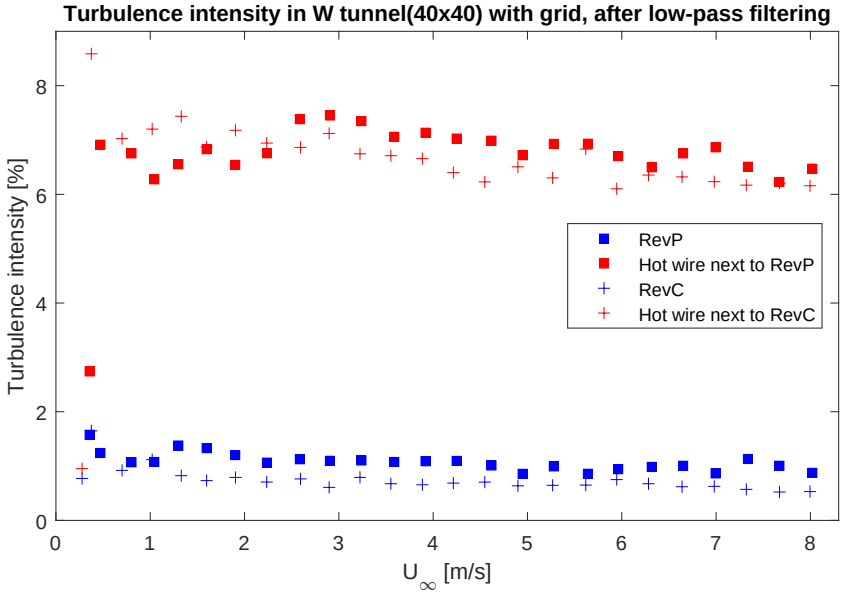

Figure 4.26: Turbulence intensity comparison among hot-wire, RevP, and RevC measurements of the flow in W-tunnel test section 40x40, with the add-on turbulence grid, after removing higher frequency components from the hot-wire measurements.

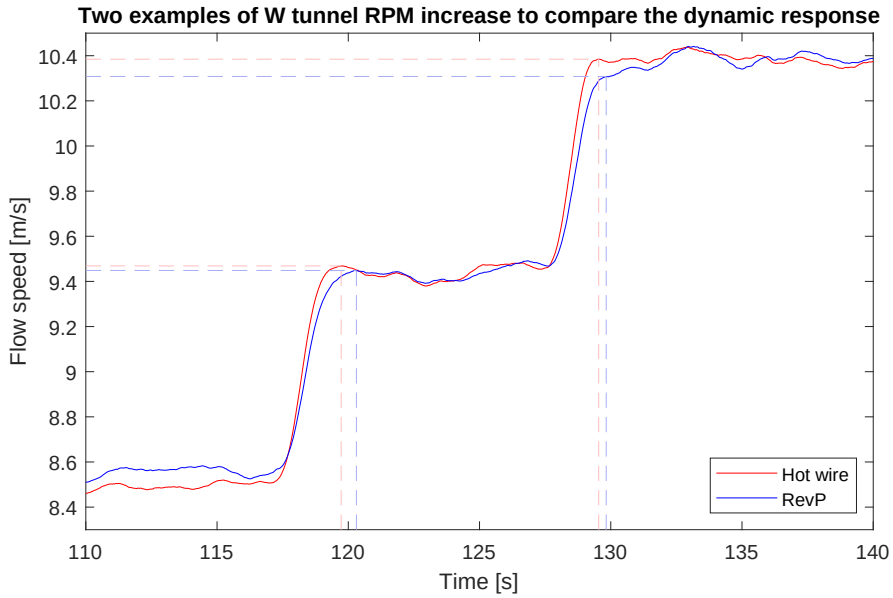

Figure 4.27: Dynamic response comparison between the hot-wire and RevP measurements in W-tunnel test section 40x40 by suddenly increasing the tunnel freestream speed, without the add-on turbulence grid

monly used in the determination of the frequency response of the constant temperature hot-wire anemometer could potentially be used in the future to further examine the frequency response over the whole frequency domain [23]. This reduced response sensitivity from the RevP sensor compared to hot-wire anemometer has also been observed during the laminar flow test regime, where the RevP sensor and the hot-wire probe undergoes sudden freestream speed increase simultaneously. In Figure 4.27, two of such freestream speed increases are presented, with the hot-wire reacting slightly faster to the flow speed change compared to the RevP sensor, at a time advance of 0.5816 s and 0.2872 s respectively.To use as a phase-advance airflow sensor, it is worth investigating the lag of the frequency response in the future, and whether it can be improved through circuitry re-design.

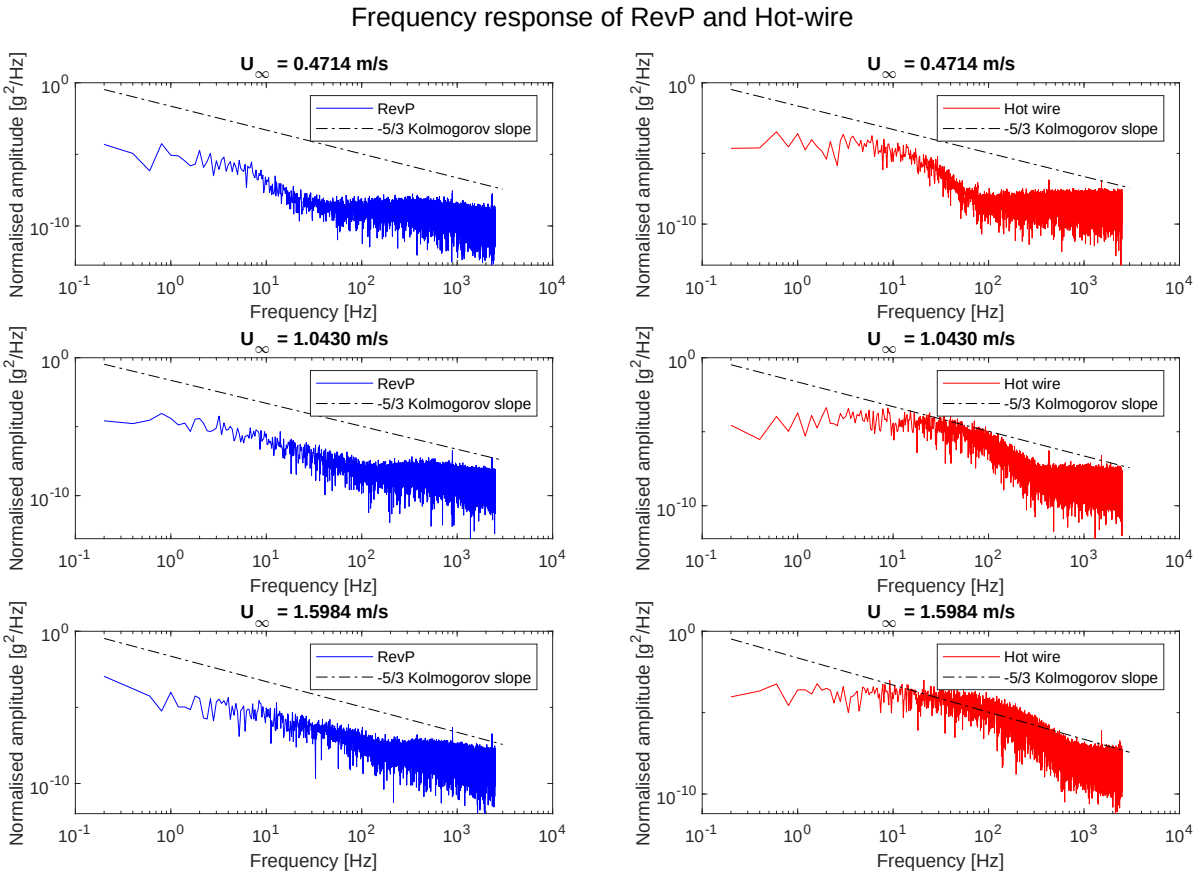

Figure 4.28: Power spectral density and frequency log-log plot of RevP and hot-wire measurements in different freestream speeds, with add-on grid for turbulence generation, with the -5/3 Kolmogorov slope displayed as reference.

In both Figure 4.28 and Figure 4.29, a line defined in Equation 4.4 based on Kolmogorov's -5/3 law of turbulence is plotted as reference, where the coefficient $c = 0.023$ is used for all plots to approximate the turbulent energy decrease trend. The idea behind the law of the -5/3 is that the energy density dissipates at a certain rate [74] with the assumption of flow homogeneity and isotropy. It can be seen that the RevP sensor's measurement energy level decay rate is closer to the Kolmogorov reference, while the RevC sensor and the hot-wire probe have a steeper decay. Overall, energy level decays as frequency increases. From the closer distance to the reference line, it is evident that the hot-wire probe can indeed pick up more higher velocity fluctuation contents compared to the other two airflow sensors, given its energy amplitude is higher.

$$y = c \cdot x^{\frac{-5}{3}} \tag{4.4}$$

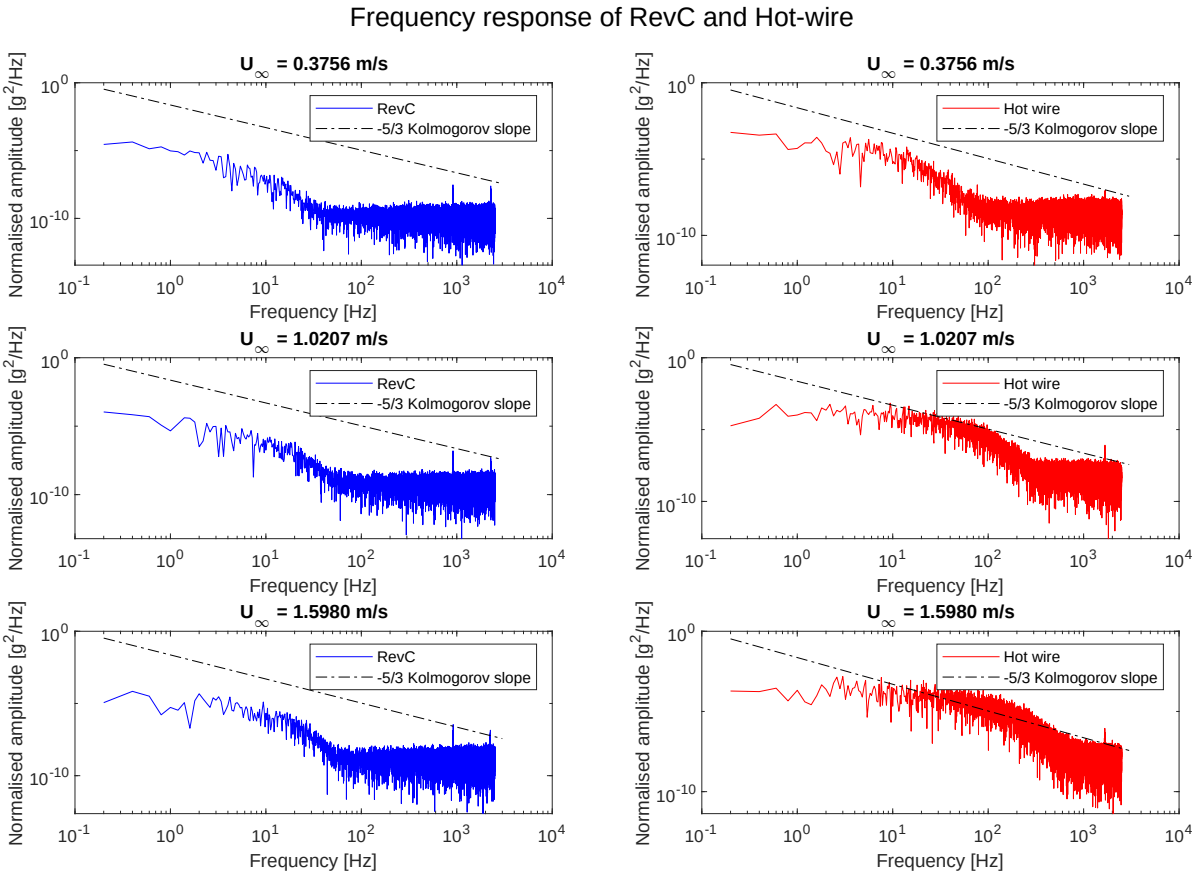

Figure 4.29: Power spectral density and frequency log-log plot of RevC and hot-wire measurements in different freestream speeds, with add-on grid for turbulence generation, with the -5/3 Kolmogorov slope displayed as reference.

4.7. Conclusion: the choice of RevP

The wind tunnel test campaign 1 investigates the calibration procedure and characterises the performance for both RevP and RevC airflow sensors. In terms of calibration procedure, RevP and RevC are both easy to calibrate with comparable accuracy compared to a hot-wire probe, although RevC's temperature analog feedback is very difficult to calibrate without a temperature regulated environment with reliable reference temperature. Without the onboard hardware compensation for temperature, RevC's calibration will also be more temperature dependent. In terms of directional sensitivity, both RevC and RevP sensors appear to be directionally independent within ± 30 degrees with respect to the incoming flow. The RevP sensor has less directional dependence at various freestream speeds. RevP sensor also has slightly higher dynamic frequency response to be able to capture approximately 0.5 % larger velocity fluctuations in turbulent flow. Besides, RevP sensor has better measurement repeatability when it comes to product quality just commercially off-the-shelf. This leads to the final choice of using RevP as the ideal airflow sensor onboard the flapping wing MAV for future experiments. One last note, RevC has an advantage at less supply power needed compared to RevP. For simple applications at larger flow speeds where there are more tolerance for errors, RevC could still be used as a less power consumption solution.

5

Results: Mounted Delfly test

In this chapter, the key results from the tests where the airflow sensor RevP is mounted on the flapping wing MAV Delfly Nimble are discussed. The influences from different throttle levels, body pitch angles, and freestream speeds are investigated in Section 5.1. Finally, a vibration analysis of the above factors is performed to identify the more important contributing factors to the measurement energy level in Section 5.2.

5.1. The three influence factors on the RevP measurements

The following test set-ups are configured during the mounted Delfly tests. The different influence factors investigated are listed in Table 5.1. These parameters are selected with the free flight scenarios in mind.

- Set the hovering position by placing Delfly Nimble as close to the zero degree body pitch angle as possible. Vary throttle levels at this hovering position
- Set the hovering position by placing Delfly Nimble as close to the zero degree body pitch angle as possible. Vary freestream velocities of the W-tunnel
- Set the forward flight position by placing Delfly Nimble at different body pitch angles, through adjusting the clamp in the mounted test set-up. Vary throttle levels and freestream velocities of the W-tunnel.

Throttle [%]	Delfly body pitch angle [deg]	Freestream speed U_∞ [m/s]
25	0	0
37.5	-15	0.5
50	-30	1
62.5	-45	1.5
	-60	2

Table 5.1: Wind tunnel campaign 2 test set-up parameters.

Note that since the throttle level is set by manually adjusting the position of the throttle stick, there could be a small deviation of approximately ±1%. With the mount test-rig, the Delfly body pitch angles are set manually and double checked with a level sensor, at ± 1 degree deviation. This set-up is to only help identify a more clear quantitative relationship of the body pitch angle's influence on the RevP measurements. It does not reflect well the real life scenarios, as body pitch angle varies during free flights.

The recording of each test configuration from Table 5.1 with certain throttle, freestream speed, and Delfly body pitch angle last 40 seconds. The obtained RevP readings are then pre-processed by removing the part of the data when flapping has not started and time averaged in Figure 5.1 and Figure 5.2. As noise from measurements is usually at high frequencies, the moving average filter which is essentially a low-pass filter could help remove the noise.

In Figure 5.1, the wind tunnel is not operating for all tests. The RevP measured speeds are mainly from sensor relative motions caused by flapping induced mechanical vibrations, despite the ambient influence from the indoor testing environment. Increasing the throttle level would increase this measured speed caused by relative motions from vibration. The overall RevP mean speed increase as body pitch angle increases between 0 ~ 45 degrees is not fully accounted for. A possible cause could be the ambient influence documented by W tunnel's Pitot tube system as it is more than 30% of the smallest mean speed here.

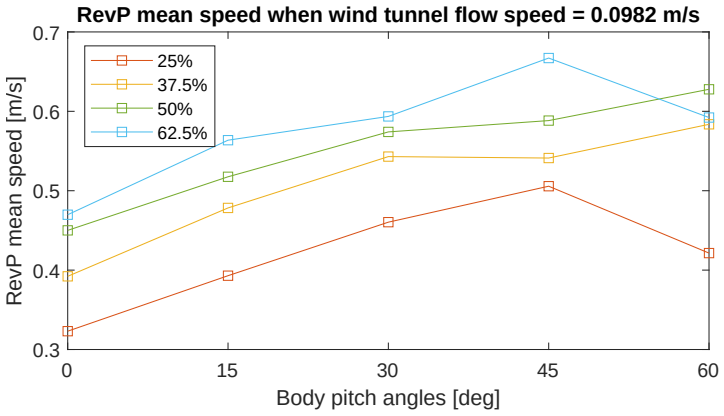

Figure 5.1: Delfly with RevP sensor onboard, W tunnel $U_\infty = 0$ m/s (Note that absolute values of the body pitch angles are taken here).

Figure 5.2 is processed similarly as Figure 5.1. But the influence due to mechanical vibration from flapping and any ambient disturbance recorded in Figure 5.1 is subtracted and the resultant RevP mean speed is non-dimensionalised with the respective freestream speed. It can be seen that after the removal of flapping induced influence, the RevP airflow sensor is capable of measuring the ambient flow disturbance speed at small body pitch angles (for $\theta < 30$ [deg], with approximately 10 ~ 20 % deviation from the reference line). This deviation is affected by ambient flow speeds and body pitch angles where the airflow sensor's directional sensitivity comes into play as the angle between the incoming flow and the sensing thermistor increases with an increase in body pitch angle. As the RevP sensor's directional dependence deteriorates rapidly beyond ± 30 degrees, the measured flow speed drops to 20 ~ 40 % of the true reference freestream speed as can be seen through the decreasing trend in Figure 5.2.

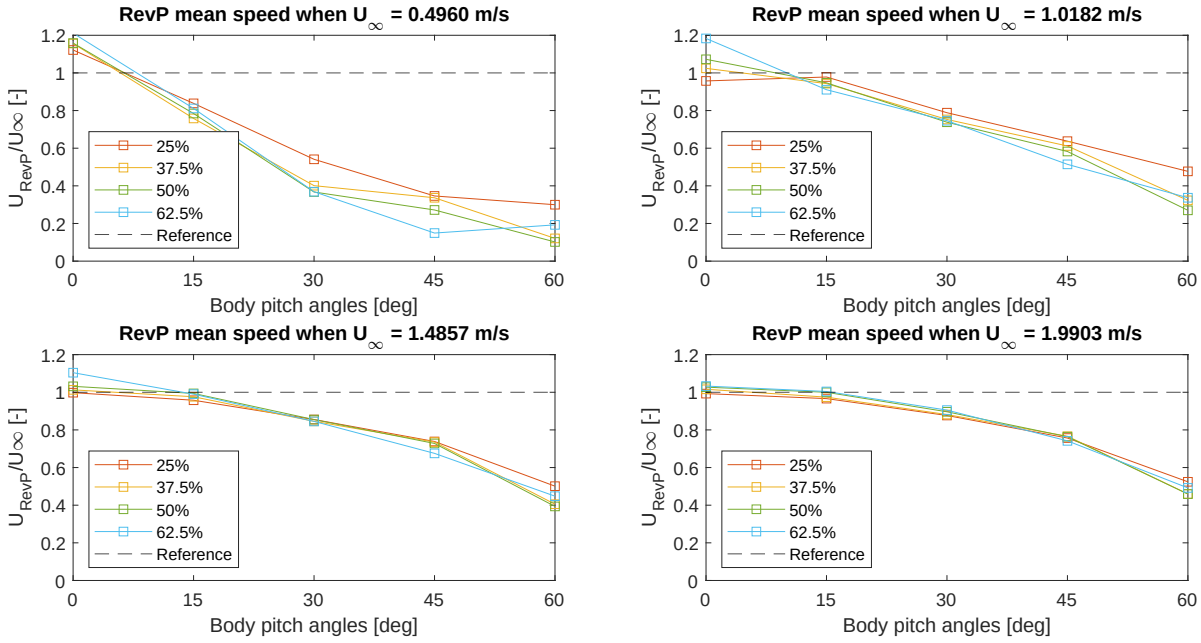

Figure 5.2: Delfly with RevP sensor onboard, W tunnel turned on (Note that absolute values of the body pitch angels are taken here).

5.2. Influence of flapping induced vibration on measurement accuracy

To minimize the Delfly fuselage body vibration during a mounted test or a tethered flight test, an optimal placement of the sensor on the fuselage is important. To evaluate the amount of the influence from vibration, the vibration energy level needs to be compared. The vibration levels at different test conditions for the mounted Delfly tests are discussed in this section. More comparison with tethered hover flight will be explained in Section 6.2.

5.2.1. Vibration analysis from Delfly linear accelerations

A fast Fourier transform (FFT) algorithm is useful at analyzing vibration given that the dominant frequency components are finite. With potentially random vibration involved given the various flying conditions Delfly are capable of, power spectral densities (PSD) are more suitable to characterize random vibration signals and allow the comparison of vibration levels for signals with different lengths. This is achieved as a PSD is computed by multiplying each frequency bin in the FFT with its complex conjugate, which leads to only the real-valued spectrum of amplitude g^2. This amplitude value is then normalised to the frequency bin width (with units: g^2/Hz) which removes the dependency on frequency bin width, and thus further allows the comparison of vibration levels under different test conditions [71].

Signal length affects the amplitude of the FFT results but not the PSD results as they are normalized with frequency bin width to allow further comparison of vibration energy levels for different test sets. In Figure 5.3, a representative case of spectral analysis on the linear acceleration in Z direction is presented with a maximum throttle level during the test. It can be seen that the first peaks of frequency contents (13 and 14 Hz) are smaller than the Nimble's hovering flapping frequency 17 Hz. This is mostly due to the slightly smaller throttle level compared to the hovering flights and the test rig set-up that clamps the drone tightly.

Z direction has more energy at all throttle levels compared to X or Y direction as shown in Figure 5.4. This is mostly due to the force generation which has the major component along the Z direction. Increasing throttle level would also increase the vibration energy level. Here the raw PSD data of the full data sets are smoothed with a Gaussian-weighted moving average filter at window length 50 to

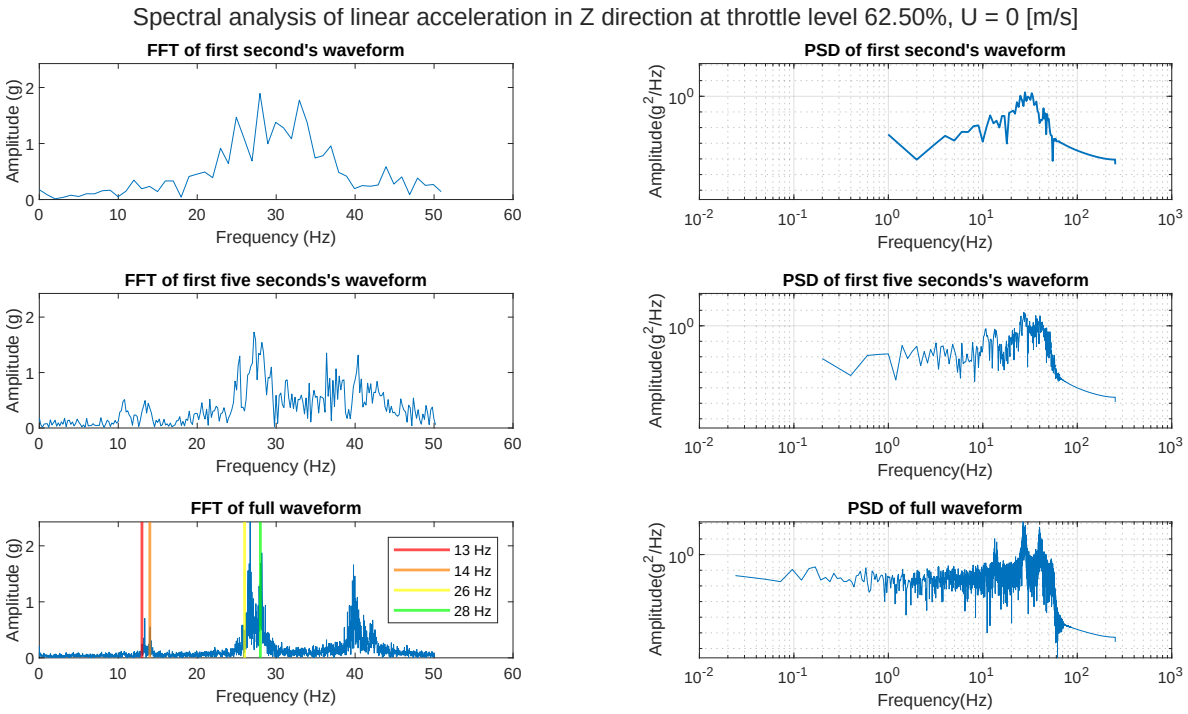

Figure 5.3: Vibration analysis example: Delfly mounted test, with RevP sensor onboard, W tunnel off, throttle level at 62.5 %.

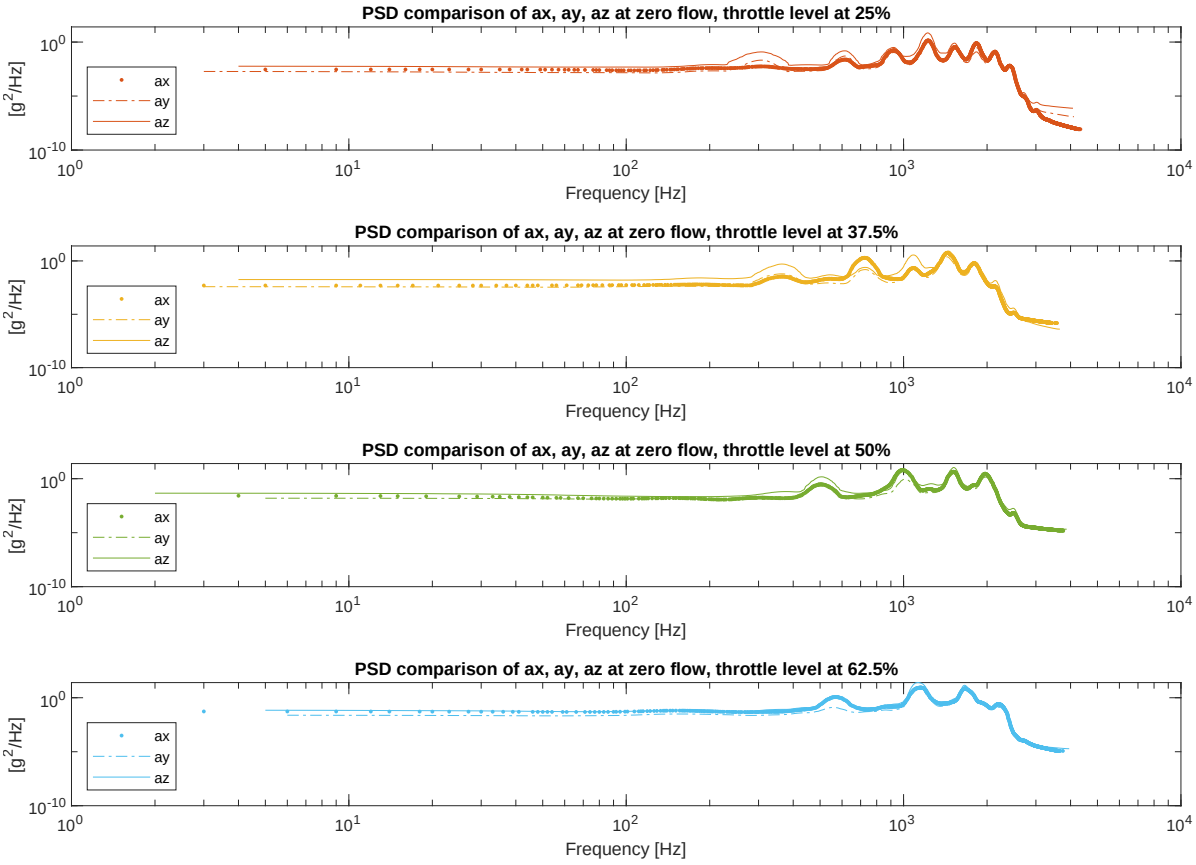

Figure 5.4: PSD comparison: Delfly with RevP sensor onboard, W tunnel off, at various throttle levels.

preserve the key details while reducing the noise level of the PSD data.

Figure 5.5 shows that the variation of flow speed and pitch angle does not affect the vibration energy level in a significant way, while throttle level variation does.

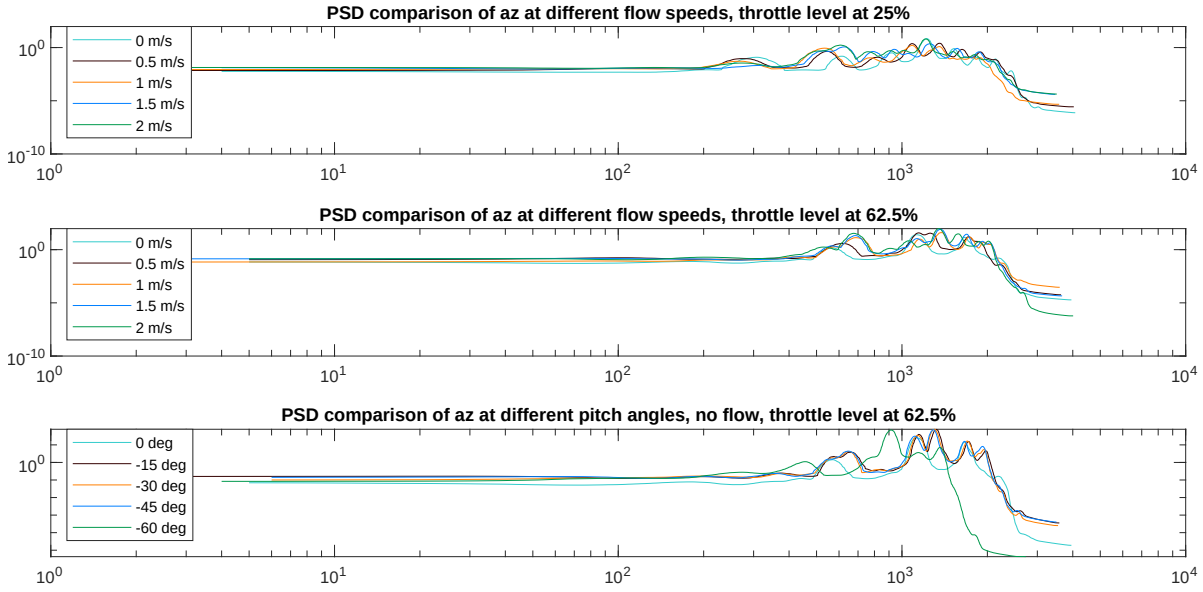

Figure 5.5: PSD comparison: Delfly with RevP sensor onboard, under different flow speeds and throttle levels (top and middle), or different pitch angles (bottom).

5.2.2. Vibration analysis from RevP measurements

The influence of flapping induced vibration can also be seen directly from the airflow sensor RevP's measurements. In Figure 5.6 and Figure 5.7, both raw and filtered airflow speed data for three flapping cycles without and with freestream flow are presented for comparison. Flapping frequency deduced from these 3 periods are summarised in Table 5.2 and Table 5.3. The increase in flapping frequency due to the throttle level rising can be seen from the shorter time needed to complete three full flapping cycles at both freestream conditions. The majority portion of the RevP measurement oscillation can be encapsulated within $\pm 2\sigma$ standard deviation, regardless the throttle level or the freestream speed. The RevP measurement standard deviation values themselves increases as the freestream speed increases, although still at a $1 \sim 2$ % low level compared to a flow disturbance of the order 0.5 m/s. The above figures and values indicate that flapping induced vibration does have a visible influence on the RevP measurement fluctuations by creating an artificial flow speed caused from the relative movement of the airflow sensor, although it is small enough comparing to the ambient flow conditions and the effects can be filtered out through some low-pass filters during an active application of the airflow sensor onboard a flapping wing MAV.

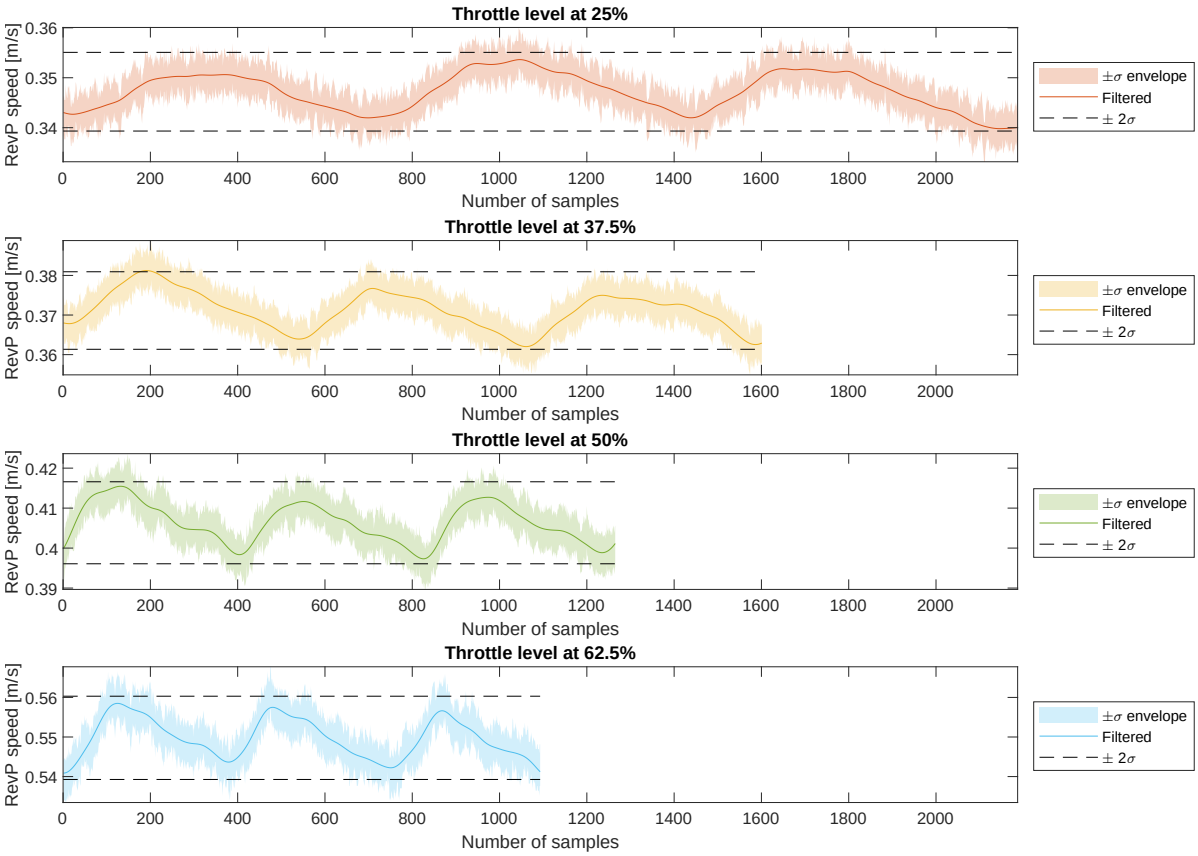

Figure 5.6: RevP sensor data in 3 periods, W tunnel off, at various throttle levels. Data is sampled at $5KHz$.

Throttle level [%]	Deduced flapping frequency [Hz]	Standard deviation σ [m/s]
25	6.86	0.0039
37.5	9.37	0.0049
50	11.86	0.0051
62.5	13.72	0.0053

Table 5.2: Flapping frequency deduced from the oscillations in the RevP measured data, zero wind tunnel freestream.

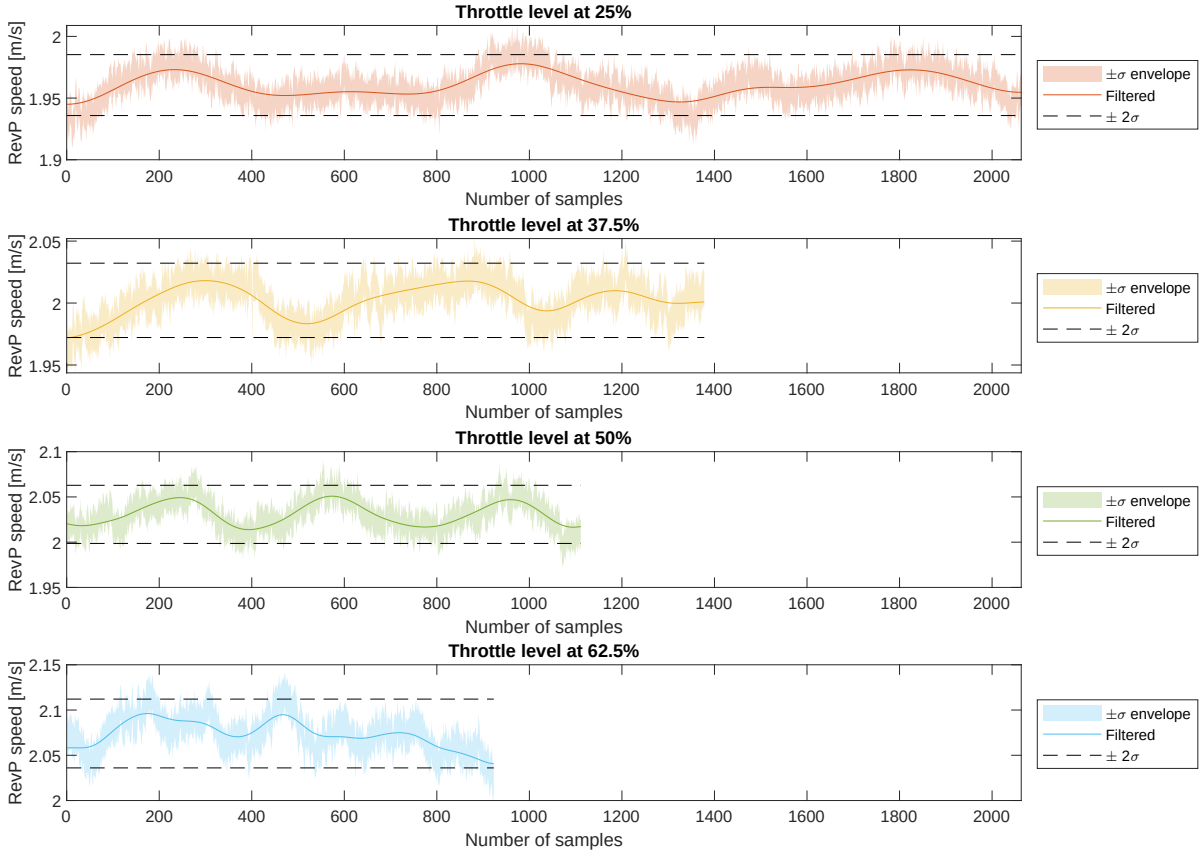

Figure 5.7: RevP sensor data in 3 periods, W tunnel on at U_∞ = 1.9903 m/s, at various throttle levels. Data is sampled at $5KHz$.

Throttle level [%]	Deduced flapping frequency [Hz]	Standard deviation σ [m/s]
25	7.27	0.0123
37.5	10.89	0.0150
50	13.50	0.0161
62.5	16.25	0.0190

Table 5.3: Flapping frequency deduced from the oscillations in the RevP measured data, W tunnel on at U_∞ = 1.9903 m/s.

6

Experimental validation

Hovering and steady forward flight tests are often used in flapping wing MAV to examine its performance under stable flight conditions [78]. To examine the airflow sensor RevP's measurement validity compared to the mounted wind tunnel test's results, hovering tests are chosen for repeatable experiments. Extra pre-flight preparation procedures need to be done on both hardware and software aspects of the Delfly Nimble to realize a stable flight with the add-on weight from the airflow sensor RevP. In the end, the RevP measurement results under no flow disturbance will be analyzed and RevP's performance reliability will be evaluated.

6.1. Tethered flight tests in the Cyberzoo flight arena

Due to the Delfly Nimble's 1-2 grams' payload limitation, it is a challenging task in terms of performing flight experiments to have the RevP airflow sensor onboard. The Delfly Nimble used in the experiments is equipped with the RevP airflow sensor which weighs 31.3 grams in total. To sustain stable flight, it requires extra thrust and consumes battery power faster, which further shortens the available flight time. The RevP sensor consumes 30 ~ 40 mA and needs 12 V power source. As Delfly Nimble is powered by 3.7 V 180 mhA LiPo battery, external power supply is needed to power up the RevP sensor. The downside of this solution is the external cables add extra weight and drag which makes performing a stable flight even more challenging. In the following sections, the preparation steps taken to allow the realization of multiple repeated stable hovering flights for effective data acquisition are described in more details.

6.1.1. RevP sensor configuration

The electronic circuitry design from the manufacturer Modern Device allows the possibility to separate the airflow sensor's main board with the sensing fingers (including the sensing thermistor, the reference thermistor and the temperature sensor as illustrated in Figure 6.1). This can be done by cutting the PCB apart by tracing the black line that goes through the 10 clustered soldering pads as shown in Figure 6.1. This knowledge was discovered by the author after the wind tunnel tests through further electronics self-study and testing to verify the airflow's usability after the cutting. In fact, both RevC and RevP sensors have this possibility to separate the PCB with the sensing fingers if an application could benefit from this separation.

The separated RevP sensor can then be re-connected by soldering 5 cables from the soldering pads on one side of the separation line to the soldering pads on the other. A type of thin copper wires (0.15 mm in diameter) is used to minimize the weight onboard and added cable resistance that could affect the validity of the wind tunnel calibration results. This separated RevP configuration has the advantage that during an actual flight test, the main board of RevP can be placed near the

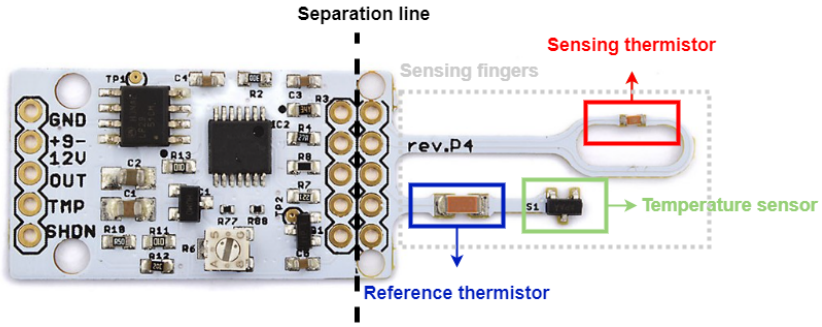

Figure 6.1: RevP sensor sensing fingers' components; The black dotted line is where the RevP sensor is separated

center of gravity of Delfly Nimble (or anywhere suitable for other MAV applications) and the sensing fingers can be placed ahead of the MAV wing to gain time advantage of sensing any flow disturbance in advance.

6.1.2. Flight test set-up

During the hovering flight tests, to reduce the body vibration's influence on the airflow sensor's measurements, the RevP is no longer placed entirely on the tip of the body fuselage as it was during the mounted wind tunnel tests. Instead, the major weight of RevP (i.e. the main board) is placed at the center of gravity and the sensing fingers at the top of the fuselage rod. This placement set-up is illustrated in Figure 6.2.

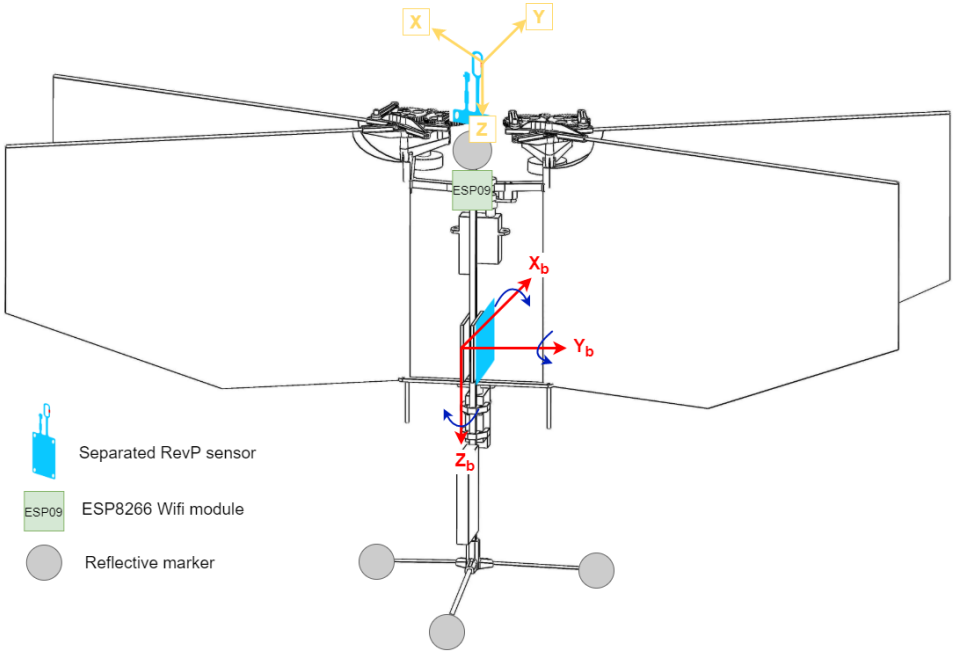

Figure 6.2: Test set-up of Delfly Nimble with RevP sensor onboard. The XYZ coordinate system marked in yellow is for indications of the airflow sensor RevP. The $X_bY_bZ_b$ coordinate system marked in red defines the body frame of Delfly Nimble. The wing following the Y_b direction is defined as the right wing, while the other as the left wing.

The airflow sensor RevP's sensing fingers are mounted on the tip of the fuselage carbon rod with a 3D printed T-shaped part to bind the sensing hoop more tightly onto the fuselage to minimize the influence caused by vibrations during flapping. The sensing fingers are placed ahead of the leading edge of the wing, at a distance matching the wind tunnel configuration. Note that it would be useful to investigate an optimal distance of how much ahead of the wing the sensing fingers should be

placed in the future by balancing between the actual flow disturbances and the disturbances measured by the airflow sensor. Their correlation decreases as the distance increases. This procedure is common in fixed-wing applications when Pitot tubes are being used as the tube length affects the actual sensing distance ahead of the wings [80].

A minimum of four reflective markers are needed to define the body of Delfly Nimble with OptiTrack motion tracking system to allow the guidance flight mode of Delfly Nimble. This enables Nimble to be able to hover above a fixed waypoint to have a better hovering test repeatability for data collection. These four markers are placed differently as illustrated in Figure 6.2 compared to the original configuration used by Karásek et al. [36]. There are two reasons for this consideration.

First, the sensing fingers of the airflow sensor RevP have already used the limited space at the top of the fuselage rod. In the wind tunnel mounted tests and in any actual free-flight tests, there are not or would not be reflective markers surrounding the airflow sensor, of which their presence could cause unwanted measurement noise to the RevP considering the fluid-structure interaction just ahead of the leading edge of the flapping wings.

Second, as this test set-up with the airflow sensor onboard is already the heaviest Delfly Nimble that has been reported so far (previous record 29.92 grams with a VL53L0X range sensor and a custom made monocular camera added [60]), a stable free hovering flight is more challenging to achieve. The tethered configuration to power up the airflow sensor RevP and its data acquisition with the extra cables brings extra difficulty to a successful hovering flight. Placing the three main OptiTrack markers at the bottom of the fuselage rod lowers Nimble's center of gravity and reduces the weight concentration near the top of the body fuselage. Such a configuration significantly reduces the tumble-over of the whole Nimble at the start of hovering stage if the markers were placed at the top where the PID controller can not regulate the position fast enough due to the drastic body movements. This indicates an improvement in dynamic stability, although at the cost of control effectiveness. When a pitch command is given, the normal drag force acts on a larger moment arm with this placement configuration and results in a larger counter moment, which reduces the overall control effectiveness [59]. In practice, this requires the drone to be at an optimal state for hovering flight as the control commands will be less effective to adjust the flight state. The fourth marker is placed as far as possible from the 3 main markers to increase the detect-ability for the OptiTrack motion capturing given its larger position difference from the 3 main markers. In the original configuration by Karásek et al. [36] and later used by Bains [9], this fourth marker is glued at the center of gravity near the autopilot board. This is not possible for the current tests as the main board of the RevP sensor is already glued at the back side of the autopilot board as shown in Figure 6.2. With the dense electrical wiring there, there is not enough space to place the fourth marker in a steady fashion. Thus, it is placed at the only remaining space on the fuselage rod, which is just beneath the airflow sensor's sensing fingers. This marker set-up proves to be easily track-able with OptiTrack motion capturing system and could enable stable hovering tests under guidance mode. The actual Cyberzoo test photos with the complete test set-up can be seen in Figure 6.3.

Note that a short ribbon is attached to the Nimble for protection purpose as can be seen in Figure 6.3. To be able to have one successful hovering flight, dozens of crashes happen. Given this heavy set-up, each crash at a hovering height of 2 m would be deadly to Nimble's fragile components. Repairing and tuning to bring Nimble to a flight-ready state could easily take more than 50% of the actual experiment time. Thus in case of a crash, the ribbon can be used to pull and catch the drone so it does not crash to the ground. Although the presence of the ribbon adds extra weight and create unwanted wake interactions, its useful protection function saves huge amount of testing time with less frequent need for repairing.

The final step to ensure a stable hovering flight involves a fine tuning of the PID controller used in the OptiTrack guidance loop. Along with the PID controller used for Delfly Nimble's active attitude stabilisation, the PID controller of the guidance loop is used to regulate the position of the Delfly

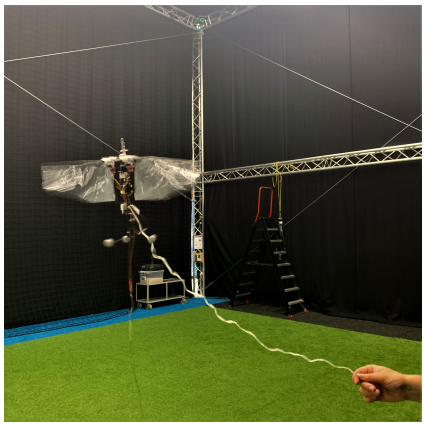

(a) Hover Delfly to a pre-set waypoint

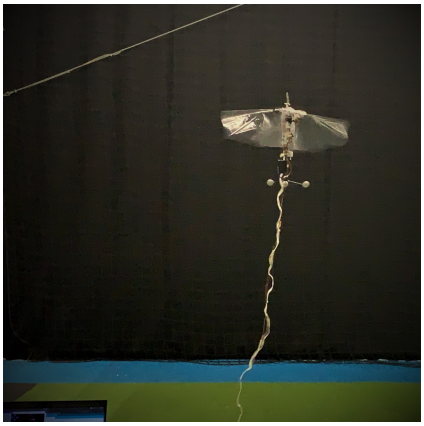

(b) Delfly hovers at fixed waypoint with the OptiTrack guidance

Figure 6.3: Delfly Cyberzoo hovering flight tests with RevP wind sensor onboard

with the position inputs from the OptiTrack motion capturing system, in particular, the horizontal control loop. The gains of the controller are determined by trial and error through actual flight performance in hovering tests. The actual steps taken to reach a stable hovering flight with minimal oscillations are explained in Appendix B.

It is not necessary to tune the I_{gain} gain as Nimble could already reach the pre-set waypoint in a timely manner with the newly tuned P_{gain} and D_{gain} values. If needed, the I_{gain} could be increased to further shorten the time to reach a setpoint, but at the cost of a few oscillations of overshoot potentially before stabilizing. This is not desired considering the presence of external power and signal cables of the airflow sensor. As a reference, the gain values used in the original Delfly's horizontal guidance control compared with the ones used in this test set-up are summarized in Table 6.1.

GUIDANCE_H	P_{gain}	D_{gain}	I_{gain}	Nominal hover throttle
Original Delfly	120	40	0	0.77
RevP sensor onboard Delfly	1250	450	0	0.85

Table 6.1: Delfly horizontal control under OptiTrack guidance mode PID controller parameter tuning

As the Delfly Nimble test set-up used in the hovering tests is about 11% heavier than the original Delfly Nimble, the expected throttle percentage needed for hovering has to be increased from the original 77% to provide the extra thrust needed. After some trial and error, an 85% is used which can maintain an optimal hovering height at 2 m above the ground while Nimble's fully-charged LiPo battery can sustain about 1 min stable hovering flight before the battery continuous discharge leads to fluctuating power output that leads to more oscillations in the Nimble hovering.

An overview of the three data acquisition sources is summarized in Table 6.2. First, the onboard 6DOF IMU (MPU 6000 from INVENSENSE) is integrated to the open-source STM32F4-based Lisa/MXS 1.0 autopilot PCB and consists of a gyroscope and an accelerometer. The MEMS 3-axis accelerometer measures the acceleration rates of a body a_x, a_y, a_z in its own instantaneous rest frame in relation to the 3 Cartesian coordinate axes. The 3-axis gyroscope measures body angular velocity change rates a_p, a_q, a_r in orientation along the roll, pitch and yaw axes. The Paparazzi autopilot [2] has pre-defined parameters to translate the angles from the IMU frame to the Delfly Nimble body frame, denoted as body angles ϕ, θ, ψ. This is pre-determined based on the mechanical mounting of the autopilot board which is to the left of the body fuselage where the side of the IMU module faces the fuselage rod. The throttle level δ_T is also recorded. All these information are logged to an SD card that is directly connected to and placed onto the autopilot board. The logs are extracted and post-processed in MATLAB.

Second, a Teensy 4.1 microcontroller unit (MCU) development board (ARM Cortex-M7, at 600 MHz clock speed) that is capable of converting the analog signals from the airflow sensor RevP into digital signals E_{temp} and $E_{airflow}$, which can then subsequently be logged to the SD card in the native SD card port of Teensy. The Teensy 4.1 is capable of acquiring data at higher than 22 kHz with its analog to digital converter (ADC). To be consistent with the airflow sensor data acquired in wind tunnel tests, a 5000 Hz sampling frequency of the airflow sensor data through the Teensy ADC is maintained. Instead of writing the data to the SD card as the real-time measurements proceed, it is stored in a fixed-size local buffer. Only after the buffer has been completely filled with data will it be written to the SD card, thereby reducing the total latency induced by the writing process. This way, the time gap caused by buffer writing to the SD card when the real-time data could not be written to the buffer is reduced to around 30 ms, maintaining the data loss rate at a lowest possible level. The purpose of using this external data acquisition for the airflow sensor is to gather data at a high sampling frequency which is comparable to previous wind tunnel tests, to get as much flow information as possible since the airflow sensor's performance under actual flights is still being evaluated at this proof of concept stage. This method generates a huge amount of data that the current Delfly Nimble onboard data logging system would not be able to store at a high rate given the existence of other logged parameters. Besides, potential CPU overloading could cause significant numbers of data frames being lost at higher sampling rates [8]. Once the performance of the airflow sensor is more certain, the Delfly Nimble's autopilot processor STM32F405 (ARM Cortex M4 at 168 MHz clock speed) with its 12-bit ADC (higher resolution than Teensy 4.1's 10-bit ADC) can be utilised to directly log the airflow sensor's data. The airflow sensor's data can then be fused into existing sensory information and upgrade the MAV's control strategy to tackle airflow disturbance. For such an application, the airflow data also can be sampled at a lower frequency which reduces the amount of data that needs to be stored to the logger.

Third, OptiTrack motion tracking system captures the position change of the reflected markers which register the position change of Delfly Nimble in the Cyberzoo inertia frame of reference. It helps to observe the amount of oscillations Delfly Nimble undergoes during the hovering flights.

Data acquisition source	Obtained data	Symbol	Sampling frequency $[Hz]$
On-board Delfly	Linear accelerations	a_x, a_y, a_z	512
	Angular accelerations	a_p, a_q, a_r	512
	Throttle level	δ_T	100
	Body angles	ϕ, θ, ψ	500
Off-board Teensy	RevP temperature analog voltage	E_{temp}	5000
	RevP airflow analog voltage	$E_{airflow}$	5000
OptiTrack	Position of Delfly markers	x, y, z	200

Table 6.2: Cyberzoo test campaign data acquisition overview

6.1.3. Extra set-up considerations for measurement accuracy

As the signal and power supply cables to the RevP will be at least 1 m longer than the ones used in wind tunnel tests to be able to allow a hovering flight above ground with sufficient height, the analog voltage drop and signal-to-noise ratio is investigated. The longest possible cable when analog signal output performance starts to have a more significant deterioration is approximately at 1.5 m. The more detailed investigation on this concern is presented in Appendix C.

To supply the airflow sensor RevP with 12 V, an external power supply bench is needed as Delfly Nimble's battery is 4.2 V only at full charge and carrying a step-up voltage regular is not an option with its added weight to the already heavy system. The cable is long enough to allow Delfly to hover at a height free of ground effects but also can not be too long as the increase in cable length increases

the resistance before power is reached at the sensor load. Fortunately, a power supply with remote sensing is available. It uses an extra set of power and ground wires to regulate the desired voltage at the airflow sensor by adjusting the power supply's output voltage a bit higher to make up for the drops in the sensor load leads. Note that this external cabling and power supply set-up would not exist if an airflow sensor can just rely on the MAV onboard power supply, which brings up the power consumption reduction challenge for future airflow sensor design.

6.2. Without wind: Hovering flight verification

To validate the test model constructed from wind tunnel tests' data, five repeated tethered hovering flight experiments are performed successfully in the Cyberzoo flight arena. The five datasets from Delfly and the RevP airflow sensors during the full flight session are presented as follows.

Figure 6.4a to 6.4e can be divided to four stages based on the rectangle divisions (alternating between not coloured, coloured, not coloured and coloured). Stage 1 is from RC direct manual mode[†] to attitude stabilisation mode [†] where the Delfly starts to flap and gets ready to hover above the waypoint before entering the OptiTrack navigation mode[‡]. At the end of Stage 1, the navigation mode is triggered and the controller with OptiTrack feedback in the horizontal guidance loop steers Delfly as close to the set waypoint as possible. This involves a sudden pitch forward motion to correct for the offset between the current hovering position and the chosen waypoint, considering the manual hovering before the navigation mode is not exactly at the set waypoint. This sudden pitch motion increases the airspeed and can be seen at the peak of the start of Stage 2 despite no ambient flow is blown to Delfly. After a few seconds, Delfly enters into a stable hovering flight position as seen in Stage 3 where the oscillation of pitch angle is minimal given the battery is still operating at a decent level. However, due to the heavy set-up compared to the original Delfly Nimble, power is drained faster and increases the unstable behaviour of the drone, which marks the entering of stage 4 where Delfly starts to oscillate more. As the body pitch angle oscillates more, the airflow sensor's reading is affected more by the oscillatory relative motions.

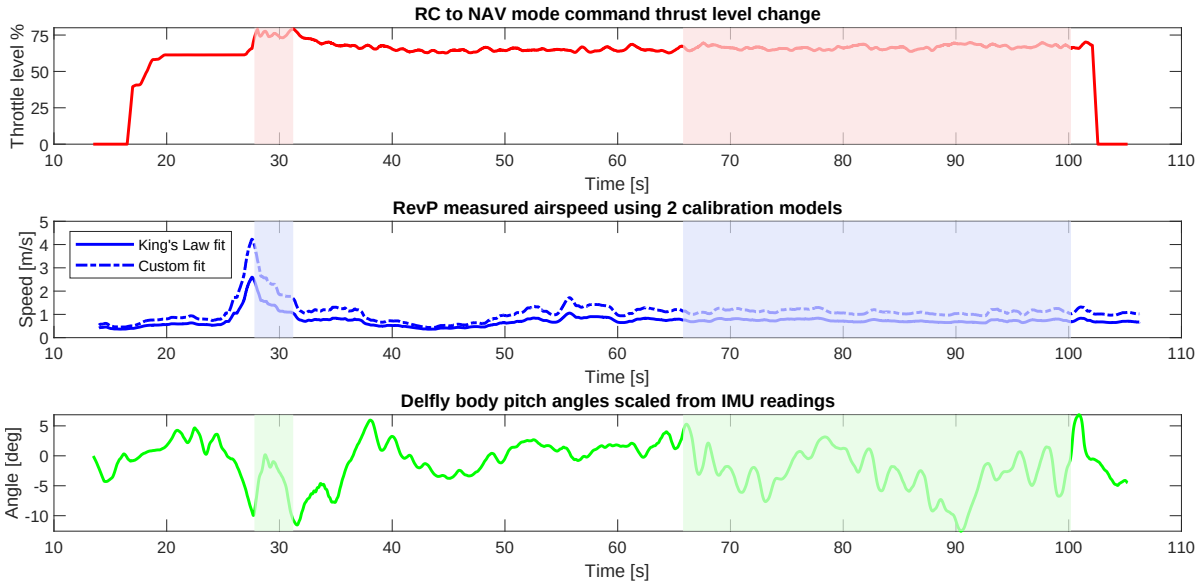

(a) Session 1

[*] https://wiki.paparazziuav.org/wiki/AutopilotModes
[†] https://wiki.paparazziuav.org/wiki/Rotorcraft_Configuration#Autopilot_modes
[‡] https://github.com/tudelft/mavlab/wiki/drone-delfly-nimble#flight-procedure

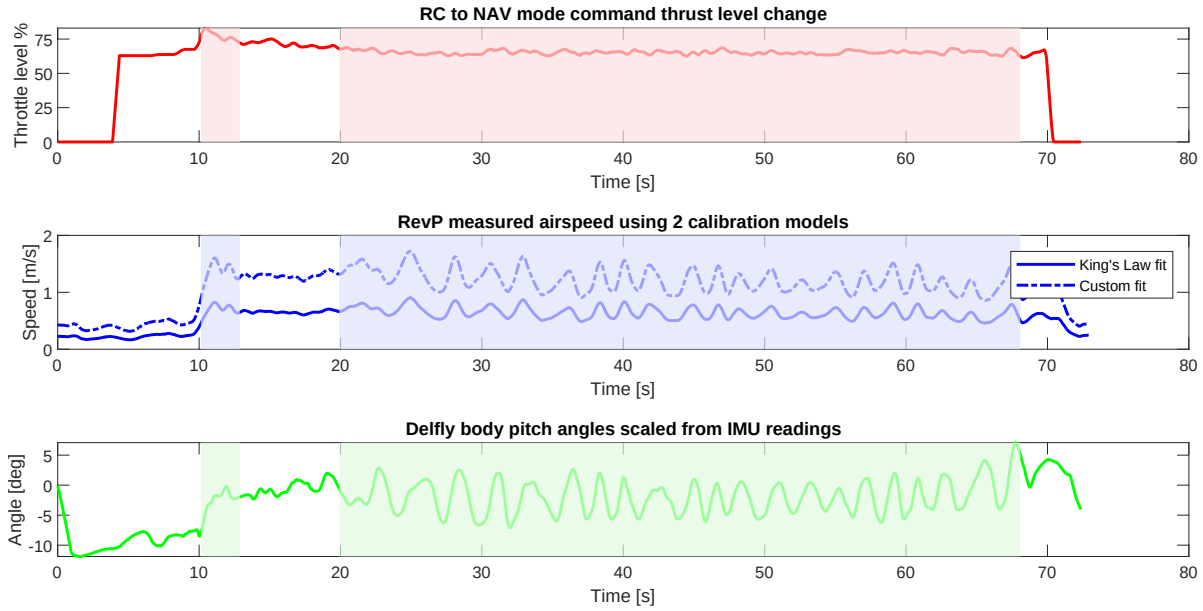

(b) Session 2

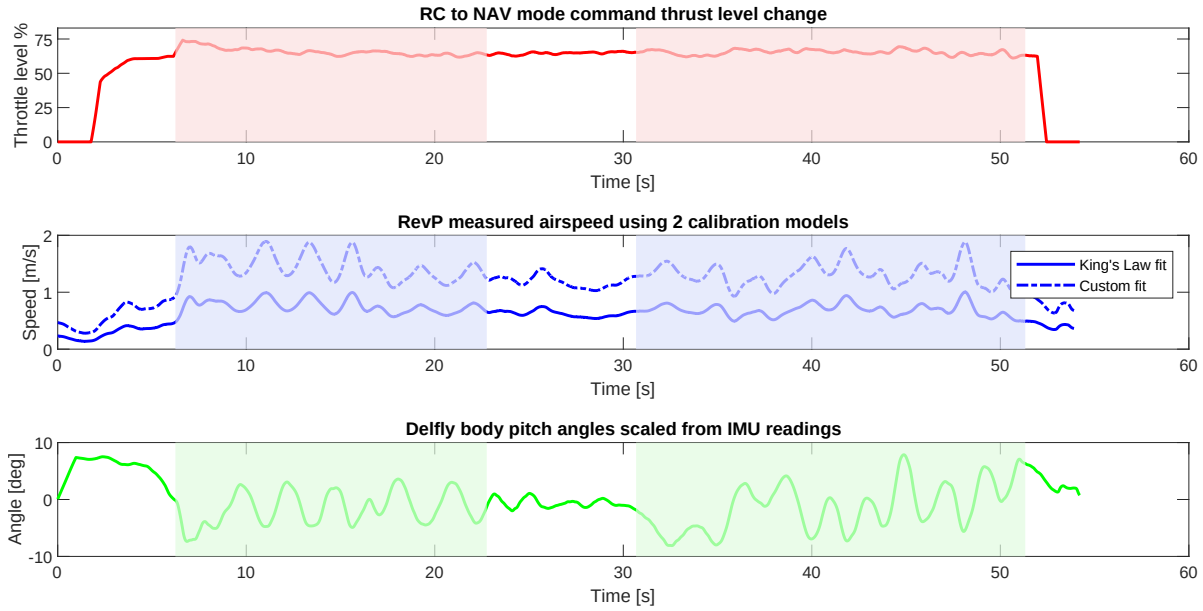

(c) Session 3

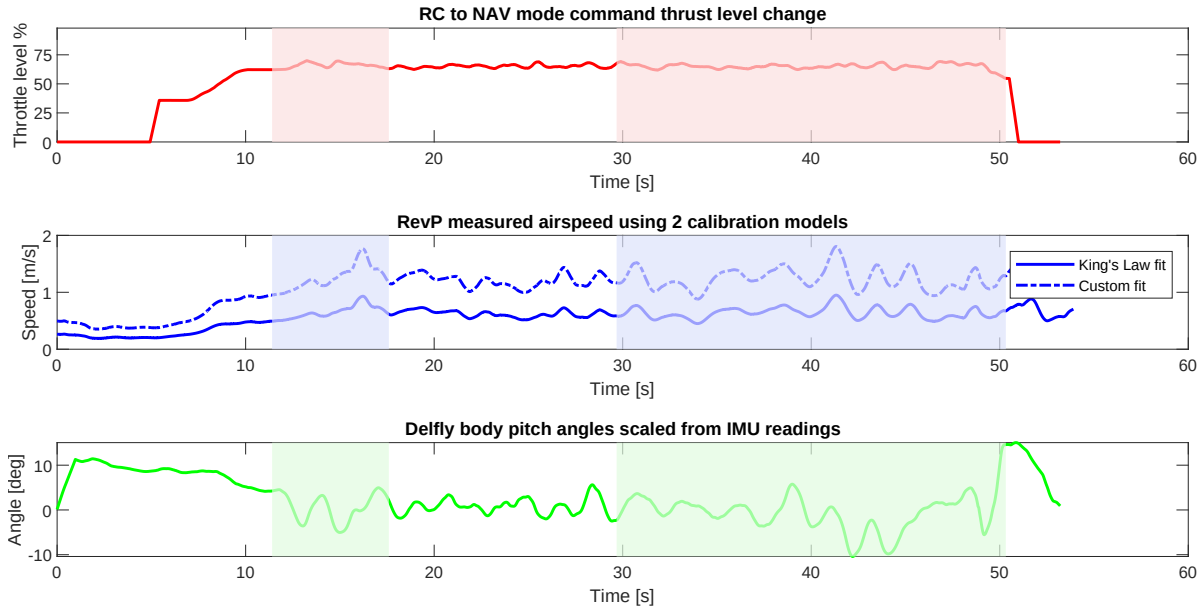

(d) Session 4

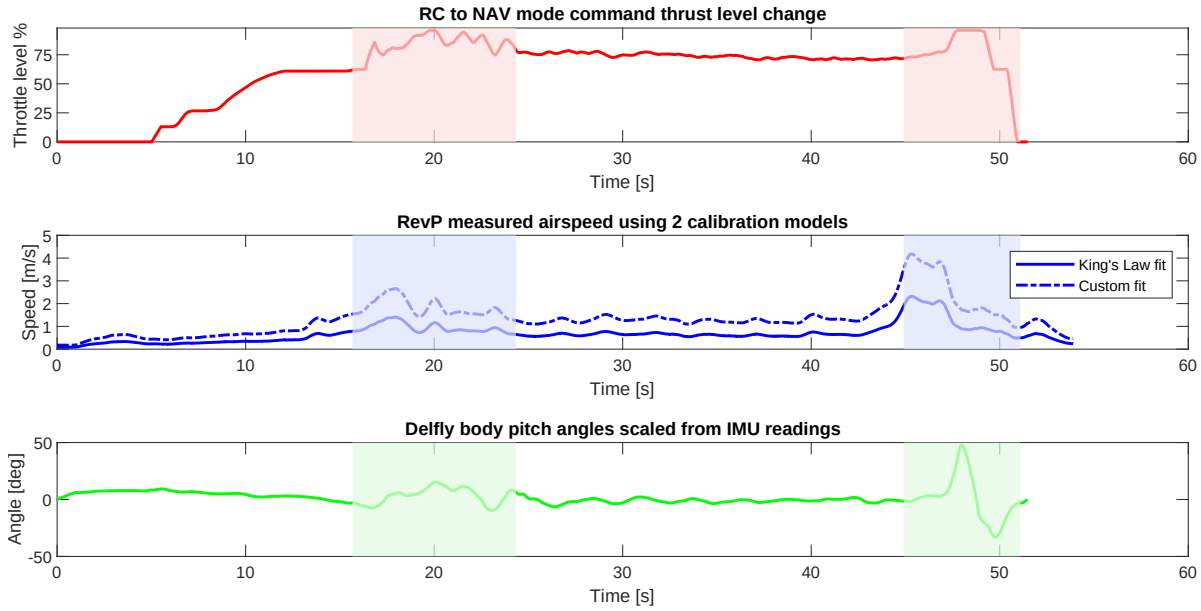

(e) Session 5

Figure 6.4: Five repeated hovering flight tests in the Cyberzoo with fixed waypoint specified in the flight plan of the Paparazzi autopilot

Note that although the procedure to achieve the stable hovering flight is the same, entering and maintaining the stable hovering flight takes slightly different amount of time at each test. This is caused by mostly two reasons. First, the tests are difficult to perform due to the external tethered cables. Hovering near the waypoint is more challenging. Second, as a self-made research product, the Delfly Nimble's mechanical and structural state changes slightly over time after an extensive amount of flapping each time. Among the repeated tests from Figure 6.4a to 6.4e, the time needed to enter each flight stage is different. Thus the flight segment of the stable hovering at Stage 3 has different time lengths.

The RevP sensor measurement results are corrected for with an offset of the mean value derived from the zero test with 15 RevP sensors as shown in Figure 6.5. This step is needed due to the slight COTS product difference and a new testing environment in Cyberzoo. Note that the RevP measurement results from using the Custom fit calibration model are consistently higher in Figure 6.4 compared to when using the King's Law calibration model. This is likely due to the slightly elevated temperature ($24°C$) in the testing environment compared to the W-tunnel calibration environment ($21°C$). And the custom fit model explicitly uses temperature in the calibration formula while King's Law does not. This indicates that further investigations into the temperature effects on the measurement accuracy are needed with the help of a more rigorously controlled temperature environment.

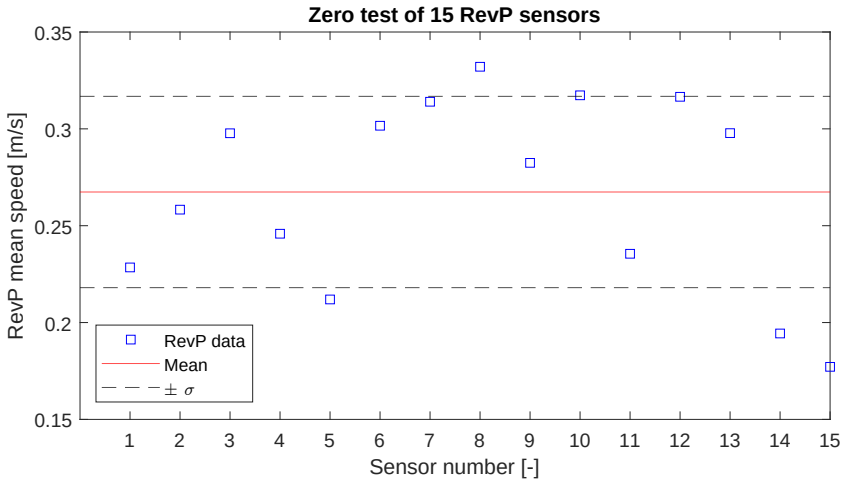

Figure 6.5: Zero test of 15 RevP sensors with no flow disturbances in the ambient, providing a reference value for offset

The mean body pitch angle and mean hovering throttle level during the stable hovering flight at Stage 3 for each repeated test is summarised in Table 6.3. Along with the corresponding mean speed from the RevP sensor measurements, they are plotted with the mounted test results from the W-tunnel for comparison in Figure 6.6. It can be seen that the Cyberzoo tethered hovering tests produces a flapping induced airflow speed approximately $0.1 \sim 0.15\ m/s$ larger than the W-tunnel mounted case. It would be extremely difficult to isolate the amount of influence from different factors at such a low speed regime. But this slight speed elevation could be mainly contributed to the increased throttle level needed for tethered hovering tests compared to the mounted ground tests, the more oscillatory body pitch angles, and the small temperature difference in the testing environment reducing the applicability of the previously obtained calibration coefficients.

Test repetition	Mean body pitch angle [deg]	Mean throttle level [%]
1	-1.42	65.86
2	-2.37	65.32
3	-0.74	65.09
4	0.62	65.43
5	-0.97	71.67

Table 6.3: Repeated tethered hover tests in Cyberzoo, with the mean body pitch angle and mean throttle level for the steady hovering stages (excluding the oscillating start and near-end stages)

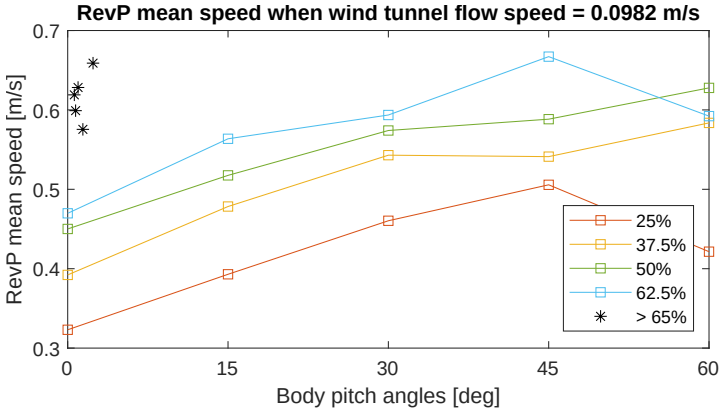

Figure 6.6: Results comparison of Cyberzoo tethered hover tests with W-tunnel mounted test (Note that absolute values of the body pitch angles are taken here)

6.2.1. Vibration analysis

To evaluate the influence of the add-on RevP airflow sensor on vibration energy level, the power spectral density (PSD) results from a free hovering flight and a tethered hovering flight with RevP sensor onboard are compared in Figure 6.7 and Figure 6.8 for the dominant Z direction. Both flights are performed in Navigation mode with the OptiTrack system's motion tracking. The 50 Hz cut-off frequency is also selected here to keep the first two harmonics on the frequency spectrum as the first two peaks are considered to be the most relevant for aerodynamic force production [13]. It can be seen that with the add-on RevP airflow sensor, the amount of mechanical vibration from flapping is higher as the PSD level is closer to the reference at the non-dimensionlised amplitude of 10^0 in Figure 6.7 and Figure 6.8. There is also an approximately 1 Hz elevation in the dominant frequency. With the add-on weight from the RevP sensor, a higher throttle level is needed to maintain a stable hovering flight, leading to higher vibration energy level.

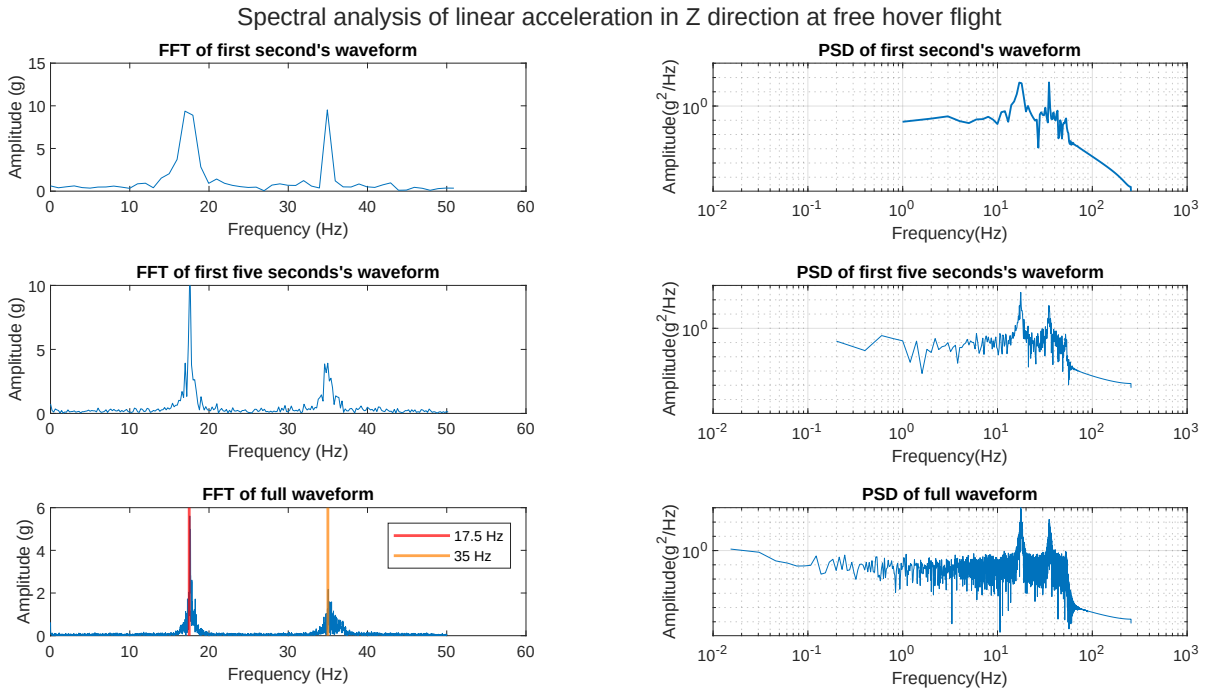

Figure 6.7: Vibration analysis: Delfly free hovering flight, without RevP sensor onboard, average hovering throttle level at 61.88%

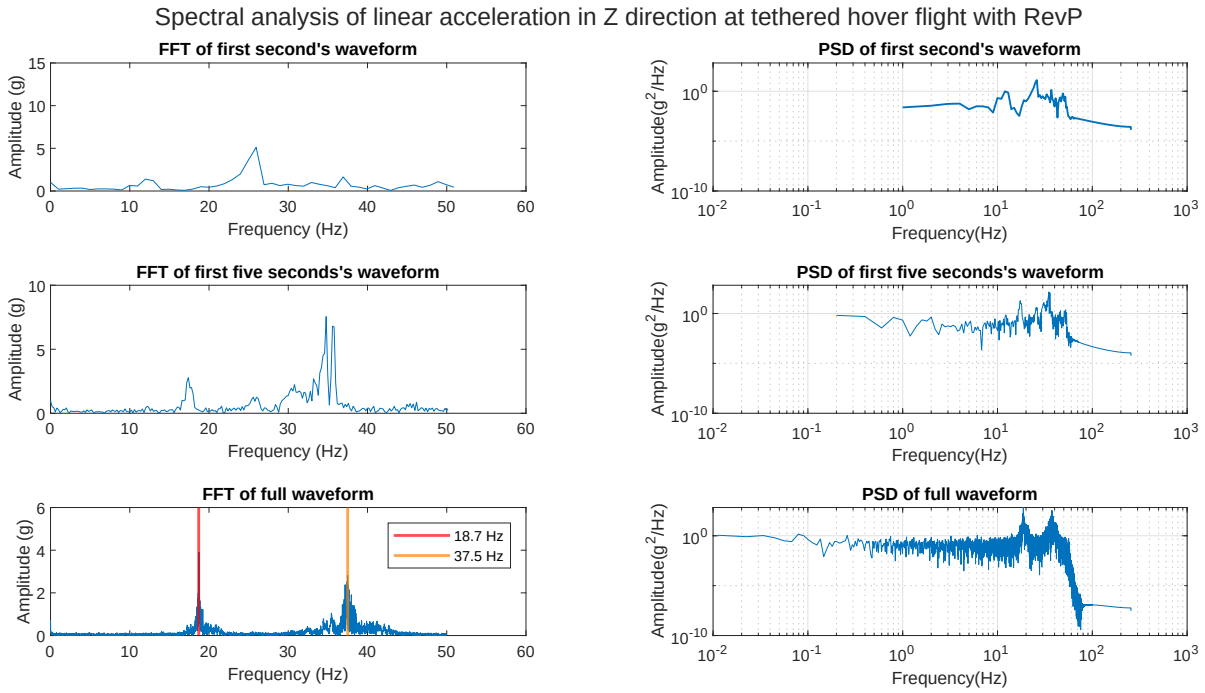

Figure 6.8: Vibration analysis: Delfly tethered hovering flight, with RevP sensor onboard, average hovering throttle level at 63.89%

In Figure 6.9, OptiTrack regulated throttle level peaks at 79 % during the initial stabilisation stage and then stabilize around 65 %. Thus the closest W-tunnel reference data that can be used for comparison is with throttle level at approximately 62.5 %. It can be seen that once in the tethered hovering flight conditions, with the slight increase in throttle level and flapping frequency, along with the added protection ribbon and RevP sensor cabling trailing and swirling at the bottom of the Delfly,

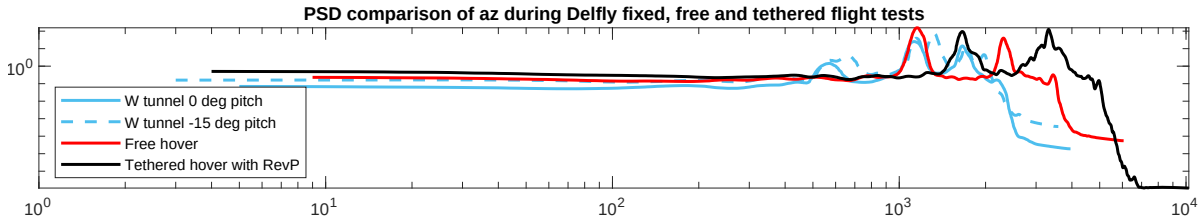

Figure 6.9: PSD from Cyberzoo hovering tests compared with mounted Delfly tests in W-tunnel

the vibration energy level is higher than mounted Delfly tests despite the majority of the RevP sensor weight is being brought closer to the drone's center of gravity. This increased vibration amplitude would result in slight increase in relative motion of the RevP sensing element resulting in larger measured speed. This effect can be observed qualitatively but difficult to quantify without repeatable controlled flight tests under different vibration levels.

7

Conclusion and future work

7.1. Conclusions

In this thesis project, the main research question of whether low speed airflow sensing on a flapping wing MAV is possible with an airflow sensor from the currently available commercial products. The flow measurement challenge lies in the distinction between measurement noise caused by relative motion from flapping and the true airflow disturbance from the ambient environment at very low speeds. Two potentially suitable sensors RevC and RevP from the company Modern Device are selected to be further characterised in terms of their measurement performance.

The major experiment results to answer the main research question and sub-questions are presented as follows.

Both the RevC and RevP airflow sensors can be easily calibrated with the help of a wind tunnel and an air velocity calibrator that is capable of generating extremely low flow speeds close to 0 m/s. Two models are used for the sensor calibration. Both King's Law and the custom fit function with temperature feedback can be used to obtain calibration coefficients for the RevP sensor. For the RevC sensor, the custom fit model is not applicable as the analog temperature feedback from the sensor displays highly non-linear relationship with the reference ambient temperature. RevP sensor does not have this issue as it has an onboard temperature sensor integrated into the circuitry. This indicates that to calibrate the RevC sensor with more accurate temperature feedback, a test environment with strict temperature control is needed. This temperature-controlled environment could also help calibrate the airflow sensors at various temperatures. Otherwise, with the currently available calibration coefficients, the larger the testing environment deviates from 21 $^{\circ}C$, the more measurement inaccuracies would occur due to the temperature effects from hot-wire like methods. This is crucial for applications at low speed ranges.

The minimum detectable flow by both airflow sensors is down to the magnitude of 0.05 m/s, although that poses a challenge to actually generate such a flow speed accurately. But the sensors are sensitive enough to reflect flow speed changes of such a magnitude. The actual sampling speed depends on the choice of the analog-to-digital (ADC) converters used for data acquisition.

Under laminar flow regime in the W-tunnel, both RevC and RevP have comparable measurement in turbulence intensity compared to a constant temperature hot-wire anemometer, all at the 0.5 % order of magnitude. When the turbulence level of the freestream is increased with an add-on grid, both sensors are sufficiently sensitive in terms of frequency response under the influence of turbulence, but when compared to the hot-wire anemometer, they are less sensitive in terms of capturing higher order fluctuations larger than 2 %. This is mostly caused due to the limitations in the sensor electronics and circuitry design.

The final key performance parameter is the directional sensitivity of both airflow sensors. RevP is less directionally dependent compared to RevC and can perform reliably for an angle variation

between $-30 \sim 30$ degrees in all rotational degrees of freedom, with the yaw degree of freedom least sensitive to incoming flow direction, and the roll degree of freedom the most sensitive. The measurement repeatability of the RevP sensor is also better than the RevC sensor when repeating the rotational test three times with three RevP or RevC sensors.

To aim for better performance and measurement accuracy, despite a higher supply voltage needed from an external source, RevP is still chosen as the airflow sensor being tested onboard Delfly Nimble in the W-tunnel. The three influence factors (throttle level, body pitch angle and ambient flow speed) are varied to examine the RevP sensor's measurement capability under different aerodynamic and control conditions. Once the flapping-induced influence on the RevP measurement due to the relative sensor movement is removed, RevP is capable of measuring ambient flow speed with a 10-20% deviation until the directional sensitivity comes into play for large pitch angles. Within $\pm$ 15 degrees of body pitch angles, the RevP sensor can measure well the actual ambient flow speeds in the W-tunnel.

The flapping-induced influence is later validated through five repeated tethered hovering flight tests in Cyberzoo for the case without any ambient wind disturbance. Due to practical implementation considerations, the RevP is mounted at the top of the Delfly body fuselage aligned with the pitch forward direction of the drone. The sensor is cut such that the main PCB board is mounted near the center of gravity to reduce the influence of flapping-related vibrations on the measurement results given the tethered flights already have higher amount of vibration energy compared to mounted tests in wind tunnels. The averaged results show a slight increase at 0.1 m/s order of magnitude in RevP measured speeds near the hovering position. This slight increase attributes mostly to the elevated throttle level needed for a tethered hovering flight causing more mechanical vibration, which leads to a larger relative motion of the RevP sensor during its measurement. Overall, at such a low speed measurement, this relatively close agreement between the wind tunnel tests and flight tests in terms of flapping-induced influence shows promising application aspects for future tests.

To further verify how the changes in body pitch angle and ambient flow speed would affect the RevP's measurement accuracy in a (tethered) free flight scenario and compare with the mounted test datasets from the wind tunnel, a solution has to be found to remove the airflow sensor's dependence on external power supply, such as through sensor redesign for smaller size and power consumption. Otherwise, the length limitation of the external cables needed for the RevP sensor power and data acquisition would restrict the forward flight distance. And last, a reliable wind generating system is needed to create various ambient flow speeds during free flight tests.

7.2. Future work

To further expand the application potential of the thermistor-based airflow sensor, the following work could be done.

7.2.1. Sensor redesign for free flight FWMAV applications

As seen in this thesis project, the high power consumption of the RevP sensor and the lack of reliable temperature measurement of the RevC sensor with more directional dependence prevents them from being further used on a flapping wing MAV. Redesign work of the airflow sensor could be carried out to further reduce the sensor size, power consumption and weight while maintaining the onboard ambient temperature compensation. With the current 12 V voltage supply of RevP, there is sufficient power to heat up the sensing thermistor to be able to sense hurricane force winds without the measurement data saturating. However, such a wide range of measure-able wind speeds is not needed for flapping wing MAV applications due to the gentle nature of its operating environment. Utilizing the sensor's high measurement sensitivity at low to medium wind speeds would be sufficient already. Thus, a different selection of thermistors without sacrificing the measurement accuracy while using a lower power supply would be the ultimate goal of sensor redesign. Since

all things in engineering come at certain prices, the balance of power consumption, measurement accuracy, size and weight for implementation on a flapping wing MAV would have to be weighed.

The following redesign specifications are suggested:

- Reduce unnecessary pin holes and redundant PCB space
- Keep the ambient temperature compensation module from Rev.P (Model S1-MCP9701SOT-23 from MICROCHIP [52])
- Investigate on the choice of thermistors to enable lower power supply need, ideally 5V or even 3.3 V which would be compatible with Delfly Nimble's regulated 3.3 V output. If the wind sensor needs 5 V or more, then a step-up voltage regulator would be needed if supplied with the Delfly Nimble battery
- Adjust accordingly the unity gain op-amp "buffer" and voltage output scaling up/down depending on the selection of thermistor and needed power supply

Once an improved version of the thermistor-based airflow sensor is available, it will also be possible to further evaluate how the sensor's performance changes overtime in terms of measurement sensitivity, power consumption etc. A more mature airflow sensing solution would become available for MAVs with extremely limited power supply and payload.

7.2.2. Incoming flow disturbance direction identification

As each individual airflow sensor's directional sensitivity is investigated fully in this thesis project, utilising this information with more than one airflow sensor could provide extra information on the incoming flow disturbance direction. This shall allow future applications for MAVs that can carry more than one airflow sensor. To realise this on a flapping wing MAV, it would put a tighter restriction on the sensor redesign work to reduce its weight primarily. Previous work done by Widyantara et al. [96] provide a three-sensor setup shown in Figure 7.1 that further demonstrated the different measurement responses to incoming winds of different directions, when the sensors are placed at a 60-degree angle with respect to each other. In Figure 7.3, Sadeghi et al. [75] present some innovative spacing patterns to arrange for the positions of multiple airflow sensing elements that would provide rich flow directional information. This could inspire future design of the sensing fingers on the RevP airflow sensor.

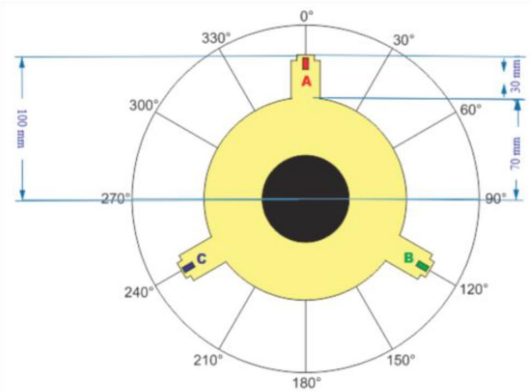

Figure 7.1: The schematic layout of three Rev.P wind sensors placed 120° with respect to each other [96]

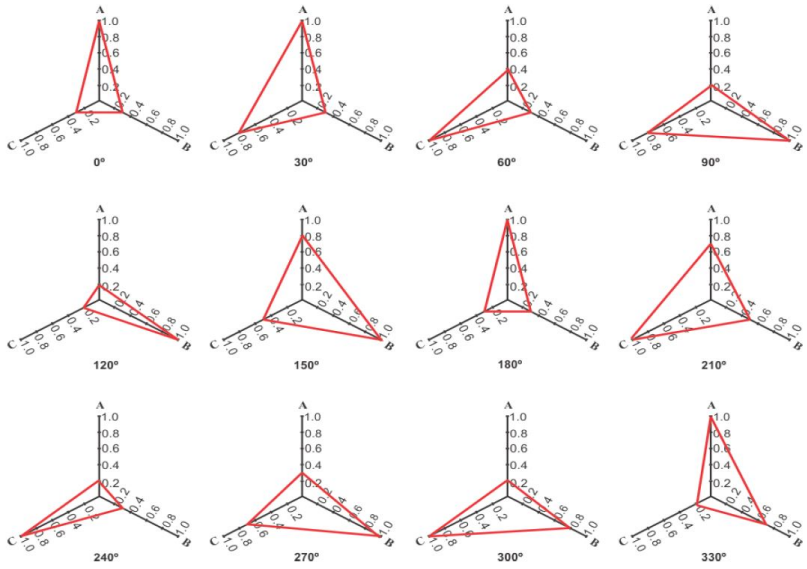

Figure 7.2: The normalized response pattern of the array of three sensors influenced by airflow coming from different directions ([96], p481)

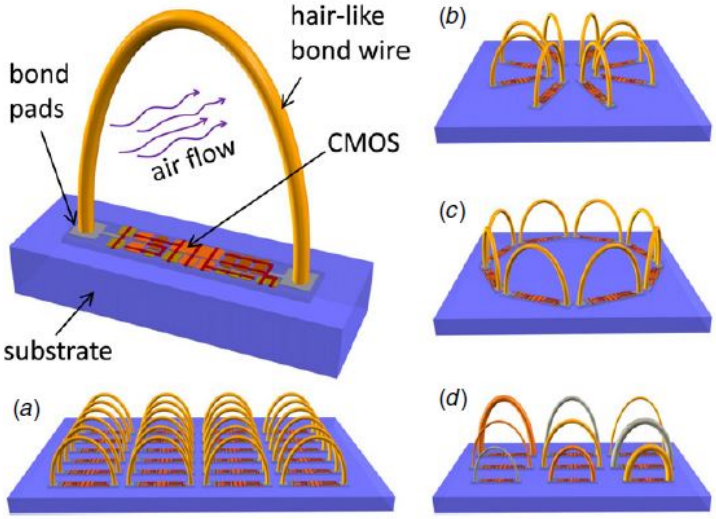

Figure 7.3: Schematic drawings of different configurations of a hot-wire hair-like thermal air flow sensor with integrated CMOS circuitry for transduction and/or onboard processing. Different configurations: (a) Dense array (b) Star-like (c) Circular (d) Sensors with different heights, wire gauges or materials [75]

7.2.3. Integration to MAV existing sensory network

Numerous work has been done to identify to what extent the stability of animal flight is inherent and the augmentation role of the creature's sensory systems. When studying the role of sensory systems in animals and insects, such as vision, airflow sensing and inertial movement sensing, passive experimental methods of breaking the feedback loops by the temporary "deactivation" of the sensory systems would disturb the animal's behaviour and welfare potentially [37]. Thus, common practice is through numerical methods. As the design of MAVs and small electronics continuously evolve, more options become possible. With the availability of a fully programmable and controllable flapping wing MAV such as Delfly Nimble, flight control stability with or without airflow

sensing in response to incoming flow disturbance could be further explored to identify an optimal control strategy and compare with how flyers in nature deal with wind disturbances. The airflow sensing capability onboard the flapping wing MAV is a crucial preparatory step in this development process, which could aid wind velocity estimation along with other components of the drone's onboard sensory modules.

A

The mobile wind generator

The author spent about 70 hours over the course of 3 months during the thesis helping assemble a self-designed (by TU Delft MAVLab PhD candidate Diana Olejnik) mobile wind generator system in Cyberzoo that is aimed to shorten the logistical preparation time for drone testing involving flow disturbance under approximately 3.5 m/s.

The whole assembly consists of 15 fan modules (each module contains 9 identical computer fans) and a self-contained electrical wiring set-up for power supply and signal feedback in the cabinet underneath the fan modules. The volume of the fan modules spans $1262mm \times 220mm \times 758mm$ in length, width and height. More design details of the whole system will be revealed later by its designer Diana Olejnik.

A grid with 15 RevP airflow sensors has been constructed by the author to characterise the uniformity of the entire flow field as illustrated in Figure A.1.

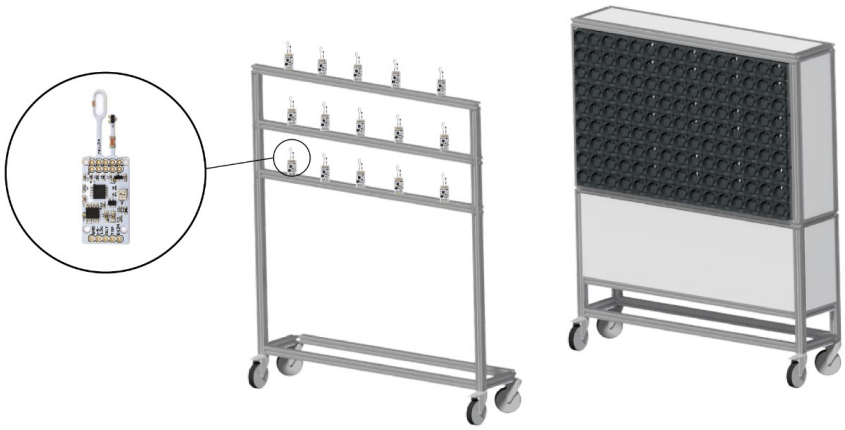

Figure A.1: Sensor grid with 15 RevP sensors for fan system flow field mapping

As a future continuation of using the RevP sensors based on the groundwork laid in this thesis, the following metrics will be obtained through flow tests at different fan settings and at different downstream locations to evaluate how the flow uniformity and velocity fluctuations change:

- The mapping between fan duty cycles and flow speeds at different downstream distances

- The turbulence intensity at different fan duty cycles
- the turbulence intensity at different downstream distances

The original design goal of this mobile wind generator is to provide small flow disturbance ($U_\infty < 4 m/s$) for flapping wing MAV tests, as flapping wing MAVs can sustain much less flow disturbance compared to other types of MAVs given the smaller size, mass and power. With the option of airflow sensing onboard a flapping wing MAV, this ready-to-use system provides future experiment possibilities of improving a flapping wing MAV's performance under various types and intensities of wind gusts.

B

PID tuning for hovering flight

1. Set the gains in the horizontal guidance loop to zero before the start of a hovering flight
2. Start hovering Delfly Nimble in RC manual mode with a DEVO 10 RC Transmitter while holding the protection ribbon. Hover to the pre-set waypoint as close as possible and switch on the OptiTrack guidance mode through the transmitter. Delfly Nimble at this state is highly unstable and prone to crash. In the PaparazziUAV software ground control interface, increase the P_{gain} until Nimble is in a steady oscillation mode
3. Increase the D_{gain} until the oscillations are as close to a critical damped stage as possible. Full oscillation removal is unlikely given the body vibration and external disturbance.
4. Repeat Step 2 and Step 3 until increasing the D_{gain} does not have further improvements on reducing oscillations.
5. So far, the P_{gain} and D_{gain} values are set temporarily through WiFi communication. Implement them in the airframe file to be permanent for the current test set-up. It is highly possible as time goes on, the flapping wing MAV's performance degrades or the payload onboard is changed, then the gain values have to be re-tuned.

C

Cable length determination for tethered hovering test

To examine how the length of the signal and power supply cable affects power input and measurement outputs, the sample standard deviation shown in Equation C.1 is used here as a measure of variability in signal outputs since the distribution of the signals appear to approach a normal distribution as the sample points keep increasing.

$$\sigma = \sqrt{\frac{\sum_{i=1}^{N} \left(E_i - \bar{E}\right)^2}{N-1}} \tag{C.1}$$

Figure C.1a visualises the higher noisiness of the raw analog voltage signals from the longest investigated cable, where the standard deviation is further calculated in Table C.1. This shows the increase in cable length leads to more noisiness in measurement results. The signal-to-noise ratio shown in Table C.2 also confirms this. The cable length $1.5m$ also has a more significant analog voltage output drop compared to other lengths as shown in Figure C.1b, especially for the raw airflow signal output. The temperature analog output is less affected. However, any shorter cable length will bring difficulty to the actual hovering flight tests and forcing the Delfly to hover at a height where ground effects will be more prominent, although it would be interesting to measure under the influence of ground effects for potential applications such as more stable landing [29]. To summarize, the $1.5m$ cable length is chosen at the cost of slightly higher noise level but brings the benefit of easier tethered hovering flight.

Standard deviation	0.5 [m]	1.5 [m]
Raw airflow analog voltage	0.2362 %	0.2755 %
Raw temperature analog voltage	0.3753 %	0.4048 %

Table C.1: Standard deviation comparison of cable length at 0.5 m and 1.5 m

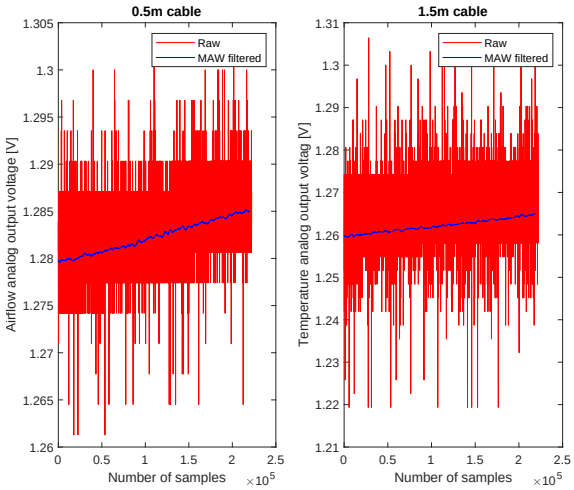

(a) Raw and moving average window filter(MAW) filtered RevP sensor analog outputs

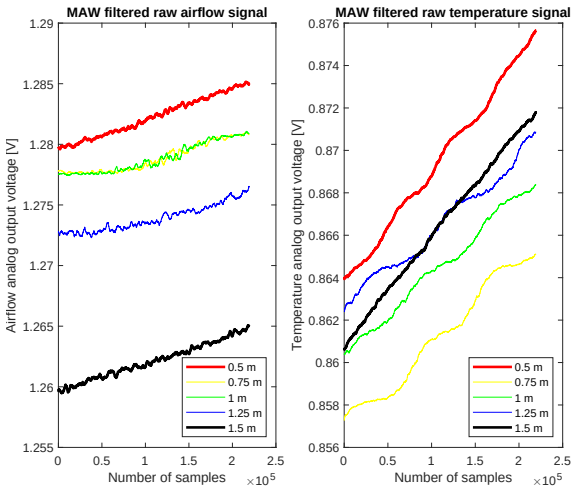

(b) Filtered analog signals from different cable lengths

Figure C.1: The cable length's influence on analog voltage outputs

SNR(dB)	**0.5 [m]**		**1.5 [m]**	
	Before	After	Before	After
Airflow analog voltage	-11.77	0.44	-16.17	-3.83
Temperature analog voltage	-4.33	-1.62	-9.52	-3.47

Table C.2: Signal-to-noise ratio comparison

Bibliography

[1] Lisa/mxs v1.0. URL https://wiki.paparazziuav.org/wiki/Lisa/MXS_v1.0.

[2] Paparazzi uav (unmanned aerial vehicle) wikipedia. URL https://wiki.paparazziuav.org/wiki/Main_Page.

[3] *Design, Fabrication and Testing of a Bioinspired Hybrid Hair-Like Fluid Motion Sensor Array*, volume Volume 8: Heat Transfer, Fluid Flows, and Thermal Systems, Parts A and B of *ASME International Mechanical Engineering Congress and Exposition*, 11 2007. doi: 10.1115/IMECE2007-43006. URL https://doi.org/10.1115/IMECE2007-43006.

[4] Dynamics and flight control of a flappingwing robotic insect in the presence of wind gusts. *Interface Focus*, 7(1), 2017. ISSN 20428901. doi: 10.1098/rsfs.2016.0080.

[5] F. Scarano A. Sciacchitato. *Flow Measurement Techniques Student Manual for the Laboratory Exercise*. Delft University of Technology Aerospace Engineering Department Aerodynamics Section, Mar 2019.

[6] A.R. Aiyar, C. Song, S.H. Kim, and M.G. Allen. An all polymer air-flow sensor array using a piezoresistive composite elastomer. In *2009 IEEE 22nd International Conference on Micro Electro Mechanical Systems*, pages 447–450, 2009. doi: 10.1109/MEMSYS.2009.4805415.

[7] Ahmed Alfadhel, Mohammed Asadullah Khan, Susana Cardoso, Diana Leitao, and Jürgen Kosel. A magnetoresistive tactile sensor for harsh environment applications. *Sensors*, 16(5), 2016. ISSN 1424-8220. doi: 10.3390/s16050650. URL https://www.mdpi.com/1424-8220/16/5/650.

[8] Sophie Armanini. *Identification of time-varying models for flapping-wing micro aerial vehicles*. PhD thesis, Delft University of Technology, 2018.

[9] Karan Bains. System identification of the delfly nimble. Master's thesis, Delft University of Technology, dec 2020.

[10] R. E. Brown and M. R. Fedde. AIRFLOW SENSORS IN THE AVIAN WING. *Journal of Experimental Biology*, 179(1):13–30, 06 1993. ISSN 0022-0949. doi: 10.1242/jeb.179.1.13. URL https://doi.org/10.1242/jeb.179.1.13.

[11] H H Bruun. Hot-wire anemometry: Principles and signal analysis. *Measurement Science and Technology*, 7(10), oct 1996. doi: 10.1088/0957-0233/7/10/024. URL https://doi.org/10.1088/0957-0233/7/10/024.

[12] C P Byers, M K Fu, Y Fan, and M Hultmark. Development of instrumentation for measurements of two components of velocity with a single sensing element. *Measurement Science and Technology*, 29(2):025304, jan 2018. doi: 10.1088/1361-6501/aa99c1. URL https://doi.org/10.1088/1361-6501/aa99c1.

[13] J V Caetano, M Percin, B W van Oudheusden, B Remes, C de Wagter, G C H E de Croon, and C C de Visser. Error analysis and assessment of unsteady forces acting on a flapping wing micro air

vehicle: free flight versus wind-tunnel experimental methods. *Bioinspiration & Biomimetics*, 10(5):056004, aug 2015. doi: 10.1088/1748-3190/10/5/056004. URL https://doi.org/10.1088/1748-3190/10/5/056004.

[14] Jack Chen, Zhifang Fan, J. Zou, J. Engel, and Change Liu. Two-dimensional micromachined flow sensor array for fluid mechanics studies. *Journal of Aerospace Engineering*, 16:85–97, 2003.

[15] Nannan Chen, Craig Tucker, Jonathan M. Engel, Yingchen Yang, Saunvit Pandya, and Chang Liu. Design and characterization of artificial haircell sensor for flow sensing with ultrahigh velocity and angular sensitivity. *Journal of Microelectromechanical Systems*, 16(5):999–1014, 2007. doi: 10.1109/JMEMS.2007.902436.

[16] Jorn A. Cheney, Jonathan P. J. Stevenson, Nicholas E. Durston, Jialei Song, James R. Usherwood, Richard J. Bomphrey, and Shane P. Windsor. Bird wings act as a suspension system that rejects gusts. *Proceedings of the Royal Society B: Biological Sciences*, 287(1937):20201748, 2020. doi: 10.1098/rspb.2020.1748. URL https://royalsocietypublishing.org/doi/abs/10.1098/rspb.2020.1748.

[17] Sheryl Coombs. Smart skins: Information processing by the lateral line system. *Autonomous Robots*, 11(3):255–261, Nov 2001. doi: https://doi.org/10.1023/A:1012491007495.

[18] P. O. A. L. Davies, M. J. Fisher, and Albert Alan Townsend. Heat transfer from electrically heated cylinders. *Proceedings of the Royal Society of London. Series A. Mathematical and Physical Sciences*, 280(1383):486–527, 1964. doi: 10.1098/rspa.1964.0159. URL https://royalsocietypublishing.org/doi/abs/10.1098/rspa.1964.0159.

[19] M. Dijkstra, M.J. de Boer, J.W. Berenschot, T.S.J. Lammerink, R.J. Wiegerink, and M. Elwenspoek. Miniaturized thermal flow sensor with planar-integrated sensor structures on semicircular surface channels. *Sensors and Actuators A: Physical*, 143(1):1–6, 2008. ISSN 0924-4247. doi: https://doi.org/10.1016/j.sna.2007.12.005. URL https://www.sciencedirect.com/science/article/pii/S0924424707008928. Micromechanics Section of Sensors and Actuators (SAMM), based on contributions revised from the Technical Digest of the IEEE 20th International Conference on Micro Electro Mechanical Systems (MEMS 2007).

[20] Marcel Dijkstra, J. V. Baar, R. Wiegerink, T. Lammerink, J. D. Boer, and G. Krijnen. Artificial sensory hairs based on the flow sensitive receptor hairs of crickets. *Journal of Micromechanics and Microengineering*, 15, 2005.

[21] Charles P. Ellington, Coen Van Den Berg, Alexander P. Willmott, and Adrian L. R. Thomas. Leading-edge vortices in insect flight. *Nature*, 384(6610):626–630, 1996. doi: 10.1038/384626a0.

[22] I. Elmi, S. Zampolli, E. Cozzani, F. Mancarella, and G.C. Cardinali. Development of ultra-low-power consumption mox sensors with ppb-level voc detection capabilities for emerging applications. *Sensors and Actuators B: Chemical*, 135(1):342–351, 2008. ISSN 0925-4005. doi: https://doi.org/10.1016/j.snb.2008.09.002. URL https://www.sciencedirect.com/science/article/pii/S0925400508005935.

[23] Dewei Fan, Cheng Xiaoqi, Chi Wai Wong, and Jun-De Li. Optimization and determination of the frequency response of constant-temperature hot-wire anemometers. *AIAA Journal*, 55(8):2537–2543, 2017. doi: 10.2514/1.J055801. URL https://doi.org/10.2514/1.J055801.

[24] Zhifang Fan, Jack Chen, Jun Zou, David Bullen, Chang Liu, and Fred Delcomyn. Design and fabrication of artificial lateral line flow sensors. *Journal of Micromechanics and Microengineering*, 12(5):655–661, jun 2002. doi: 10.1088/0960-1317/12/5/322. URL https://doi.org/10.1088/0960-1317/12/5/322.

[25] Joel H. Ferziger, Milovan Perić, and Robert L. Street. *Computational methods for fluid dynamics*. Springer, 2020.

[26] Peter Freymuth. Hot-wire anemometer thermal calibration errors. *Instr. and Contr. Systems*, 43:82–83, 1970.

[27] M K Fu, Y Fan, C P Byers, T-H Chen, C B Arnold, and M Hultmark. Elastic filament velocimetry (EFV). *Measurement Science and Technology*, 28(2):025301, dec 2016. doi: 10.1088/1361-6501/28/2/025301. URL https://doi.org/10.1088/1361-6501/28/2/025301.

[28] Werner Gnatzy and Jürgen Tautz. Ultrastructure and mechanical properties of an insect mechanoreceptor: Stimulus-transmitting structures and sensory apparatus of the cereal filiform hairs of gryllus. *Cell and Tissue Research*, 213(3), 1980. doi: 10.1007/bf00237890.

[29] Samuel Dutra Gollob, Yash Manian, Ryan St. Pierre, Abraham Simpson Chen, and Sarah Bergbreiter. A lightweight, compliant, contact-resistance-based airflow sensor for quadcopter ground effect sensing. In *2018 IEEE International Conference on Robotics and Automation (ICRA)*, pages 7826–7831, 2018. doi: 10.1109/ICRA.2018.8461229.

[30] Zhiwu Han, Linpeng Liu, Kejun Wang, Song Honglie, Chen Daobing, Ze Wang, Shichao Niu, Junqiu Zhang, and Luquan Ren. Artificial hair-like sensors inspired from nature: A review. *Journal of Bionic Engineering*, 15:409–434, 05 2018. doi: 10.1007/s42235-018-0033-9.

[31] Hendrik Herzog, Adrian Klein, Horst Bleckmann, Peter Holik, Sam Schmitz, Georg Siebke, Simon Tätzner, Manfred Lacher, and Siegfried Steltenkamp. μ-biomimetic flow-sensors–introducing light-guiding pdms structures into mems. *Bioinspiration & biomimetics*, 10: 036001, 06 2015. doi: 10.1088/1748-3190/10/3/036001.

[32] Albert J., Friedrich O., Dechant H.-E., and Barth F. Arthropod touch reception: spider hair sensilla as rapid touch detectors. *Journal of Comparative Physiology A: Sensory, Neural, and Behavioral Physiology*, 187(4):303–312, 2001. doi: 10.1007/s003590100202.

[33] Diana E. Jaalouk and Jan Lammerding. Mechanotransduction gone awry. *Nature Reviews Molecular Cell Biology*, 10(1):63–73, 2009. doi: 10.1038/nrm2597.

[34] Yonggang Jiang, Peng Zhao, Zhiqiang Ma, Dawei Shen, Gongchao Liu, and Deyuan Zhang. Enhanced flow sensing with interfacial microstructures. *Biosurface and Biotribology*, 6(1): 12–19, 2020. doi: https://doi.org/10.1049/bsbt.2019.0043. URL https://ietresearch.onlinelibrary.wiley.com/doi/abs/10.1049/bsbt.2019.0043.

[35] Finn E. Jørgensen. *How to measure turbulence with hot-wire anemometers-a practical guide*. Dantec Dynamics, 2002.

[36] Matej Karasek, Florian T. Muijres, Christophe De Wagter, Bart D.W. Remes, and Guido C.H.E. De Croon. A tailless aerial robotic flapper reveals that flies use torque coupling in rapid banked turns. *Science*, 361(6407):1089–1094, 2018. ISSN 10959203. doi: 10.1126/science.aat0350.

[37] Matěj Karásek. *Robotic hummingbird: Design of a control mechanism for a hovering flapping wing micro air vehicle*. PhD thesis, École polytechnique de Bruxelles, nov 2014.

[38] Gadi Katzir, Edna Schechtman, Nurit Carmi, and Daniel Weihs. Head stabilization in herons. *Journal of comparative physiology. A, Sensory, neural, and behavioral physiology*, 187:423–32, 08 2001. doi: 10.1007/s003590100210.

[39] D. Khelif, S. P. Burns, and C. A. Friehe. Improved wind measurements on research aircraft. *Journal of Atmospheric and Oceanic Technology*, 16(7):860–875, 1999. doi: 10.1175/1520-0426(1999)016<0860:iwmora>2.0.co;2.

[40] A.M. Koppius and G.R.M. Trines. The dependence of hot-wire calibration on gas temperature at low reynolds numbers. *International Journal of Heat and Mass Transfer*, 19(9):967–974, 1976. ISSN 0017-9310. doi: https://doi.org/10.1016/0017-9310(76)90177-0. URL `https://www.sciencedirect.com/science/article/pii/0017931076901770`.

[41] Daniel Kress, Evelien van Bokhorst, and David Lentink. How lovebirds maneuver rapidly using super-fast head saccades and image feature stabilization. *PLOS ONE*, 10(6):1–24, 06 2015. doi: 10.1371/journal.pone.0129287. URL `https://doi.org/10.1371/journal.pone.0129287`.

[42] G. Kroetz, M. Eickhoff, and H. Moeller. Silicon compatible materials for harsh environment sensors. *Sensors and Actuators A-physical*, 74:182–189, 1999.

[43] J. Kuo, Lawrence Yu, and E. Meng. Micromachined thermal flow sensors - a review. *Micromachines*, 3:550–573, 2012.

[44] Horace Lamb. *Hydrodynamics*. Dover Publications, New York, 1932.

[45] C. Liu. Micromachined biomimetic artificial haircell sensors. *Bioinspiration & biomimetics*, 2 4:S162–9, 2007.

[46] Guijie Liu, Anyi Wang, Xinbao Wang, and Peng Liu. A review of artificial lateral line in sensor fabrication and bionic applications for robot fish. *Applied Bionics and Biomechanics*, 2016: 1–15, 2016. doi: 10.1155/2016/4732703.

[47] Huicong Liu, Songsong Zhang, R. Kathiresan, Takeshi Kobayashi, and Chengkuo Lee. Development of piezoelectric microcantilever flow sensor with wind-driven energy harvesting capability. *Applied Physics Letters*, 100:223905, 2012.

[48] Charles G. Lomas. *Fundamentals of Hot Wire Anemometry*. Cambridge University Press, 1986.

[49] Sadeghi M M, Peterson R L, Peterson K, Fearing R, and Najafi K. Air-flow sensing on autonomous mobile platforms using micro-scale hot-wire anemometry. *27th Army Science Conference*, 2010.

[50] Blanca Martinez Gallar. Flapping-wing aerodynamics study on the wake of DelFly II by means of Robotic Volumetric Particle Tracking Velocimetry. 2019.

[51] Mohd Norzaidi Mat Nawi, Asrulnizam Abd Manaf, and Mohd Rizal Arshad. Review of mems flow sensors based on artificial hair cell sensor. *Microsystem Technologies*, 17:1417–1426, 09 2011. doi: 10.1007/s00542-011-1330-y.

[52] MICROCHIP. Low-power linear active thermistor ics mcp9700/9700a mcp9701/9701a. Technical report, MICROCHIP TECHNOLOGY, 2016.

[53] A. Mohamed, R. Clothier, S. Watkins, R. Sabatini, and M. Abdulrahim. Fixed-wing MAV attitude stability in atmospheric turbulence, part 1: Suitability of conventional sensors. *Progress in Aerospace Sciences*, 70:69–82, 2014. ISSN 03760421. doi: 10.1016/j.paerosci.2014.06.001.

[54] A. Mohamed, S. Watkins, R. Clothier, M. Abdulrahim, K. Massey, and R. Sabatini. Fixed-wing MAV attitude stability in atmospheric turbulence - Part 2: Investigating biologically-inspired sensors. *Progress in Aerospace Sciences*, 71:1–13, 2014. ISSN 03760421. doi: 10.1016/j.paerosci.2014.06.002. URL http://dx.doi.org/10.1016/j.paerosci.2014.06.002.

[55] Abdulghani Mohamed, Mujahid Abdulrahim, Simon Watkins, and Reece Clothier. Development and flight testing of a turbulence mitigation system for micro air vehicles. *Journal of Field Robotics*, pages 1–22, 08 2015. doi: 10.1002/rob.21626.

[56] A. Molnár and D. Stojcsics. New approach of the navigation control of small size uavs. In *19th International Workshop on Robotics in Alpe-Adria-Danube Region (RAAD 2010)*, pages 125–129, 2010. doi: 10.1109/RAAD.2010.5524598.

[57] Tania Mukherjee and Tarun K. Bhattacharyya. A miniature, high sensitivity, surface micromachined displacement sensor with high resolution. In *2012 IEEE/ASME International Conference on Advanced Intelligent Mechatronics (AIM)*, pages 737–742, 2012. doi: 10.1109/AIM.2012.6265951.

[58] Nam-Trung Nguyen. Micromachined flow sensors—a review. *Flow Measurement and Instrumentation*, 8:7–16, 1997.

[59] Diana Olejnik, Aadithya Sujit, Matej Karásek, Bart Remes, and Guido de Croon. Wing sweeping mechanism for active control and stabilisation of a flapping wing mav. *10th International Micro-Air Vehicles Conference*, 2018.

[60] Diana A. Olejnik, Bardienus P. Duisterhof, Matej Karásek, Kirk Y. W. Scheper, Tom van Dijk, and Guido C. H. E. de Croon. A tailless flapping wing mav performing monocular visual servoing tasks. *Unmanned Systems*, 08(04):287–294, 2020. doi: 10.1142/S2301385020500235. URL https://doi.org/10.1142/S2301385020500235.

[61] B. W. Oudheusden. Silicon thermal flow sensors. *Sensors and Actuators A-physical*, 30:5–26, 1992.

[62] Y. Ozaki, T. Ohyama, T. Yasuda, and I. Shimoyama. An air flow sensor modeled on wind receptor hairs of insects. In *Proceedings IEEE Thirteenth Annual International Conference on Micro Electro Mechanical Systems (Cat. No.00CH36308)*, pages 531–536, 2000. doi: 10.1109/MEMSYS.2000.838573.

[63] Mustafa Percin, Jerke Eisma, Bas Van Oudheusden, Bart Remes, Rick Ruijsink, and Christophe De Wagter. *Flow Visualization in the Wake of the Flapping-Wing MAV 'DelFly II' in Forward Flight*. doi: 10.2514/6.2012-2664. URL https://arc.aiaa.org/doi/abs/10.2514/6.2012-2664.

[64] Ashley E. Pete, Daniel Kress, Marina A. Dimitrov, and David Lentink. The role of passive avian head stabilization in flapping flight. *Journal of The Royal Society Interface*, 12(110):20150508, 2015. doi: 10.1098/rsif.2015.0508. URL https://royalsocietypublishing.org/doi/abs/10.1098/rsif.2015.0508.

[65] D. Prohasky and S. Watkins. Low cost hot-element anemometry verses the TFI cobra. *Proceedings of the 19th Australasian Fluid Mechanics Conference, AFMC 2014*, (December), 2014.

[66] A.f.p. Van Putten and S. Middelhoek. Integrated silicon anemometer. *Electronics Letters*, 10 (21):425–426, 1974. doi: 10.1049/el:19740339.

[67] Daniel B. Quinn, Yous van Halder, and David Lentink. Adaptive control of turbulence intensity is accelerated by frugal flow sampling. *Journal of The Royal Society Interface*, 14(136): 20170621, 2017. doi: 10.1098/rsif.2017.0621. URL https://royalsocietypublishing.org/doi/abs/10.1098/rsif.2017.0621.

[68] Marshall P. Tulin Ralph D. Cooper. Turbulence measurements with the hot-wire anemometer. North Atlantic Treaty Organization Advisory Group for Aeronautical Research and Development, aug 1955.

[69] Badri N. Ranganathan, Ivan Penskiy, William Dean, Sarah Bergbreiter, and J. Sean Humbert. Bio-inspired wind frame state sensing and estimation for mav applications. In *2015 IEEE/RSJ International Conference on Intelligent Robots and Systems (IROS)*, pages 2729–2735, 2015. doi: 10.1109/IROS.2015.7353751.

[70] P. Roach. The generation of nearly isotropic turbulence by means of grids. *International Journal of Heat and Fluid Flow*, 8:82–92, 1987.

[71] D.Ronald Fannin Rodger Ziemer, William Tranter. *Signals and Systems: Continuous and Discrete*. Pearson, fourth edition, 2013.

[72] A. R. Rodi and D. C. Leon. Correction of static pressure on a research aircraft in accelerated flight using differential pressure measurements. *Atmospheric Measurement Techniques*, 5 (11):2569–2579, 2012. doi: 10.5194/amt-5-2569-2012. URL https://amt.copernicus.org/articles/5/2569/2012/.

[73] Andres Rodriguez, Evan Andersen, Justin Bradley, and Clark Taylor. *Wind Estimation Using an Optical Flow Sensor on a Miniature Air Vehicle*. doi: 10.2514/6.2007-6614. URL https://arc.aiaa.org/doi/abs/10.2514/6.2007-6614.

[74] Benoît Pinier Roger Lewandowski. The kolmogorov law of turbulence, what can rigorously be proved ? part ii the foundations of chaos revisited: from poincaré to recent advancements. *Springer*, pages 71–89, 2016.

[75] M M Sadeghi, R L Peterson, and K Najafi. Air flow sensing using micro-wire-bonded hair-like hot-wire anemometry. *Journal of Micromechanics and Microengineering*, 23(8):085017, 2013. doi: 10.1088/0960-1317/23/8/085017.

[76] Mahdi M. Sadeghi, Rebecca L. Peterson, and Khalil Najafi. Micro-hydraulic structure for high performance bio-mimetic air flow sensor arrays. In *2011 International Electron Devices Meeting*, pages 29.4.1–29.4.4, 2011. doi: 10.1109/IEDM.2011.6131638.

[77] T. Shimozawa, T. Kumagai, and Y. Baba. Structural scaling and functional design of the cercal wind-receptor hairs of cricket. *Journal of Comparative Physiology A: Sensory, Neural, and Behavioral Physiology*, 183(2):171–186, 1998. doi: 10.1007/s003590050245.

[78] Wei Shyy, Hikaru Aono, Chang-kwon Kang, and Hao Liu. *An Introduction to Flapping Wing Aerodynamics*. Cambridge Aerospace Series. Cambridge University Press, 2013. doi: 10.1017/CBO9781139583916.

[79] Keith A. Slinker, Corey Kondash, Benjamin T. Dickinson, and Jeffery W. Baur. Cnt-based artificial hair sensors for predictable boundary layer air flow sensing. *Advanced Materials Technologies*, 1(9):1600176, 2016. doi: https://doi.org/10.1002/admt.201600176. URL https://onlinelibrary.wiley.com/doi/abs/10.1002/admt.201600176.

[80] Elisabeth van der Sman, Ewoud Smeur, Bart Remes, Christophe De Wagter, and Qiping Chu. Incremental nonlinear dynamic inversion and multihole pressure probes for disturbance rejection control of fixed-wing micro air vehicles. In H. de Plinval J.-M. Moschetta G. Hattenberger, editor, *International Micro Air Vehicle Conference and Flight Competition 2017*, pages 111–120, September 2017. URL http://www.imav2017.org/,http://www.imavs.org/2017/. null ; Conference date: 18-09-2017 Through 21-09-2017.

[81] G. R. Spedding and P. B. S. Lissaman. Technical aspects of microscale flight systems. *Journal of Avian Biology*, 29(4):458–468, 1998. ISSN 09088857, 1600048X. URL http://www.jstor.org/stable/3677165.

[82] P C Stainback and K A Nagabushana. Review of Hot-Wire Anemometry Techniques and the Range of their Applicability for Various Flows. *Electronic Journal of Fluids Engineering, Transactions of the ASME*, 167:1–54, 1993.

[83] Y Su, A G R Evans, A Brunnschweiler, and G Ensell. Characterization of a highly sensitive ultra-thin piezoresistive silicon cantilever probe and its application in gas flow velocity sensing. *Journal of Micromechanics and Microengineering*, 12(6):780–785, sep 2002. doi: 10.1088/0960-1317/12/6/309. URL https://doi.org/10.1088/0960-1317/12/6/309.

[84] Johan Sundin, Katherine Kokmanian, Matthew K. Fu, Shervin Bagheri, and Marcus Hultmark. A soft material flow sensor for micro air vehicles. *Soft Robotics*, 8(2):119–127, 2021. doi: 10.1089/soro.2019.0130. URL https://doi.org/10.1089/soro.2019.0130. PMID: 32320328.

[85] O. Tabata. Fast-response silicon flow sensor with an on-chip fluid temperature sensing element. *IEEE Transactions on Electron Devices*, 33(3):361–365, 1986. doi: 10.1109/T-ED.1986.22495.

[86] Hidetoshi Takahashi, Eiji Iwase, Kiyoshi Matsumoto, and Isao Shimoyama. Air flow senser for an insect-like flapping wing. In *2008 IEEE 21st International Conference on Micro Electro Mechanical Systems*, pages 916–919, 2008. doi: 10.1109/MEMSYS.2008.4443806.

[87] Junliang Tao and Xiong (Bill) Yu. Hair flow sensors: from bio-inspiration to bio-mimicking—a review. *Smart Materials and Structures*, 21(11):113001, sep 2012. doi: 10.1088/0964-1726/21/11/113001. URL https://doi.org/10.1088/0964-1726/21/11/113001.

[88] Henk Tennekes. *The simple science of flight: from insects to jumbo jets*. MIT Press, 2009.

[89] Matthew J. Thompson, S. Watkins, C. White, and J. Holmes. Span-wise wind fluctuations in open terrain as applicable to small flying craft. *The Aeronautical Journal (1968)*, 115:693 – 701, 2011.

[90] G. Tschulena. Marktchancen sensoren. *Sensormagazin*, 1:1–4.

[91] TSI. *Air Velocity Calibrator Model 1127/1128 User's Manual [Part Number 1990791]*, d edition, sep 2010.

[92] Aline van den Kroonenberg, Tim Martin, Marco Buschmann, Jens Bange, and Peter Vörsmann. Measuring the wind vector using the autonomous mini aerial vehicle m2av. *Journal of Atmospheric and Oceanic Technology*, 25(11):1969 – 1982, 2008. doi: 10.1175/2008JTECHA1114.1. URL https://journals.ametsoc.org/view/journals/atot/25/11/2008jtecha1114_1.xml.

[93] J.L. Verboom, S. Tijmons, C. De Wagter, B. Remes, R. Babuska, and G.C.H.E. de Croon. Attitude and altitude estimation and control on board a flapping wing micro air vehicle. In *2015 IEEE International Conference on Robotics and Automation (ICRA)*, pages 5846–5851, 2015. doi: 10.1109/ICRA.2015.7140017.

[94] D. Warrick, M. Bundle, and K. Dial. Bird maneuvering flight: Blurred bodies, clear heads1. In *Integrative and comparative biology*, 2002.

[95] Simon Watkins, Juliette Milbank, Benjamin J. Loxton, and William H. Melbourne. Atmospheric winds and their implications for microair vehicles. *AIAA Journal*, 44(11):2591–2600, 2006. doi: 10.2514/1.22670. URL https://doi.org/10.2514/1.22670.

[96] Helmy Widyantara, Muhammad Rivai, and Djoko Purwanto. Wind direction sensor based on thermal anemometer for olfactory mobile robot. *Indonesian Journal of Electrical Engineering and Computer Science*, 13(2):475–484, 2019. ISSN 25024760. doi: 10.11591/ijeecs.v13.i2.pp475-484.

[97] James Wissman, Ariel Perez-Rosado, Alex Edgerton, Benjamin M Levi, Zeynep N Karakas, Mark Kujawski, Alyssa Philipps, Nicholas Papavizas, Danielle Fallon, Hugh A Bruck, and Elisabeth Smela. New compliant strain gauges for self-sensing dynamic deformation of flapping wings on miniature air vehicles. *Smart Materials and Structures*, 22(8):085031, jul 2013. doi: 10.1088/0964-1726/22/8/085031. URL https://doi.org/10.1088/0964-1726/22/8/085031.

[98] R.F Wolffenbuttel. *Electronic Instrumentation I: ET8017*. TU Delft, 2006.

[99] Yingchen Yang, Nannan Chen, Craig Tucker, Jonathan Engel, Saunvit Pandya, and Chang Liu. From artificial hair cell sensor to artificial lateral line system: Development and application. In *2007 IEEE 20th International Conference on Micro Electro Mechanical Systems (MEMS)*, pages 577–580, 2007. doi: 10.1109/MEMSYS.2007.4432986.

[100] Yizhou Ye, Zhenxiang Yi, Shixuan Gao, M. Qin, and Qing-An Huang. Octagon-shaped 2-d micromachined thermal wind sensor for high-accurate applications. *Journal of Microelectromechanical Systems*, 27:739–747, 2018.

[101] Yizhou Ye, Zhenxiang Yi, M. Qin, and Qing-An Huang. Eight-trigram-inspired mems thermal wind sensor with improved accuracy. *2018 IEEE Micro Electro Mechanical Systems (MEMS)*, pages 836–839, 2018.

[102] Liang Zhao, Qingfeng Huang, Xinyan Deng, and Sanjay Sane. Aerodynamic effects of flexibility in flapping wings. *Journal of the Royal Society, Interface / the Royal Society*, 7:485–97, 09 2009. doi: 10.1098/rsif.2009.0200.